January 2010

The Water Cycle at the Phoenix Landing Site, Mars

Selby Cull
Washington University in St. Louis

Recommended Citation

Cull, Selby, "The Water Cycle at the Phoenix Landing Site, Mars" (2010). *All Theses and Dissertations (ETDs)*. 78.
https://openscholarship.wustl.edu/etd/78

WASHINGTON UNIVERSITY IN ST. LOUIS

Department of Earth and Planetary Sciences

Dissertation Examination Committee:
Raymond E. Arvidson, Chair
Daniel Giammar
Rudolf Husar
Bradley Jolliff
Jill Pasteris
Jennifer Smith

THE WATER CYCLE AT THE PHOENIX LANDING SITE, MARS

by

Selby Cull

A dissertation presented to the
Graduate School of Arts and Sciences
of Washington University in
partial fulfillment of the
requirements for the degree
of Doctor of Philosophy

December 2010

Saint Louis, Missouri

ABSTRACT OF THE DISSERTATION

The Water Cycle at the Phoenix Landing Site, Mars

by

Selby Cull

Doctor of Philosophy in Earth and Planetary Sciences

Washington University in St. Louis, 2010

Professor Raymond E. Arvidson, Chairperson

The water cycle is critically important to understanding Mars system science, especially interactions between water and surface minerals or possible biological systems. In this thesis, the water cycle is examined at the Mars Phoenix landing site (68.22˚N, 125.70˚W), using data from the Compact Reconnaissance Imaging Spectrometer for Mars (CRISM), High-Resolution Imaging Science Experiment (HiRISE), the Phoenix Lander Surface Stereo Imager (SSI), and employing non-linear spectral mixing models.

The landing site is covered for part of the year by the seasonal ice cap, a layer of CO_2 and H_2O ice that is deposited in mid-fall and sublimates in mid-spring. During the mid-summer, H_2O ice is deposited on the surface at the Phoenix landing site. CO_2 ice forms at the site during fall. The onset date of seasonal ices varies

annually, perhaps due to variable levels of atmospheric dust. During fall and winter, the CO_2 ice layer thickens and sinters into a slab of ice, ~30 cm thick.

After the spring equinox, the CO_2 slab breaks into smaller grains as it sublimates. Long before all of the CO_2 ice is gone, H_2O ice dominates the near-infrared spectra of the surface. Additional H_2O ice is cold-trapped onto the surface of the CO_2 ice deposit during this time. Sublimation during the spring is not uniform, and depends on the thermal inertia properties of the surface, including depth of ground ice.

All of the seasonal ices have sublimated by mid-spring; however, a few permanent ice deposits remain throughout the summer. These are small water ice deposits on the north-facing slopes of Heimdal Crater and adjacent plateaus, and a small patch of mobile water ices that chases shadows in a small crater near the landing site.

During the late spring and early summer, the site is free of surface ice. During this time, the water cycle is dominated by vapor exchange between the subsurface water ice deposits and the atmosphere. Two types of subsurface ice were found at the Phoenix landing site: a pore water ice that appears to be in diffusive equilibrium with the atmosphere, and an almost pure water ice deposit that is apparently not in equilibrium.

In addition to vapor and solid phases of the water cycle, there is strong evidence of a liquid phase. Patches of concentrated perchlorate salt are observed in trenches dug by the lander. Perchlorate is believed to form at the landing site through atmospheric interactions, which deposit the salts on the surface. The salts are then dissolved and translocated to the subsurface by thin films of liquid water. These thin films may arise due to perchlorate interactions with the atmospheric water vapor or seasonal ices. It is possible that the winter CO_2 ice slab may act as a greenhouse cap, trapping enough heat for the underlying fall-deposited water ice to react with the perchlorate to form thin films of brines. Alternatively, the brines may form when summertime water vapor interacts with perchlorate on the surface, when temperatures rise above the perchlorate brine eutectic.

Acknowledgements

I gratefully thank my advisor, R.E. Arvidson, for his years of thoughtful guidance and support. I am also grateful to the many co-authors who have collaborated with me on these projects, especially M. Mellon, S. Wiseman, R.V. Morris, J. Catalano, and D. Ming. I thank my committee members, B. Jolliff, J. Pasteris, J. Smith, D. Giammar, and R. Husar. And, I thank the Phoenix, HiRISE, and CRISM science teams, who acquired the data sets analyzed here, especially L. Tamppari and F. Seelos, who orchestrated the coordinated observation campaigns.

Portions of this work were funded by fellowships from the McDonnell Center for Space Sciences at Washington University in St. Louis, the Missouri Space Grant Consortium, the CRISM science team, and the Phoenix science team.

TABLE OF CONTENTS

List of Figures

List of Tables

List of Abbreviations

Acronym	**Full Name**
AFM	Atomic Force Microscope
CRISM	Compact Reconnaissance Imaging Spectrometer for Mars
DISORT	Discrete Ordinate Radiatve Transfer
e	Emergence angle
FRT	Full-Resolution Targeted image
g	Phase angle
GRS	Gamma Ray Spectrometer
HEND	High Energy Neutron Detector
HiRISE	High-Resolution Imaging Science Experiment
HRL	Half-Resolution Long targeted image
i	Incidence angle
I/F	Spectral radiance at the sensor divided by solar spectral irradiance divided by pi
LMST	Local Mean Solar Time
Ls	Solar Longitude
LTST	Local True Solar Time
MECA	Microscopy Electroconductivity and Conductivity Analyzer
MRO	Mars Reconnaissance Orbiter

OM	Optical Microscope
p(g)	Surface phase function
RA	Robotic Arm
RAC	Robotic Arm Camera
SSI	Surface Stereo Imager
TECP	Thermal and Electrical Conductivity Probe
TEGA	Thermal and Evolved Gas Analyzer
TES	Thermal Emission Spectrometer
w	Single-scattering albedo
WCL	Wet Chemistry Laboratory

Chapter 1 - Introduction

The water cycle is one of the most fundamental components in Earth system science. It describes how, where, and under what conditions the various phases of water interact with Earth's atmosphere, lithosphere, biosphere, and surface materials. It is critical to our understanding of Earth surface processes, including erosion, sedimentation, soil mechanics, soil development, and mineral distributions. It is fundamental to our knowledge of weather and climate. And, it is crucial for our understanding of Earth's biological systems.

As on Earth, the water cycle on Mars is a fundamental element of Mars system science. However, whereas Earth's water cycle is relatively well-understood, we have barely begun to quantify the water cycle on Mars. Until recently, our understanding of the Martian water cycle has been limited by a lack of ground truth and a lack of integration of data sets.

However, in the last several years, the Mars Reconnaissance Orbiter (MRO) and Mars Express Orbiter (MEX) have returned data sets that cover vast areas of the surface, in high spatial and temporal resolution. Meanwhile, on the surface, the Mars Phoenix Lander has returned complementary data sets that can be used as ground truth. When combined, these data sets allow us to map out the water cycle on Mars in great detail; to illuminate interactions between Mars' water cycle, CO_2 cycle, dust cycle, and surface materials; and to predict where and when, if ever, a biosphere played a role.

Perhaps the best location at which to demonstrate how orbital and ground-based data sets can be integrated to map out the water cycle is the landing site of the Mars Phoenix mission, a lander that touched down on the northern plains of Mars on 25 May 2008 (Figure 1.1). The site is ideal for mapping the Martian water cycle for several reasons:

First, the site was the focus of a long-term coordinated observation campaign [*Tamppari et al.,* 2009], wherein both MRO/MEX orbital and Phoenix ground-based instruments routinely monitored the site and the surrounding areas. These campaigns resulted in a data set more spatially and temporally complete than for any other site on Mars.

Second, Phoenix landed above the Martian Arctic circle, at 68.22˚N, 125.70˚W (planetocentric; *Smith et al.*, 2009). This area is covered for part of the year by the seasonal ice cap, a layer of CO_2 and H_2O ice that extends from the pole to ~50˚N [*Larson and Fink* 1972; *James et al.,* 1993, Figure 1.2]. Seasonal cap dynamics are a major part of Mars' water cycle, and the coordinated observation campaigns capture the cap's deposition and sublimation at the Phoenix landing site over the course of a Martian year. These data sets, then, allow us to track annual interactions between seasonal ices and other phases of the water cycle at the Phoenix landing site.

Third, the Phoenix site was chosen based on data from the Gamma Ray Spectrometer (GRS) that suggested high abundances of subsurface hydrogen in the form of water ice. This prediction was verified by Phoenix's Thermal and Evolved Gas Analyzer (TEGA, Figure 1.3), which sampled subsurface ice and confirmed it to be water [i.e., *Smith et al.*, 2009]. Inasmuch as subsurface water ice interacts with soil, the atmosphere, and seasonal ices, it is a critical part of the water cycle on Mars.

Thus, due to its proximity to ground ice, location within the extent of the seasonal ice cap, and frequent targeted coverage, the Phoenix site is ideal for studying the water cycle on Mars.

In the chapters that follow, I analyze the water cycle at the Phoenix landing site using a variety of data sets that were obtained between December 2006 and December 2008:

In chapters 2 and 3, I track the deposition, evolution, and sublimation of the seasonal ice cap at the Phoenix landing site, using data from the Compact Reconnaissance Imaging Spectrometer for Mars (CRISM), the High-Resolution Imaging Science Experiment (HiRISE), and Phoenix's Surface Stereo Imager (SSI). I also use these data sets to track interactions between seasonal ices and the CO_2 and dust cycles.

In chapter 4, I analyze the composition of subsurface ices at the Phoenix landing site, using data from the SSI and a non-linear spectral mixing model.

In chapter 5, I map the distribution of perchlorate salt at the landing site, using SSI data, in an effort to understand water-salt interactions on the surface.

The work presented in these chapters has been published elsewhere. Chapters 2 and 3 were published in the *Journal of Geophysical Research* [*Cull et al.,* 2010a, *Cull et al.,* 2010b]. Chapters 4 and 5 are accepted and in-press in *Geophysical Research Letters* [*Cull et al.,* 2010c, *Cull et al.,* 2010d].

In addition to these chapters, I have co-authored several papers, contributing research that also adds to our understanding of the water cycle at the Phoenix landing site [*Arvidson et al.*, 2008, *Seelos et al.*, 2008, *Arvidson et al.,* 2009, *Bryne et al.,* 2009, *Heet et al.,* 2009, *Mellon et al.,* 2009, *Searls et al.,* 2010]. These projects were led by others, and so are not included as chapters in this thesis; however, much of the work that I contributed to these papers illuminates important aspects of the water cycle at the Phoenix landing site. In the final synthesis (chapter 6), I include relevant results from these papers, relating them to the results presented in chapters 2, 3, 4, and 5.

Figures

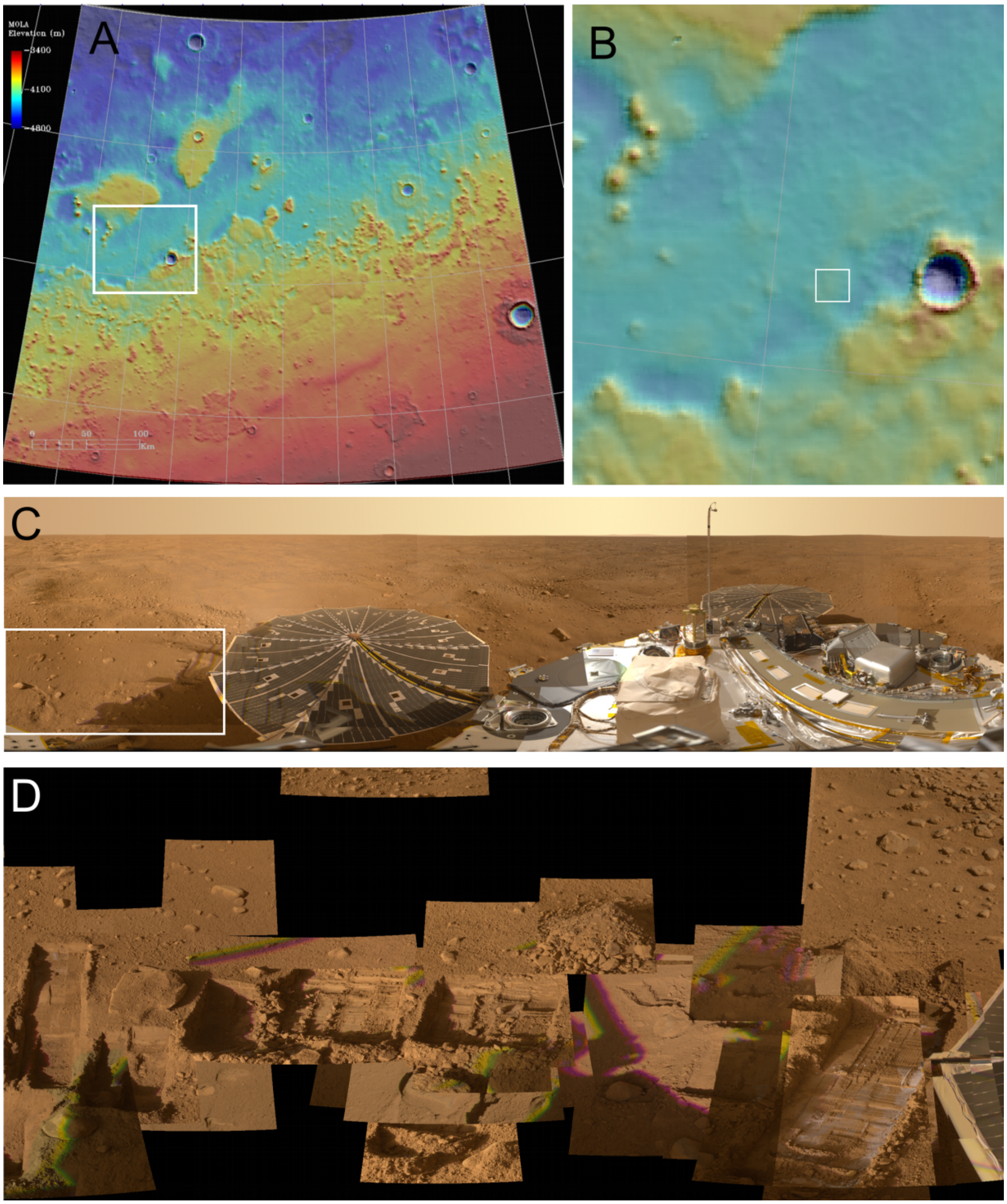

Figure 1.1 – Phoenix landing site, Mars.

A) Map of regional topography around Phoenix landing site (warmer colors indicate higher elevations, see key at left). The landing site is marked with the white box, which also indicates the location of frame B. B) Close-up topographic view of Phoenix landing site area. The valley is smooth-floored, with little topographic variation. The large crater on the east side is Heimdal, ~10 km wide. White box indicates location of Phoenix landing site. C) SSI panorama of Phoenix landing site, including Phoenix deck and one solar panel (near-true color: R=603.8 nm, G=532.0 nm, B=: 485.3 nm). Polygonal terrain can be seen all around the lander. White box indicates location of panel D. D) SSI mosaic of the work space, where Phoenix's Robotic Arm was able to dig trenches (near true-color, same filters as above). The lander dug 12 trenches over the course of the mission, several of which exposed the ice table. Here, the ice table can be seen in the far-right trench (Snow White).

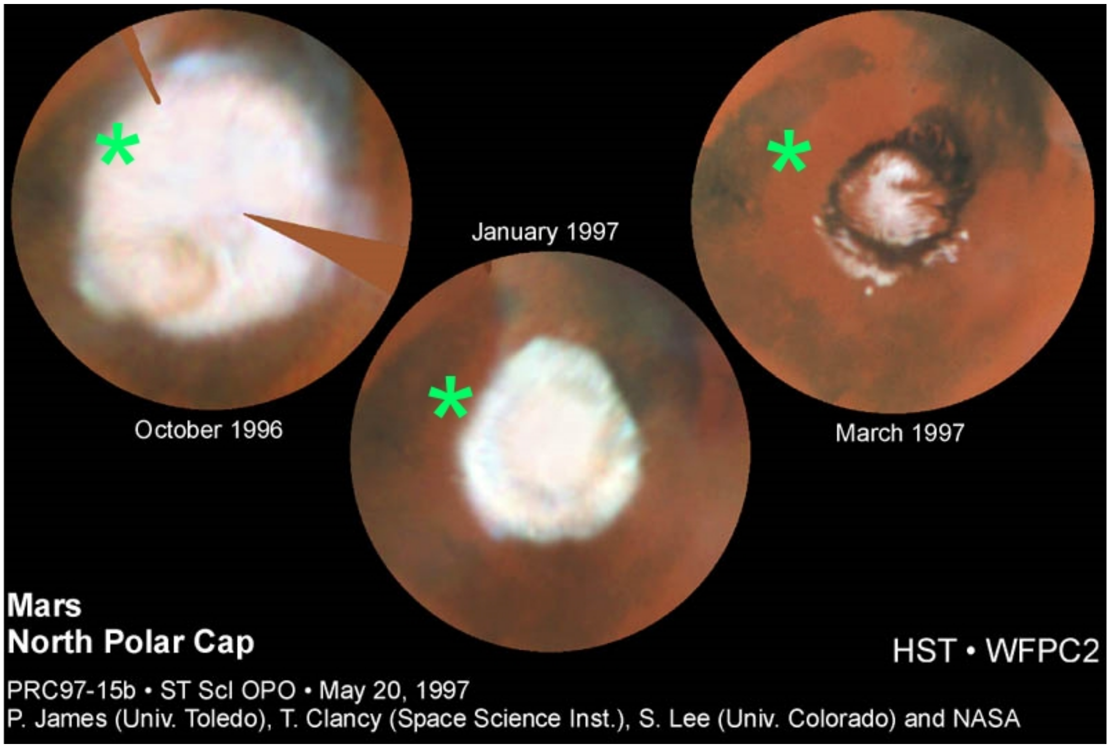

Figure 1.2 - Northern seasonal ice cap, Mars.

The Phoenix landing site (green asterisks) is covered for part of the year by the seasonal ice cap. In the Hubble Space Telescope images above, the globe at the right is the summertime northern polar region. The ice remaining at the pole is the perennial water ice cap that remains year-round. As summer ends, surface temperatures cool to the point that H_2O and CO_2 ices form on the surface, spreading south to form the seasonal ice cap (far left). The cap retreats in spring (center).

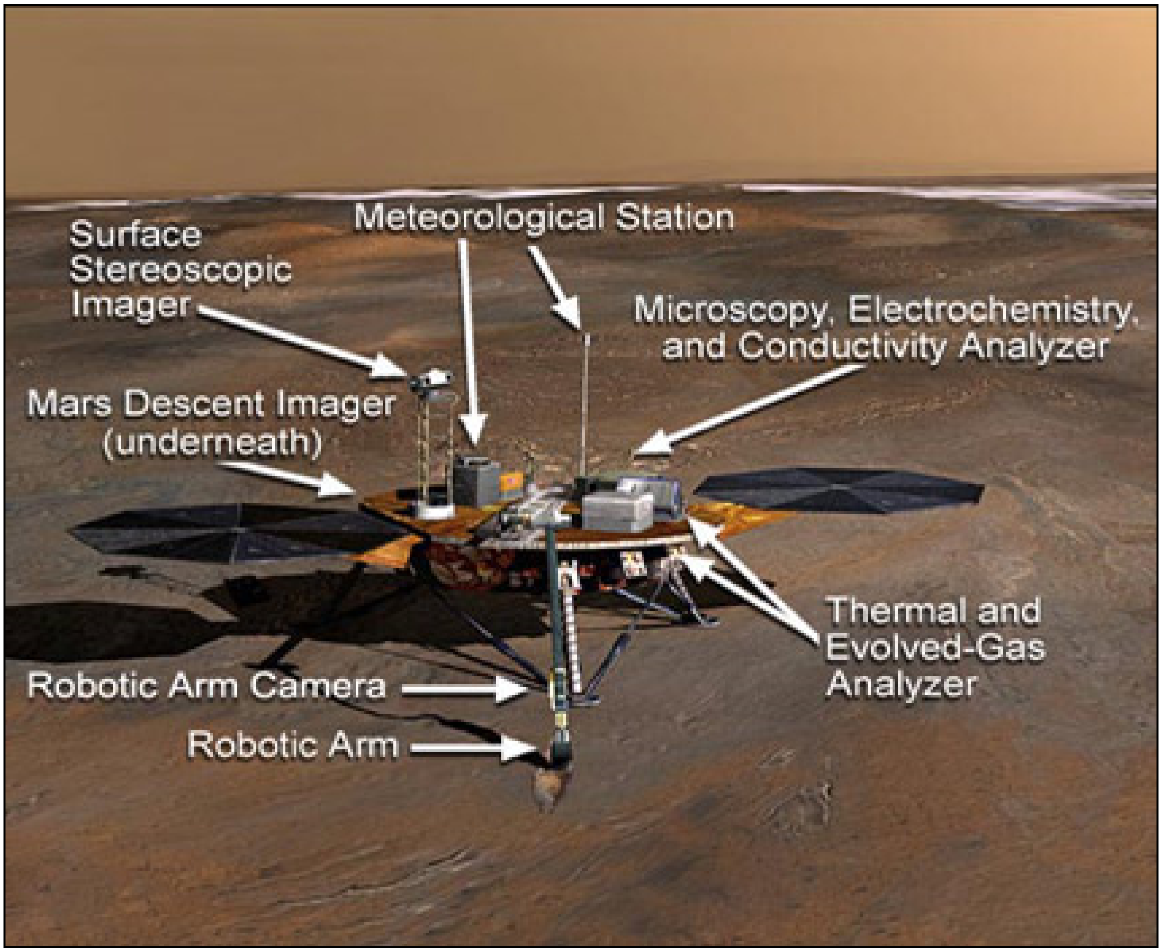

Figure 1.3 – Instruments onboard the Phoenix lander.

The Phoenix lander was equipped with the Surface Stereo Imager (SSI), Mars Descent Imager, Robotic Arm (RA), Robotic Arm Camera (RAC), Thermal and Evolved-Gas Analyzer (TEGA), Meteorological Station, and Microscopy, Electrochemistry, and Conductivity Analyzer (MECA), which included an Optical Microscope (OM), Atomic Force Microscope (AFM), Wet Chemistry Laboratory (WCL), and Thermal and Electrical Conductivity Probe (TECP).

References

Arvidson, R.E., D. Adams, G. Bonfiglio, P. Christensen, S. Cull, M. Golombek, J. Guinn, E. Guinness, T. Heet, R. Kirk, A. Knudson, M. Malin, M. Mellon, A. McEwen, A. Mushkin, T. Parker, F. Seelos, K. Seelos, P. Smith, D. Spencer, T. Stein, L. Tamppari (2008) Mars Exploration Program 2007 Phoenix landing site selection and characteristics. *Journal of Geophysical Research*, 113, E00A03, doi:10.1029/2007JE003021.

Arvidson, R.E., R. Bonitz, M. Robinson, J. Carsten, R. Volpe, A. Trebi-Ollennu, M. Mellon, P. Chu, K. Davis, J. Wilson, A. Shaw, R. Greenberger, K. Siebach, T. Stein, S. Cull, W. Goetz, R. Morris, D. Ming, H. Keller, M. Lemmon, H. Sizemore, M. Mehta (2009), Results from the Mars Phoenix Lander Robotic Arm experiment, *Journal of Geophysical Research*, 114, E00E02, doi:10.1029/2009JE003408.

Byrne, S., Colin M. Dundas, Megan R. Kennedy, Michael T. Mellon, Alfred S. McEwen, Selby C. Cull, Ingrid J. Daubar, David E. Shean, Kimberly D. Seelos, Scott L. Murchie, Bruce A. Cantor, Raymond E. Arvidson, Kenneth S. Edgett, Andreas Reufer, Nicolas Thomas, Tanya N. Harrison, Liliya V. Posiolova, Frank P. Seelos (2009) Distribution of mid-latitude ground-ice on Mars from new impact craters. *Science*, 325(5948): 1674-1676. doi: 10.1126/science.1175307

Cull, Selby, R Arvidson, M.Mellon, S.Wiseman, R. Clark, T.Titus, RV Morris, P McGuire (2010a) The Seasonal H_2O and CO2 Ice Cycle at the Mars Phoenix Landing Site: I. Pre-Landing CRISM and HiRISE Observations. *Journal of Geophysical Research*, 115: doi:10.1029/2009JE003340.

Cull, Selby, R. Arvidson, R. V. Morris, M. Wolff, M. T. Mellon, M. T. Lemmon. (2010b) The Seasonal Ice Cycle at the Mars Phoenix Landing Site: II. Post-Landing CRISM and Ground Observations. *Journal of Geophysical Research*, 115, E00E19, doi:10.1029/2009JE003410.

Cull, Selby, R. E. Arvidson, M. T. Mellon, P. Skemer, A. Shaw, and R. V. Morris (2010c) Compositions of subsurface ices at the Mars Phoenix Landing Site. *Geophysical Research Letters*. doi:10.1029/2010GL045372, in press.

Cull, Selby, R. E. Arvidson, J. G. Catalano, D. W. Ming, R. V. Morris, M. T. Mellon, and M. Lemmon (2010d) Concentrated perchlorate at the Mars Phoenix landing site: Evidence for thin film liquid water on Mars. *Geophysical Research Letters*. doi:10.1029/2010GL045269, in press.

Heet, T,. R. E. Arvidson, S. C. Cull, M. T. Mellon, and K. D. Seelos (2009) Geomorphic and geologic settings of the Phoenix lander mission landing site. *Journal of Geophysical Research*, 114, E00E04, doi:10.1029/2009JE003416, 2009.

James, P.B., H. H. Kieffer, and D. A. Paige (1993) The seasonal cycle of carbon dioxide on Mars, in Mars (Hugh Kieffer, editor), University of Arizona Press: Tucson, Arizona.

Larson, H.P. and U. Fink (1972) Identification of carbon dioxide frost on the Martian polar caps. *The Astrophysical Journal* 171: L91-L95.

Mellon, M.T., R. Arvidson, H. Sizemore, M. Searls, D. Blaney, S. Cull, M. Hecht, T. Heet, H.U. Keller, M. Lemmon, W. Markiewicz, D. Ming, R. Morris, W. Pike, A. Zent (2009) Ground ice at the Phoenix landing site: Stability, state, and origin. *Journal of Geophysical Research* 114: E00E08, doi:10.1029/2009JE003417.

Searls, M.L., M. Mellon, S. Cull, C.J. Hansen, H. Sizemore (2010) Seasonal defrosting of the Phoenix landing site. *Journal of Geophysical Research* 115: E00E24, doi:10.1029/2009JE003438.

Seelos, K. D., R. Arvidson, S. Cull, C. Hash, T. Heet, E. Guinness, P. McGuire, R. Morris, S. Murchie, T. Parker, T. Roush, F. Seelos, M. Wolff (2008), Geomorphologic and mineralogic characterization of the northern plains of Mars at the Phoenix Mission candidate landing sites, *Journal of Geophysical Research*, 113, E00A13, doi:10.1029/2008JE003088.

Smith, P.H., Leslie K. Tamppari, Raymond E. Arvidson, Deborah Bass, D. Blaney, W. V. Boynton, A. Carswell, D. C. Catling, Benjamin C. Clark, T. Duck, E. DeJong, D. Fisher, W. Goetz, H. P. Gunnlaugsson, M. H. Hecht, V.

Hipkin, J. Hoffman, S. F. Hviid, H. U. Keller, S. P. Kounaves, C. F. Lange, M. T. Lemmon, M. B. Madsen, W. J. Markiewicz, J. Marshall, C. P. McKay, M. T. Mellon, D. W. Ming, R. V. Morris, W. T. Pike, N. Renno, U. Staufer, C. Stoker, P. Taylor, J. A. Whiteway, A. P. Zent (2009) Water at the Phoenix Landing Site. *Science* 325: doi:10.1126/science.1172339.

Tamppari, L.K., D. Bass, B. Cantor, I. Daubar, C. Dickinson, D. Fisher, K. Fujii, H.P. Gunnlauggson, T.R. Hudson, D. Kass, A. Kleinbohl, L. Komguem, M.T. Lemmon, M. Mellon, J. Moores, A. Pankine, M. Searls, F. Seelos, M.D. Smith, S. Smrekar, P. Taylor, C. von Holstein-Rathlou, W. Weng, J. Whiteway, M. Wolff (2009) Phoenix and MRO Coordinated Atmospheric Measurements. *Journal of Geophysical Research*, doi:10.1029/2009JE003415.

Chapter 2 - The seasonal H_2O and CO_2 ice Cycles at the Mars Phoenix landing site: I. Pre-landing CRISM and HiRISE observations

Journal of Geophysical Research, 115: doi:10.1029/2009JE003340.

2.1 Introduction

NASA's Phoenix Scout Mission landed on the northern plains of Mars on 25 May 2008, at solar longitude (L_s) ~80˚, at 68.22˚N, 125.70˚W (planetocentric; *Smith et al.*, 2009). Mission science objectives focused on characterizing the high-latitude environment and implications for habitability, including mapping subsurface ice and tracking seasonal polar changes from northern late spring through summer [*Smith et al.*, 2008].

The Phoenix landing site is within the area covered by the seasonal ice cap, a layer of CO_2 and H_2O ice that extends down to 50°N and covers the permanent northern H_2O ice cap from late summer through late spring [*Larson and Fink* 1972; *James et al.*, 1993]. More than 25% of the carbon dioxide in the Martian atmosphere condenses to form the seasonal cap, beginning in late northern summer and coinciding with the onset of regional dust storms in the southern hemisphere [*Forget et al.*, 1995*; Kieffer and Titus* 2001]. Atmospheric dust may act as condensation nuclei for seasonal CO_2 ice, although the majority of CO_2 ice is expected to form directly on the surface as a result of radiative cooling [*Forget et al.*, 1998]. Estimates of CO_2 ice depth and duration within the Phoenix latitude band (65°-72°N) vary considerably; however, at the pole, the cap grows to more than a meter deep by mid-winter [*Smith et al.*, 2001], and begins to sublimate during early spring, finally disappearing by late spring [*Wagstaff et al., 2008*]. As the CO_2 ice sublimates, it leaves behind an annulus of water ice [*Bibring et al.*, 2005], perhaps deposited in fall and re-exposed during the spring, or cold-trapped onto the surface during or after CO_2 sublimation [*Seelos et al.*, 2008]. The large spatial scale, volume of CO_2, and the global dust, CO_2, and H_2O cycle dynamics make the seasonal evolution of the polar cap one of the more important climatic processes on Mars.

The CO_2 cap is relevant to the Phoenix mission because it is closely tied to the presence and dynamics of ground H_2O ice. Shallow ground water ice fills in subsurface soil pore spaces and increases thermal conductivity, which allows more summer heat into the ground [*Mellon et al.*, 2008a]. Gradually released, this heat warms the surface enough to slow the CO_2 ice rate of condensation and to increase the rate of sublimation [*Aharonson* 2004; *Kieffer* 2007; *Haberle et al.*, 2008]. The depth to the top of the ground ice is in turn controlled by surface soil properties and albedo variations [*Sizemore and Mellon* 2006], both of which influence ice deposition and sublimation rates.

Because the seasonal CO_2 cap is a major component of the ice and dust cycles and is closely related to ground water ice, it is important to understand its behavior at the Phoenix landing site. Previous studies have characterized the large-scale behavior of the seasonal cap and shown that the cap deposition and retreat patterns are longitude-dependent, especially at mid-latitudes [*James and Cantor* 2001*; Benson and James* 2005]. There is considerable disagreement among data sets examined prior to this study on the cap evolution within the Phoenix latitude band. In particular, the reported "crocus date," or date of the disappearance of the last CO_2 ice [*Titus et al.,* 2001], varies widely: from L_s ~35˚-55˚ based on Thermal Emission Spectrometer (TES) temperature estimates [*Kieffer and Titus* 2001], to L_s ~70˚ based on models from High Energy Neutron Detector (HEND) data [*Litvak et al.*, 2005]. In MOC images, the edge of the cap reached ~68˚N by L_s~44˚ during the 2000 recession, and by L_s~48˚ during the 2002 recession [*Benson and James* 2005]. Viking Infrared Thermal Mapper data shows the cap edge reaching ~68˚N at L_s~56˚ [*James and Cantor* 2001].

The Phoenix primary and extended mission lasted most of the martian northern summer (L_s ~80˚ to 145˚; *Smith et al.,* 2009; *Arvidson et al.,* 2009). However, our understanding of ice and dust cycles at the landing site is incomplete without analyses of ice evolution from L_s ~145˚ to L_s ~80˚ (late summer, fall, winter, and spring). In this paper, detailed analyses are presented of the winter-to-spring and summer-to-fall evolution of ice around the Phoenix landing site, using high-resolution orbital data. The data cover 65˚N-72˚N, 230˚E-250˚E (“Region D” in *Seelos et al.,* 2008*)*, an area that was selected for the Phoenix landing site for its low rock abundances and postulated shallow ground water ice [*Arvidson et al.,* 2008; *Mellon et al.,* 2008a].

The prelanding advance and retreat of ices over the Phoenix site discussed in this paper were observed using hyperspectral data from the Compact Reconnaissance Imaging Spectrometer for Mars (CRISM; *Murchie et al.,* 2007) onboard Mars Reconnaissance Orbiter (MRO). To estimate changes in ice grain sizes and abundances, non-linear mixing models [*Hapke* 1981, 1993] were used to calculate reflectances of theoretical soil-H_2O-CO_2 mixtures. Images from the MRO High-Resolution Imaging Science Experiment (HiRISE; *McEwen et al.,* 2007) were used to track small-scale sublimation patterns in spring, and to estimate changing ice thicknesses. CRISM and color HiRISE images were also used to track changes in surface brightness and color. These analyses, when combined with coordinated Phoenix ground and orbital observations, will provide a full year view of the surface ice and dust cycles at the landing site.

2.2 Spectral Fitting - Data Sets and Methods

The CRISM instrument consists of two detectors: a shortwave (“S”) detector with bands between 0.3646 and 1.0560 μm, and a long-wavelength (“L”) detector with bands between 1.0014 and 3.9368 μm. The spectrometer is mounted to a gimbal platform, which enables off-nadir pointing and ground-tracking of a target. CRISM can operate either in hyperspectral (544 channels) or multichannel (72 channel subset) mode. In multispectral mode, the gimbal is pointed to nadir and remains fixed, collecting 10-km-wide observations at 72 wavelengths and either 100- or 200-m/pixel resolution. In hyperspectral, or targeted mode, the gimbal scans along the optical line-of-sight, allowing for longer integration times without along-track smear. Targeted observations are taken with all 544 wavelengths, at either full-spatial resolution (FRT; 15-19 m/pixel) or 2x spatially-binned (HRS/HRL; 30-40 m/pixel) to cover a larger area. CRISM data utilized in this study were processed to units of *I/F* (spectral radiance at the sensor divided by solar spectral irradiance divided by pi).

This study used 49 FRTs taken over “Region D,” most of which were taken in the summer and spring (Figure 2.1), with a few observations acquired in fall and winter. All but three of the observations were acquired between 13:30 – 15:00 local mean solar time (LMST).

2.2.1 Atmospheric Correction

CRISM *I/F* spectra have radiative contributions from both the surface and atmosphere, including gas and aerosol absorption, scattering, and emission. This study uses the Discrete Ordinate Radiative Transfer (DISORT) model [*Stamnes et al.*, 1988*; Wolff et al.*, 2007] to separate atmospheric and surface contributions from CRISM *I/F* spectra. DISORT can be used to calculate: 1) the scattering and attenuation of a solar beam down through the atmosphere; 2) interactions with a user-defined surface; and 3) scattering and attenuation up through the atmosphere. We used routines with DISORT that are optimized for calculations of the Martian atmosphere [*Wolff et al.*, 2009] and procedures developed for use with CRISM data [*Arvidson et al.*, 2008; *Wiseman et al.*, 2009]. DISORT was used to generate a series of modeled *I/F* spectra that would be observed at the top of the atmosphere (*e.g.*, contain both surface and atmospheric contributions) given known surface reflectance spectra. The DISORT model results were used to retrieve surface reflectance values (*e.g.*, atmospherically corrected spectra) from measured CRISM *I/F* data using a lookup table approach. This process is diagramed in Figure 2.2.

For this process to accurately atmospherically-correct CRISM spectra, we must accurately approximate the atmosphere at the time of observation (Section 2.2.1-a below) and the scattering behavior of the surface (Section 2.2.1-b below).

2.2.1-a Defining Atmospheric Parameters

We included in our model the atmospheric pressure-temperature profile, contributions from atmospheric gases (CO_2, CO, H_2O), and contributions from aerosols (dust and ice). Temperatures for each layer of the atmosphere were taken from historical Thermal Emission Spectrometer (TES) climatology observations at the appropriate latitude, longitude, and L_s [*Conrath et al.,* 2000; *Smith* 2002]. Surface pressure was based on Viking lander measurements, and the pressure for each atmospheric layer calculated by integrating the hydrostatic equilibrium equation [*Conrath et al.,* 2000]. H_2O vapor abundances were taken from historical TES data [*Smith* 2002]. Dust and ice aerosol abundances were also derived from historical TES estimates of the optical depth (tau) of dust at 9.3 μm and ice at 12.1 μm [*Smith* 2004].

To account for aerosol scattering effects, ice and dust single-scattering albedos (*w*) and particle phase functions [*p(g)*] were input and radiatively modeled. For ice, *w* was calculated using optical constants from *Warren* [1984] and an assumed particle radius of 2.0 μm, and *p(g)* was modeled as a Legendre polynomial with coefficients from *Clancy et al.,* [2003]. For dust, *w* was calculated using optical constants derived from CRISM observations [*Wolff et al.,* 2009] and an assumed particle radius of 1.5 μm, and *p(g)* was modeled as a wavelength-dependent Legendre polynomial with coefficients from *Wolff et al.,* [2009]. Dust aerosols were assumed to be uniformly distributed throughout each layer, with a constant volume-mixing ratio, and ice aerosols were assumed to be well-mixed above the altitude at which water condenses.

To account for small (<~1 nm) time-dependent shifts in center wavelength due to instrument temperature changes, radiative transfer models were first run with high spectral resolution (0.1 nm spacing) over the CO_2 gas band region, and the wavelengths resampled and fit to observed wavelengths to determine wavelength offset, a technique developed by *Wiseman* [2007, 2009].

2.2.1-b Defining the Surface

The lower boundary of the atmosphere was defined within DISORT as a surface that scatters light according to the scattering model [*Hapke* 1993]:

$$r(i,e,g) = \frac{w}{4\pi}\frac{\mu_0}{\mu_0+\mu}\left\{[1+B(g)]p(g)+H(\mu_0)H(\mu)-1\right\}$$

Equation 2.1

where i, e, and g are the incidence, emergence, and phase angles, respectively; $r(i,e,g,)$ is the bidirectional reflectance observed, μ_0 is the cosine of i, μ is the cosine of e, $B(g)$ is the opposition effect, $p(g)$ is the surface phase function, and $H(\mu_0)$ $H(\mu)$ describe multiple scattering.

The surface phase function was modeled as a two-lobed Henyey-Greenstein model [*Henyey and Greenstein* 1941]:

$$p(g) = \frac{(1-\delta^2)(1-f)}{[1-2\delta\cos(g)+\delta^2]^{3/2}} + \frac{f(1-\delta^2)}{[1+2\delta\cos(g)+\delta^2]^{3/2}}$$

Equation 2.2

where f is a weighting factor that describes the scattering direction (f=0 for forward scatter, f=1 for backscatter), and δ is an asymmetry factor constrained to be between -1 and 1 (δ=0 for isotropic scatter).

Deriving the spectrophotometric functions for Phoenix soils and ices is beyond the scope of this paper; however, it is important to constrain them to reasonable values, since scattering parameter selection can affect the overall albedo of a spectrum (Figure 2.3). *Cull et al.*, [2010] showed that surface soils at the Phoenix landing site have scattering parameters similar to those derived by *Johnson et al.*, [2006] for soils at the Spirit landing site at Gusev Crater: an asymmetry parameter of 0.498, forward-scattering fraction of 0.817, and *h* of 0.385. The Gusev Crater Soil endmember is a wide-spread plains unit photometrically similar to many Martian soils, including soils at the Viking 1 [*Arvidson et al.*, 1989] and Mars Pathfinder landing sites [*Johnson et al.*, 1999]. We assumed soils at the Phoenix landing site have the same scattering properties as Gusev soils.

The opposition effect, *B(g)*, was ignored in our calculations, because it is only important for observations with small phase angles. FRTs used in this study were obtained with large phase angles (> 40°).

2.2.1-c Retrieval of Surface Reflectance from CRISM I/F

In order to calculate atmospherically-corrected surface reflectance from CRISM *I/F*, DISORT was used to model the *I/F* that would be observed at the top of the atmosphere for 6 input surfaces with variable *w* values, with all other parameters fixed. The relationship between modeled *I/F* and calculated *w* was determined using a 5th-order polynomial fit to output from DISORT calculations. For each CRISM band, a look-up table between modeled *I/F* and *w* was used to retrieve *w* for a measured CRISM *I/F* value (Figure 2.2). Atmospheric parameters were adjusted slightly and the models re-run to remove residual atmospheric contributions, if necessary. Examples of pre- and post-atmospherically-corrected spectra are shown in Figure 2.4.

Because subsequent surface modeling (see Section 2.2.2 below) was done in terms of bidirectional reflectance, retrieved values of *w* as a function of wavelength were converted to bidirectional reflectance using

$$r(i,e,g) = \frac{w}{4\pi}\frac{\mu_0}{\mu_0+\mu}\left\{[1+B(g)]p(g)+H(\mu_0)H(\mu)-1\right\}$$

Equation 2.1

2.2.2 *Modeling of Surface Spectra*

To estimate the relative abundances and grain sizes of H_2O ice, CO_2 ice, and soil in CRISM observations, spectra of theoretical mixtures of these three components were generated using a non-linear mixing model, and compared to bidirectional surface reflectance spectra retrieved from CRISM images as described in Section 2.2.1 above.

2.2.2-a Spectral Mixing Model

CRISM bidirectional surface reflectance spectra were extracted from the geomorphic unit on which Phoenix landed: the unit first named Lowland Bright by *Seelos et al.*, [2008] and later re-named Heimdal Outer Ejecta by *Heet et al.*, [2009]. This unit is widespread around the Phoenix landing site and visible in CRISM observations acquired at multiple L_s. Five-by-five pixel average spectra were compared across the unit in each scene and a representative spectrum selected for modeling.

To extract grain sizes and relative abundances of water ice, CO_2 ice, and soil, each spectrum was modeled using the non-linear mixing model described by *Hapke* [1981, 1993]. Single-scattering albedos of mixtures were calculated as from *Hapke* [1981]:

$$w = \frac{\sum_{i=1}^{i=N}\left(Q_{Si} M_i / \rho_i D_i\right)}{\sum_{i=1}^{i=N}\left(Q_{Ei} M_i / \rho_i D_i\right)}$$

Equation 2.3

where M_i is the mass fraction of component i, ρ_i the solid density, D_i the diameter, Q_{Si} the scattering efficiency, Q_{Ei} the extinction efficiency, and the summation is carried out for all components in the mixture. Because the particles considered here are large compared to the wavelengths, we assume that the extinction efficiency is 1, which indicates that the particle's surface is affecting the entire wavefront [*Hapke* 1981]. The scattering efficiency is calculated using the internal and external reflection coefficients and the absorption coefficient, as described in detail by *Roush* [1994]. In addition, to account for observations with a layer of transparent ice covering soil, a two-layer non-linear mixing model described by *Equations 9.31a-e* in *Hapke* [1993] was used. For each spectrum, $p(g)$ parameters were matched to the DISORT parameters discussed in Section 2.2.1-b above. Because the size parameter ($X=\pi D/\lambda$) is >> 1 for our wavelength region, we ignore the effects of resonant oscillations.

In the layered models, the thickness of the overlying layer was calculated based on the cross-sectional mass (e.g., mg/cm^2). To convert this to a layer thickness, the cross-sectional mass was divided by the material's solid density.

In our non-linear mixing models, we ignored the effects of macroscale roughness, since the Hapke model's roughness term [e.g. *Hapke* 1984] appears to be inaccurate for high-albedo surfaces [*Byrne et al.*, 2008, *Domingue et al.,* 1997], and macroscale roughness should not be a significant factor at the Phoenix landing site, where slopes are typically ≤ 5° [*Kirk et al.,* 2008]. With these assumptions, the bidirectional reflectance of the surface depended on material properties (optical constants, particle size, and density) and observational geometry (*i, e, g*, and λ). In our modeling, we used CRISM wavelengths and FRT-specific incidence, emergence, and phase angles.

Three surface components were included in the non-linear modeling: H_2O ice, CO_2 ice, and a Mars soil analog. The soil component utilized optical constants based on a Mauna Kea palagonite sample – a low-temperature alteration product of fine-grained basaltic ash [*Clancy et al.,* 1995]. Based on both orbital and ground observations, dehydrated palagonite mixed with nanophase iron oxides appears to be a good analog for the Phoenix site soils [*Arvidson et al.*, 2009*; Heet et al.*, 2009]. For modeling, optical constants were used from *Hansen* [1997, 2005] for CO_2 ice, *Warren* [1984] for H_2O ice, and solid densities of ρ=1.562 g/cm^3 for solid CO_2, ρ=0.9167 g/cm^3 for solid H_2O, and ρ=2.700 g/cm^3 for palagonite were assumed. The bidirectional reflectance was then modeled as a function of grain size and relative mass fraction. We define "grain size" as a grain's diameter.

Water ice and soil optical constants were resampled to the bandpasses used in the CO_2 optical constants measurements, because their absorption features are less likely to be altered by resampling than the narrow CO_2 ice absorptions. Bidirectional reflectances were calculated with the Hapke model, and the results were convolved to CRISM bandpasses [*Murchie et al.*, 2007].

2.2.2-b Sensitivity Analysis

For each spectrum, initial best-fit parameters were obtained by inspection and a chi-squared (X^2) value calculated:

$$\chi^2 = \sum_{\lambda=1}^{n} \frac{(r_o - r_m)^2}{r_o^2}$$

Equation 2.4

where r_o is the observed bidirectional reflectance, r_m is the modeled bidirectional reflectance, and the summation was carried out over all wavelengths (except between 1.95 μm and 2.1 μm, an area sometimes disrupted by residual CO_2 gas bands in DISORT-derived spectra).

Because these models include multiple variables, multiple sets of parameters can produce low X^2 values. We therefore consider the initial best-fit set of parameters a local minimum in X^2 space. To test for the existence of other local minima, we performed a sensitivity analysis: one parameter was fixed while the others were allowed to vary and a new X^2 was calculated; then, the fixed parameter was increased to a higher or lower fixed value, and the others allowed to vary, and so on until the parameter had been assigned each of its physically reasonable values. This process resulted in X^2 as a function of the fixed parameter, as illustrated in Table 2.1. For each spectrum, this process was carried out for each parameter (grain size, mass ratio, or upper layer thickness), and local minima identified. Of the local minima identified, some could be discarded because the depths of the major absorptions did not match. Some could be discarded because of physical constraints (for example, the thickness of the overlying layer could not be less than the diameter of the particles that made it up). After discarding the parameter sets that were physically unreasonable and those that produced band depths that were too shallow or too deep, only one set of parameters was left for most FRTs. Some FRTs (FRT0000939A, FRT000093F5, FRT0000A07E) had multiple sets of parameters; these were discarded as being too poorly constrained. Only those with a single set of best-fit parameters are analyzed here.

We further tested each best-fit set of parameters to determine which variables within each fit were well constrained and which were poorly constrained. To do this, one variable was varied in steps away from its original value and the fitting process repeated for each step. If the variable was well-constrained, the chi-squared value increased quickly as the value moved away from the best-fit value (*e.g.*, Figure 2.6). For poorly constrained variables, chi-squared values increased slowly away from the best fit.

Sensitivity analysis results are presented in Section 2.3.4 below.

2.3 Spectral Fitting – Results

2.3.1 Summer to Fall

Representative summer and early fall CRISM spectra are plotted in Figure 2.5. As previously reported by *Seelos et al.,* [2008], Phoenix ice-free summer spectra show a ferric edge in the VNIR, indicating contributions from nanophase iron oxides, and a reflectance drop-off starting at 2.3-μm, which is typical of the northern plains and has been interpreted as small amounts of water adsorbed onto the surface [*e.g., Jouglet et al., 2007; Milliken et al.,* 2007]. Ice-free summer spectra were best modeled as a thin layer (~95 μm thick) of 15 μm soil overlying coarser-grained soil (~2 mm), based on use of the palagonite optical constants. This result is not inconsistent with Phoenix Optical Microscope (OM) and Robotic Arm Camera (RAC) results, which indicate an abundance of translucent reddish grains of silt to sand sizes, appearing in undisturbed state as aggregates of larger particles [*Arvidson et al., 2009; Pike et al., 2009*].

CRISM data show water ice forming near the Phoenix landing site in late summer, with 1.5- and 2-μm bands appearing by L_s ~167˚ (Figure 2.5). The late summer spectra were best fit by a 1:1 ice:soil layer of 50 μm H_2O ice with 15 μm soil particles over sand-sized particles (2 mm), consistent with dirty ice overlying soil deposits (X^2=0.354). The thickness of the icy layer increases from ~90 μm to ~115 μm from L_s~167˚ to L_s~177˚, but the grain sizes and ice:soil ratio stay the same.

2.3.2 Winter

CRISM obtained only one winter spectrum (L_s ~344˚) due to the presence of the polar hood. This spectrum is dominated by CO_2 ice (Figure 2.6). The 2-μm triplet is saturated, as are the 1.43 and 2.12 μm bands. The 1.2-μm doublet and 1.87, 2.283, 2.34 μm bands – all of which are only present in CO_2 ice, not in the gas phase – are all strong. There are also shallow H_2O ice absorptions, including a broad 1.5 μm band, a broadening at 2.0 μm beyond what would be expected of CO_2 ice, and the 2.3-μm turndown.

Atmospheric corrections were run on this observation; however, because the observation's high incidence angle (81.3˚ relative to the areoid) violated the DISORT assumption that the atmosphere behaves as series of plane parallel layers, absolute bidirectional reflectances could not be obtained. The observation could not be accurately modeled using the non-linear mixing model. However, information on grain sizes and abundances could still be extracted from the spectrum using only the absorption band depths.

CO_2 ice grain sizes were estimated by comparing the depth of the 2.283 μm ice-only absorption in the observation (37.7%) to band depths modeled using the non-linear mixing model. The 2.283 μm CO_2 ice band depth best matched models of CO_2 ice with "grain sizes" of 30 cm. (At this scale, the CO_2 can be thought of as a solid slab with long light pathlengths, rather than individual grains). Water ice grain sizes were estimated by comparing the 1.5 μm band depth in the observation (24.7%) and the slope between 2.2 and 2.5 μm to models, and best matched models with a layer of 100- μm grain size water ice overlying the CO_2 slab (Figure 2.6).

2.3.3 Spring

The earliest springtime CRISM FRT was taken 72 sols after the winter observation, at L_s ~11˚, and the spectrum is quite different than the winter spectrum (Figure 2.7A). H_2O ice absorptions at 1.5 and 2.0 μm dominate, and the 2.3-2.6 region is steeply negative, corresponding to coarser-grained H_2O ice (~100 μm). CO_2 ice absorptions are still apparent at 1.43, 2.28, and 2.34 μm. The overall reflectance is higher than observed in spectra acquired during the winter: rising to a bidirectional reflectance of ~0.5 at L_s ~14˚, then steadily declining again, an effect seen across the entire retreating seasonal cap [*Kieffer et al.,* 2000].

The spectral dominance of the H_2O ice does not mean that H_2O ice dominates by mass: only a small amount of H_2O ice is needed to produce absorptions because of its high absorption coefficients. For example, only 1 mg/cm^2 of water ice (100 μm grain size) overlying CO_2 ice (1 mm grain size) will produce water ice absorptions (Figure 2.8), or just 0.05 wt% if the two are intimately mixed (Figure 2.8). Water ice cold-trapped onto the surface during winter would produce weak H_2O absorptions as long as the CO_2 was abundant and coarse-grained; however, as the CO_2 sublimates and disintegrates into smaller grains (as seen elsewhere on both polar caps, presumably resulting from an increase in solar insulation, *e.g.* *Titus et al.*, 2001), the same amount of water ice will dominate the spectrum.

The early spring observations are initially well-fit by an intimate mixture of ~0.1 wt% water ice (100 μm grain size), 0.003 wt% soil (3 μm grain size), and slab CO_2 ice (~20 cm pathlengths), overlying a layer of soil with grain sizes of ~2 mm (Figure 2.7A). The ratios and grain sizes of the water ice and soil remain fairly constant throughout the spring; however, the grain sizes of the CO_2 ice layer gradually decreases as the CO_2 ice sublimates (Table 2.2).

As the CO_2 ice disappeared, the H_2O ice also sublimated, contributing to the mid-spring hazes observed in HiRISE and CRISM observations during this time. CO_2 ice absorptions disappear from DISORT-corrected FRTs at L_s ~26˚; however, features continue to show up in ratioed spectra until L_s ~34˚. After L_s~26˚, water ice is completely dominating the spectrum and masking the small CO_2 ice features that remain. This is consistent with *Kieffer and Titus's* [2001] estimate that the "crocus date" (disappearance of CO_2 frost) at 68˚N should be between L_s ~29˚ and L_s ~48˚. The water ice finally disappears around L_s ~59˚.

2.3.4 Sensitivity Analysis Results

A representative sensitivity analysis for a summer ice-free spectrum is shown in Figure 2.9A-B. Component grain sizes are well-constrained on the lower end, but poorly constrained on the higher end. The thickness of the top layer is likewise well-constrained on the lower end, but less well-constrained on the upper end.

Sensitivity analysis was not performed on the winter spectrum, since conclusions about grain sizes were based on absorption bands depths, instead of on the mixing model.

A representative sensitive analysis for spring is shown in Figure 2.9C-F. Grain sizes for H_2O ice and soil are well-constrained; however, CO_2 ice "grain size" is poorly constrained on the upper limit. The thickness of the CO_2 slab is likewise well-defined (Figure 2.9F).

2.4 HiRISE Analysis – Data Set and Methods

The spring defrosting period was also monitored with images from HiRISE [*McEwen et al.*, 2007], which have 0.25- to 1.3-m/pixel size and swath widths of ~6 km. The R (570-830 nm) and BG (<580 nm) filter channels were used to monitor annual changes in surface color and the R channel for ice depth measurements, because it has the widest swath width.

spring ice depth was calculated by comparing rock "heights" in spring and summer images. Rock shadow lengths in summer HiRISE images were measured parallel to solar azimuth direction, and, with the incidence angles from the HiRISE geometry files, the height of the rock was calculated. The shadow lengths of the same rocks were measured in spring, and, with the new incidence angles, the new rock “heights” were calculated. The difference in summer and spring rock “heights” gives the ice depth, assuming that there was not significant ice on top of the rocks (Figure 2.10A-B). This is a valid assumption, because fine-scale morphology is visible on the tops of large rocks in both summer and spring (Figure 2.10E and F), demonstrating that the tops are relatively uncovered.

It is possible that the high thermal inertia of the rocks also retards ice formation around them. For example, *Sizemore and Mellon* [2006] showed that a rock’s influence on the ice table extends ~1-2 rock radii, which is greater than the area usually covered by a rock shadow at typical HiRISE incidence angles. Rocks in many spring HiRISE images often have dark halos around them (e.g., Figure 2.10F) because of this effect. An ice-free moat around a rock would make the measured shadows longer (Figure 2.10D), reducing the inferred depth of ice. Likewise, any ice on top of rocks would make them appear “taller” than they actually are (Figure 2.10C), reducing the inferred depth of ice. The shadow measurements therefore indicate minimum ice depths.

2.5 HiRISE – Results

2.5.1 Ice Depth

During winter, few HiRISE images were obtained near the landing site, due to the presence of the polar hood. The few that were obtained showed few rocks due to the thick layer of ice on the ground.

By L_s~3˚, the ice layer had become thin enough to expose large rocks, and shadow measurements indicated an ice depth of 34 ± 1 cm. The ice layer continued to thin through spring, reaching 5 ± 1 cm by L_s~37˚. The ice depth measurements obtained from HiRISE images are listed in Table 2.3.

2.5.2 Ice Sublimation Patterns

Our combined HiRISE and CRISM results show that ice does not sublimate uniformly from the Phoenix landing site region. Different sublimation rates are most noticeable over the polygonal terrain that covers this region. At the Phoenix landing site, polygons are usually small (3-6 m across) with troughs ~10 cm deep [*Mellon et al.,* 2008b]. HiRISE and CRISM observations during spring show that high-albedo ice begins disappearing from polygon centers as early as L_s ~18˚, and lingers in polygon troughs as late as L_s ~45˚ (Figure 2.11). A similar phenomenon is also observed in the retreat of the southern seasonal cap [*Kossacki and Markiewicz* 2002; *Kossacki et al.,* 2003].

It is possible that ice is being redistributed to polygon troughs, perhaps by wind. Another possibility is that the ice lingers in the troughs because of thermal inertia effects. Rock-free soil, which is prevalent in the troughs, has a low thermal conductivity (which dominates thermal inertia), meaning that a thick surface soil layer should conduct less summer heat into the subsurface than a denser surface. With less stored heat, the surface will cool faster in the fall and winter, allowing more ice to accumulate. If significant amounts of soil are trapped in polygon troughs by wind, the cooler surface would encourage CO_2 ice formation during fall and retard its sublimation in spring. A similar effect might be expected for the diurnal temperature cycle, as the troughs cool down faster at night. Trough shadowing might also play a role in retaining ice in troughs longer.

In addition to the polygons, defrosting rates differ among the geologic units that were described by *Seelos et al.,* [2008]. Lowland Dark and Knobby terrains lose ices first, followed by Block/Mesa terrain, then Highland Unit, then Lowland Bright Unit, and finally debris aprons surrounding plateaus (Figure 2.12). This probably results from higher thermal inertia surfaces that conduct more summer heat into the ground and release it slowly during winter and spring, raising annual mean surface temperatures, retarding ice formation, and speeding ice sublimation. Indeed, in THEMIS pre-dawn thermal IR images, the units that appear brightest (indicating high thermal inertias) are Lowland Dark and Knobby Terrain, which lose their ice first.

2.6 Discussion - Annual Evolution of Ices

In CRISM spectra, water ice first appears at L_s~167˚. The late-summer ice is best modeled as 50 μm diameter ice grains, and the presence of a 1.5 μm band makes it unlikely that these are atmospheric ice particles.

Late summer and early fall spectra lack evidence of CO_2 ice (L_s ~142˚-181˚). It is possible that CO_2 ice is present and masked by the strong H_2O ice absorptions - the H_2O-CO_2 ice modeling shows that 10-μm grain size water ice can hide up to 80 wt.% CO_2 in intimate mixture – however, this probably is not happening in early fall, as temperatures are still above the CO_2 condensation temperature of ~140K [*Kelly et al.,* 2006].

These results are consistent with a number of other observations. The late-summer onset of ice is consistent with TES temperature observations, which show that 68˚N reaches water condensation temperatures (<190K) at L_s ~164˚ [*Kieffer and Titus* 2001]. Additionally, the amount of water ice accumulating during this period is within the range of perceptible water vapor measured in this area during late summer [*e.g., Houben et al.,* 1997].

By winter, CRISM observations and modeling show a ~30 cm layer of CO_2 ice on the surface. Because of the deep ice-only absorptions seen in this spectrum, the CO_2 must have “grain sizes” on the order of 20 cm, indicating that this material is probably slab ice. The depth of the 1.5 μm band and the shape of the CRISM spectrum between 2.2 and 2.5 μm also indicate that some coarse-grained water ice is overlying the slab. The presence of water ice on top of the CO_2 slab indicates that the CO_2 slab is no longer growing at L_s~344˚.

The ~30 cm slab thickness is consistent with thermal models, which predict that at L_s~340˚, the surface should be covered with 170-350 kg/m^2 CO_2, depending on the depth of ground ice [*Mellon et al.*, 2008a]. Assuming a CO_2 ice solid density of 1590 kg/m^3 and a low porosity (30%), this translates to ~16-33 cm of CO_2 ice.

The long path lengths suggest that the ice is in slab form, which is consistent with a number of other observations. Based on physical models, CO_2 ice of any grain size is expected to quickly metamorphose into slab ice in the seasonal deposits [*Eluszkiewicz* 1993]. CO_2 slab ice has been invoked to explain a number of polar observations, including low-albedo, cold surfaces [*e.g. Kieffer et al.*, 2000; *Titus et al.*, 2001]. Additionally, Mars Global Surveyor gravity and topography data suggest a seasonal cap mean density close to ~910 kg/m^3, which corresponds to a porosity of only ~40% [*Smith et al.*, 2001], compared to ~70% porosity expected of freshly-fallen snow [*Eluszkiewicz et al.*, 2005].

If the CO_2 is in slab ice form, it might be possible to see through the ice to the underlying soil and fall-deposited water ice. Our modeling shows that a 30 cm-thick slab of perfectly pure CO_2 ice (*i.e.*, with no internal scattering surfaces like soil or crystal faces) is transparent at wavelengths <1.5 μm and in the 2.3 to 2.5 μm region. However, a transparent slab of CO_2 ice covering fall-deposited water ice and soil is a poor match for the CRISM winter observation, since it mutes the depth of the 1.5 μm absorption and the slope of the 2.2 – 2.5 μm region (Figure 2.13).

After the spring equinox, the ice slab is interpreted to break into smaller grains. CRISM observations and models show a steady decrease in the thickness of the CO_2 ice layer from 20 cm to 4 cm from L_s~11˚ to 34˚. This decrease matches ice depth measurements from HiRISE, which show the ice layer ~21 cm deep at L_s~11˚ to ~5 cm deep at L_s~47˚. The agreement between the ice layer thicknesses produced by the non-linear mixing model and ice layer thicknesses measured by from HiRISE images is good (Table 2.2 and Table 2.3).

The different rates of sublimation observed for polygon troughs and centers and for different geomorphic units may be responsible for the widely varying estimates for “crocus dates” from various data sets. Depending on the spatial resolution of the data set, and the criteria each is using to distinguish an ice-free surface (e.g., visual images, surface temperature, spectral properties), the seasonal cap may appear to be “gone” at different times.

2.7 Summary

This study analyzed CRISM spectra and HiRISE images taken over the Phoenix landing site from summer to early fall (L_s ~142˚-181˚) and late winter mid-spring (L_s ~344˚-75˚) for the year prior to Phoenix landing. Spectra were atmospherically-corrected using the DISORT radiative transfer method, and compared to non-linear mixing models of soil-H_2O-CO_2 mixtures. Matching summer/spring pairs of HiRISE images were used to calculate ice depths based on changes in rock shadow length. This study draws the following conclusions about seasonal ice at the Phoenix landing site:

1) Water ice precedes CO_2 ice during the onset of the seasonal cap. Water ice first appears on the surface at L_s ~167˚. CO_2 ice begins to condense at L_s >181˚.
2) During winter, the seasonal cap at the Phoenix landing site consists of a ~30 cm-thick layer of nearly pure CO_2 ice, probably in the form of slab ice. A thin layer ~100 μm water ice overlies the CO_2 slab. The surface appears slightly red during winter from the soil contamination; however, we are not seeing through the ice to the underlying surface.
3) During spring, the CO_2 ice deteriorates into smaller grain sizes and sublimates, producing spectra that are increasingly dominated by water ice. Our modeling supports the hypothesis that the spring water ice annulus is due to water ice cold-trapped onto the surface of the CO_2 ice, not due to an underlying layer of water ice that is exposed during CO_2 sublimation.
4) CO_2 ice finally disappears after L_s ~34˚. The water ice finally disappears around L_s ~59˚.
5) Ice sublimation is not uniform: it disappears first from polygon centers, and only later from troughs. This probably results from soil trapped in polygon

troughs, lowering the thermal inertia and surface temperature, or due to re-distribution by wind.

6) Ice sublimation also varies among geomorphic units. In the Region D geomorphic units defined by *Seelos et al.,* [2008], ice disappears first from the Lowland Dark and Knobby units, then Block/Mesa, then Highland, then Lowland Bright, and finally from debris aprons. This pattern also likely results from thermal inertia differences.

Tables

Table 2.1 - Example of a
sensitivity analysis for
FRT0000419C.

Sensitivity analysis shown for a
subset of one parameter. For
each run, the fixed parameter (in this
case, soil grain size of the upper
layer) was held constant and the
other variables allowed to
adjust until a best-fit for that grain
size was found, then that grain
size was increased
incrementally. The
lowest chi- squared value for this
example occurred for soil grain
sizes of 15 μm, a combination of
parameters that also produced a 1.5

	Upper Layer				Lower Layer				Results	
Soil Grain Size (microns)	Water Ice Grain Size (microns)	Soil Mass Fraction	Water Ice Mass Fraction	Upper Layer Thickness	Soil Grain Size (mm)	Water Ice Grain Size (microns)	Soil Mass Fraction	Water Ice Mass Fraction	Chi-Squared	1.5 micron band depth
1	80	0.1	0.9	1.3	3	0	1	0	0.214	0.071
5	70	0.1	0.9	3.1	3	0	1	0	0.152	0.161
10	80	0.3	0.7	3.3	2	0	1	0	0.205	0.132
15	**70**	**0.5**	**0.5**	**3.1**	**2**	**0**	**1**	**0**	**0.041**	**0.097**
20	80	0.7	0.3	4.2	3	0	1	0	0.283	0.073
30	100	0.8	0.2	5.5	2	0	1	0	0.073	0.066
50	60	0.4	0.6	6.1	2	0	1	0	0.119	0.140
100	50	0.7	0.3	6.9	3	0	1	0	0.295	0.131
150	70	0.5	0.5	7.1	3	0	1	0	0.402	0.207
250	50	0.4	0.6	6.8	3	0	1	0	0.176	0.165

μm band depth (0.097) comparable to the actual 1.5 μm band depth for FRT0000419C (0.095). Soil grain size of 30 μm also produced a low chi-squared value (0.073); however, that set of parameters produced too small of a 1.5 μm band depth (0.066), and so was not considered a good solution.

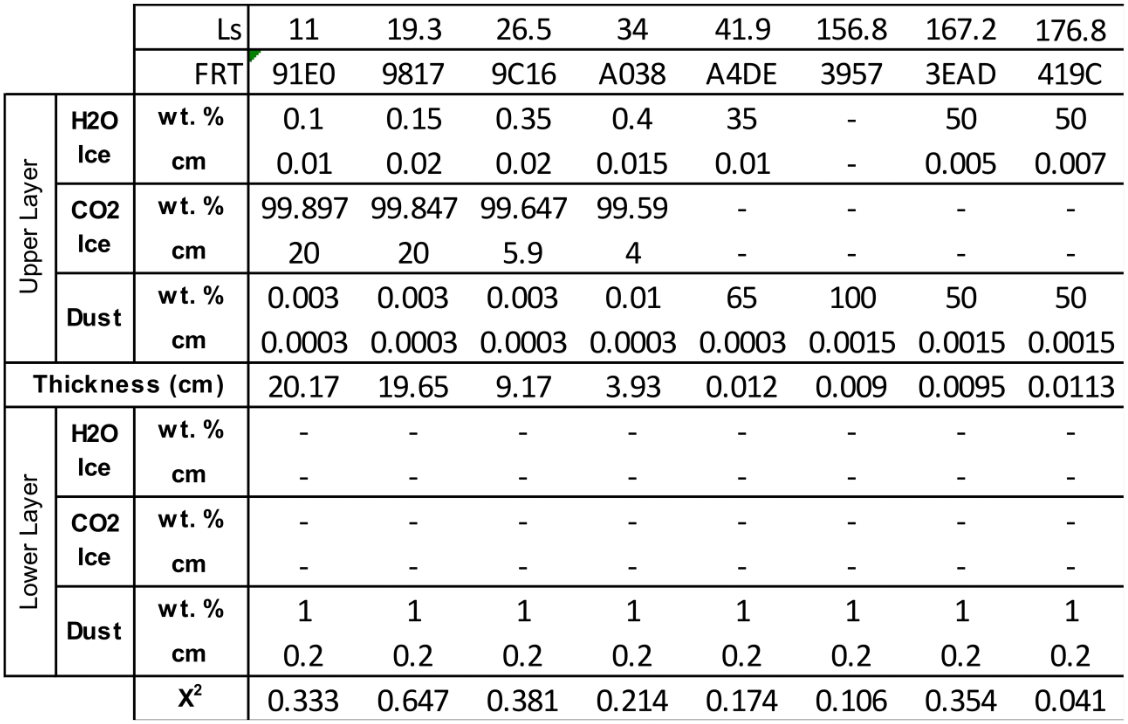

		Ls	11	19.3	26.5	34	41.9	156.8	167.2	176.8
		FRT	91E0	9817	9C16	A038	A4DE	3957	3EAD	419C
Upper Layer	H2O Ice	wt. %	0.1	0.15	0.35	0.4	35	-	50	50
		cm	0.01	0.02	0.02	0.015	0.01	-	0.005	0.007
	CO2 Ice	wt. %	99.897	99.847	99.647	99.59	-	-	-	-
		cm	20	20	5.9	4	-	-	-	-
	Dust	wt. %	0.003	0.003	0.003	0.01	65	100	50	50
		cm	0.0003	0.0003	0.0003	0.0003	0.0003	0.0015	0.0015	0.0015
Thickness (cm)			20.17	19.65	9.17	3.93	0.012	0.009	0.0095	0.0113
Lower Layer	H2O Ice	wt. %	-	-	-	-	-	-	-	-
		cm	-	-	-	-	-	-	-	-
	CO2 Ice	wt. %	-	-	-	-	-	-	-	-
		cm	-	-	-	-	-	-	-	-
	Dust	wt. %	1	1	1	1	1	1	1	1
		cm	0.2	0.2	0.2	0.2	0.2	0.2	0.2	0.2
		X^2	0.333	0.647	0.381	0.214	0.174	0.106	0.354	0.041

Table 2.2 - Modeling results for representative FRTs.

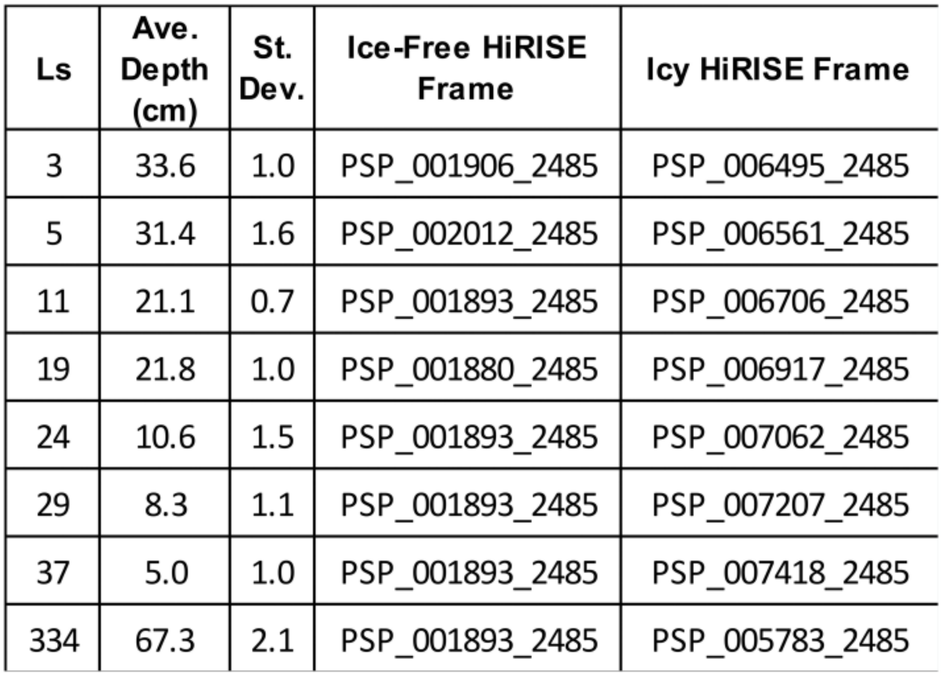

Ls	Ave. Depth (cm)	St. Dev.	Ice-Free HiRISE Frame	Icy HiRISE Frame
3	33.6	1.0	PSP_001906_2485	PSP_006495_2485
5	31.4	1.6	PSP_002012_2485	PSP_006561_2485
11	21.1	0.7	PSP_001893_2485	PSP_006706_2485
19	21.8	1.0	PSP_001880_2485	PSP_006917_2485
24	10.6	1.5	PSP_001893_2485	PSP_007062_2485
29	8.3	1.1	PSP_001893_2485	PSP_007207_2485
37	5.0	1.0	PSP_001893_2485	PSP_007418_2485
334	67.3	2.1	PSP_001893_2485	PSP_005783_2485

Table 2.3 - Ice depths from HiRISE measurements.

Figures

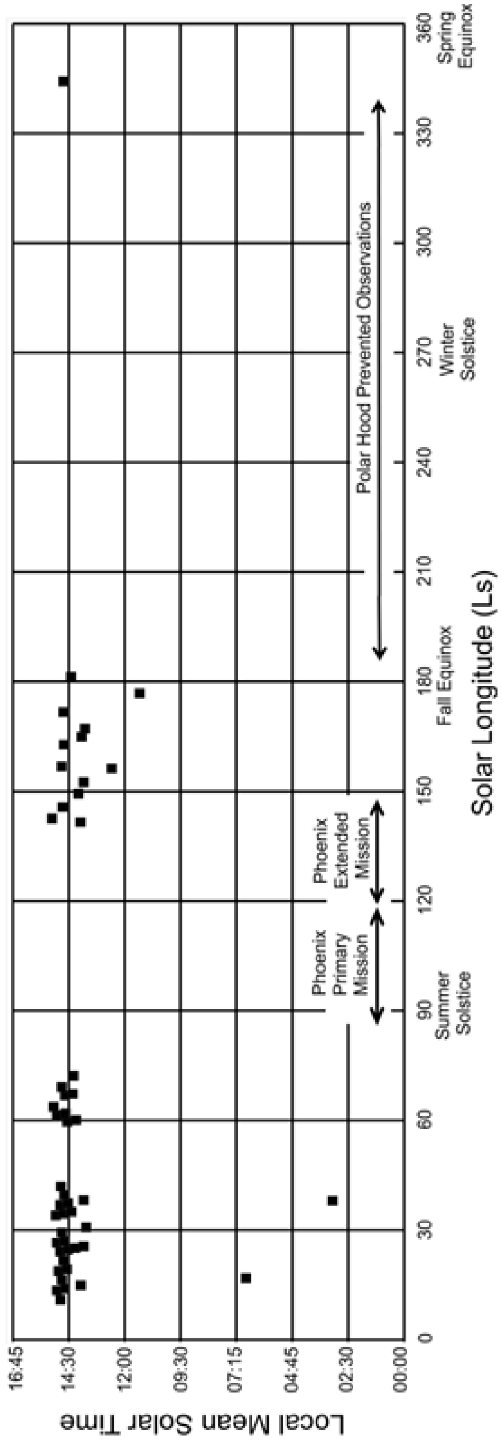
Local Mean Solar Time
16:45
14:30
12:00
09:30
07:15
04:45
02:30
00:00
Solar Longitude (Ls)
0
30
60
90
Summer Solstice
120
150
180
Fall Equinox
210
240
270
Winter Solstice
300
330
360
Spring Equinox
Phoenix Primary Mission
Phoenix Extended Mission
Polar Hood Prevented Observations

Figure 2.1 - CRISM FRT coverage.

Coverage over solar longitude (L_S) and local mean solar time (LMST). With only three exceptions, all of the FRTs used in this study were acquired between 13:30-15:00 LMST. Most of the observations were acquired during spring (L_s ~0˚-90˚) or late summer (L_s ~90˚-180˚).

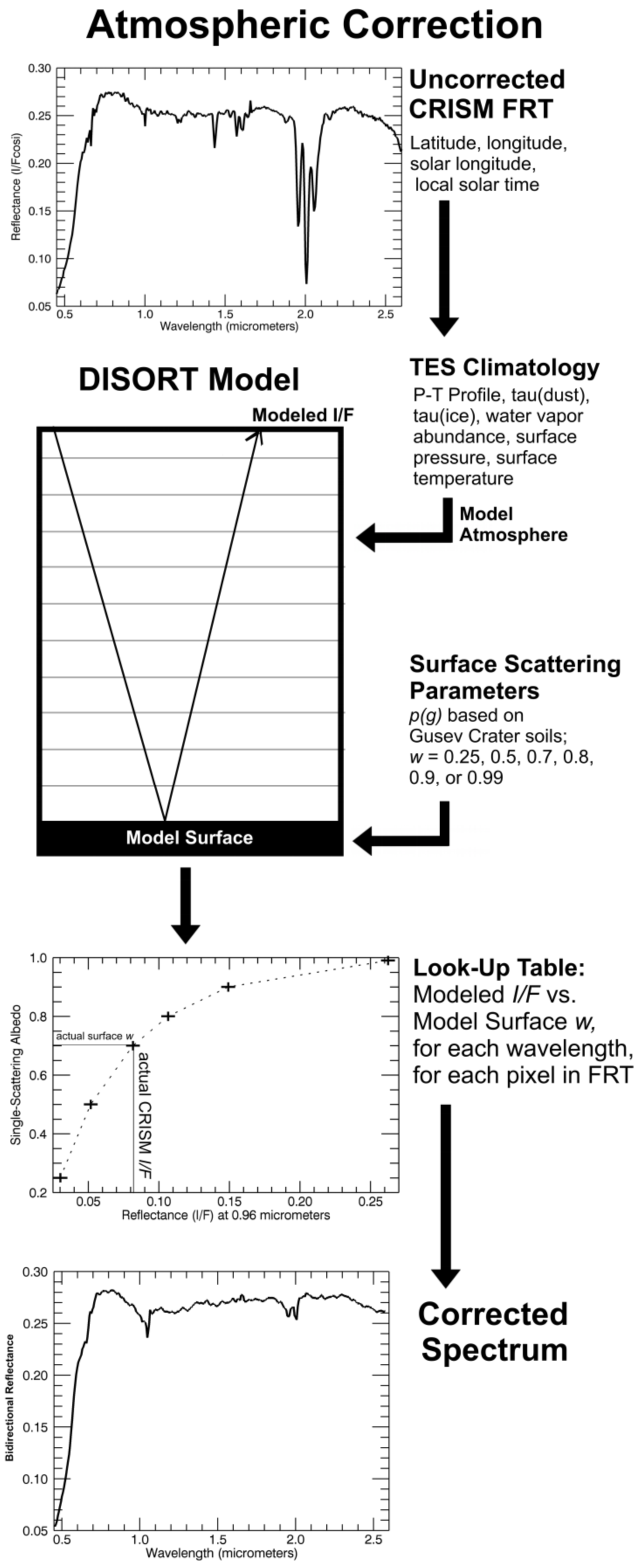
Atmospheric Correction
Uncorrected CRISM FRT
Latitude, longitude, solar longitude, local solar time
Reflectance (I/Fcosi)
0.30
0.25
0.20
0.15
0.10
0.05
0.5
1.0
1.5
2.0
2.5
Wavelength (micrometers)
DISORT Model
Modeled I/F
Model Surface
TES Climatology
P-T Profile, tau(dust), tau(ice), water vapor abundance, surface pressure, surface temperature
Model Atmosphere
Surface Scattering Parameters
p(g) based on Gusev Crater soils;
w = 0.25, 0.5, 0.7, 0.8, 0.9, or 0.99
Look-Up Table:
Modeled I/F vs. Model Surface w,
for each wavelength,
for each pixel in FRT
Single-Scattering Albedo
1.0
0.8
0.6
0.4
0.2
actual surface w
actual CRISM I/F
0.05
0.10
0.15
0.20
0.25
Reflectance (I/F) at 0.96 micrometers
Corrected Spectrum
Bidirectional Reflectance
0.30
0.25
0.20
0.15
0.10
0.05
0.5
1.0
1.5
2.0
2.5
Wavelength (micrometers)

Figure 2.2 - The atmospheric correction process for CRISM FRTs.

Based on each observation's latitude, longitude, and time of observation, historical TES climatology data was used to estimate atmospheric conditions at the time of observation, including a pressure-temperature profile, ice and dust optical depths, and water vapor abundances. This atmospheric profile was used in a DISORT model, along with surface scattering parameters based on Gusev Crater soils, to calculate the radiance at the top of the atmosphere for each CRISM wavelength. Six DISORTs were run for each cube, varying the surface single-scattering albedo, and a look-up table created to relate single-scattering albedo to *I/F*.

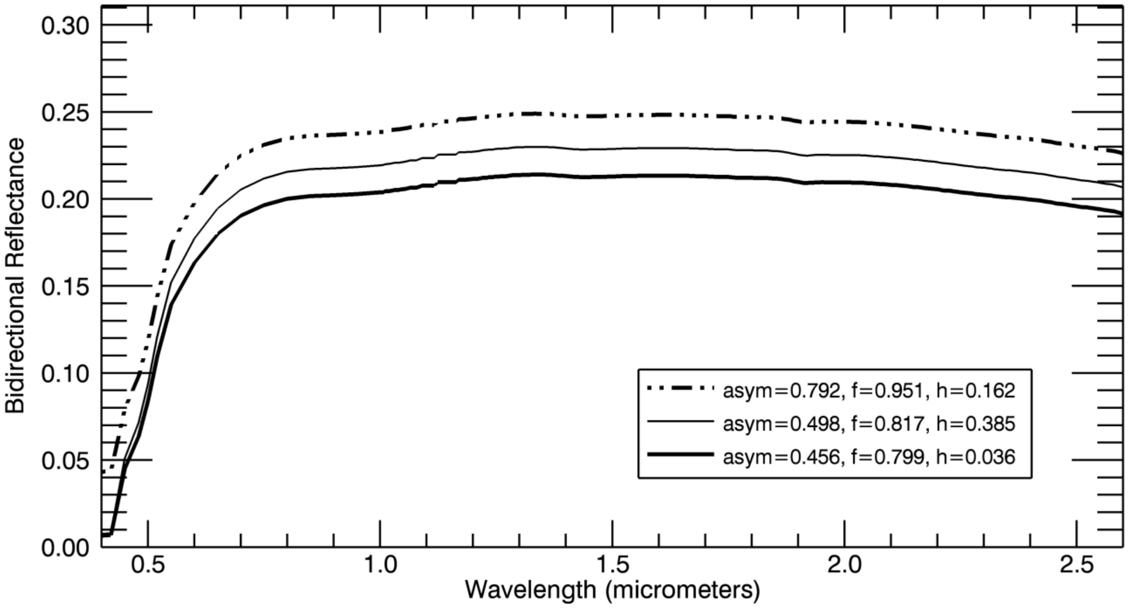

Figure 2.3 – Effects of varying surface phase function.

Model results of 10- μm diameter palagonite with varying surface scattering parameters. The scattering parameters were derived from various materials at the Gusev Crater landing site by Johnson et al., [2006] and are (top) Sol 102-103 Gray Rock endmember, (middle) Sol 212-225 Soil endmember, and (bottom), Sol 212-225 Red Rock endmember.

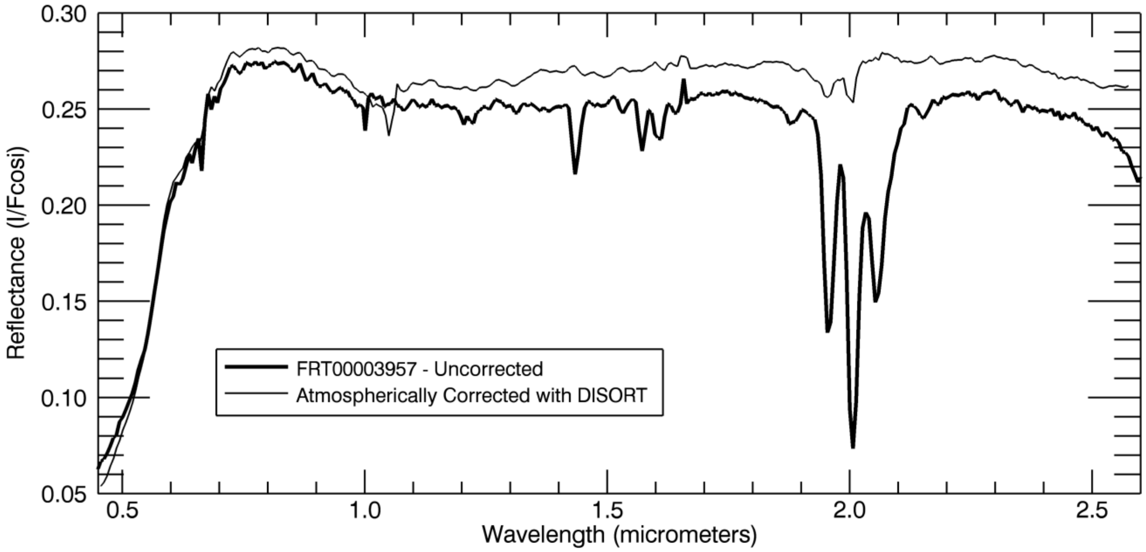

Figure 2.4 – Raw I/F vs. DISORT spectrum.

Comparison of DISORT-corrected CRISM spectrum (thin line) and original, uncorrected spectrum (thick line). The small hashes in the corrected spectrum are due to residual CO_2 gas from the correction.

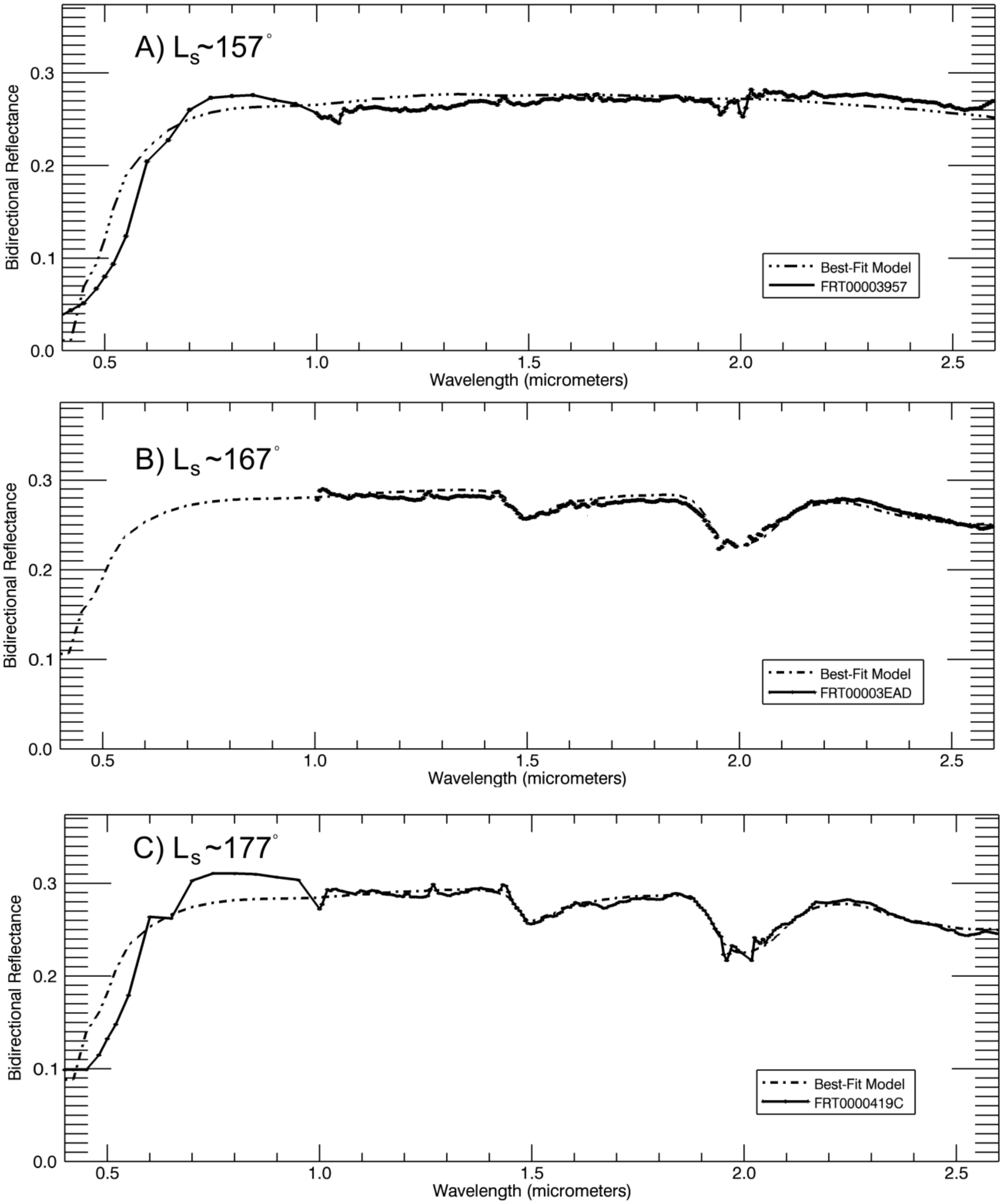

Figure 2.5 - Late summer spectra over the Phoenix landing site.

A) No ice has yet formed. B) A 1.5 μm and 2.0 μm absorption illustrate that water ice has begun to condense. C) The 1.5 μm and 2.0 μm absorptions become stronger. Model parameters for these observations are given in Table 2.2.

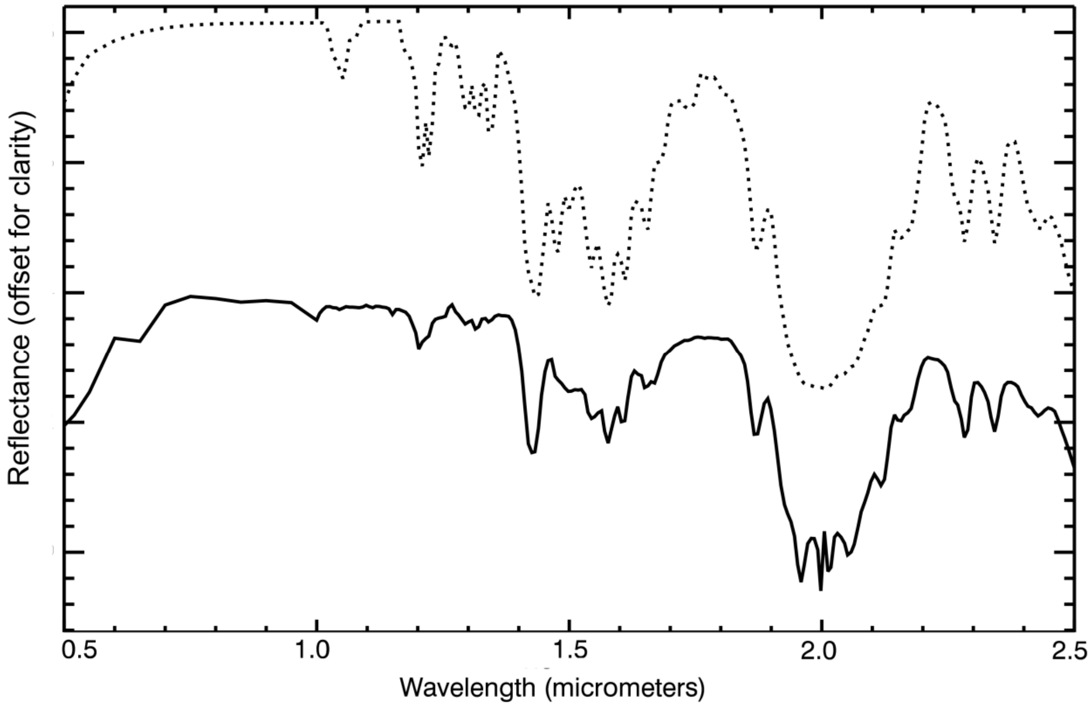

Figure 2.6 - winter CRISM observation over Phoenix site vs. model.

CRISM observation is the solid curve, and model results the dotted curve. DISORT corrections have removed most of the observation's CO_2¬ gas bands, but, due to the observation's high incidence angle, it was not possible to calculate absolute bidirectional reflectances for this observation.

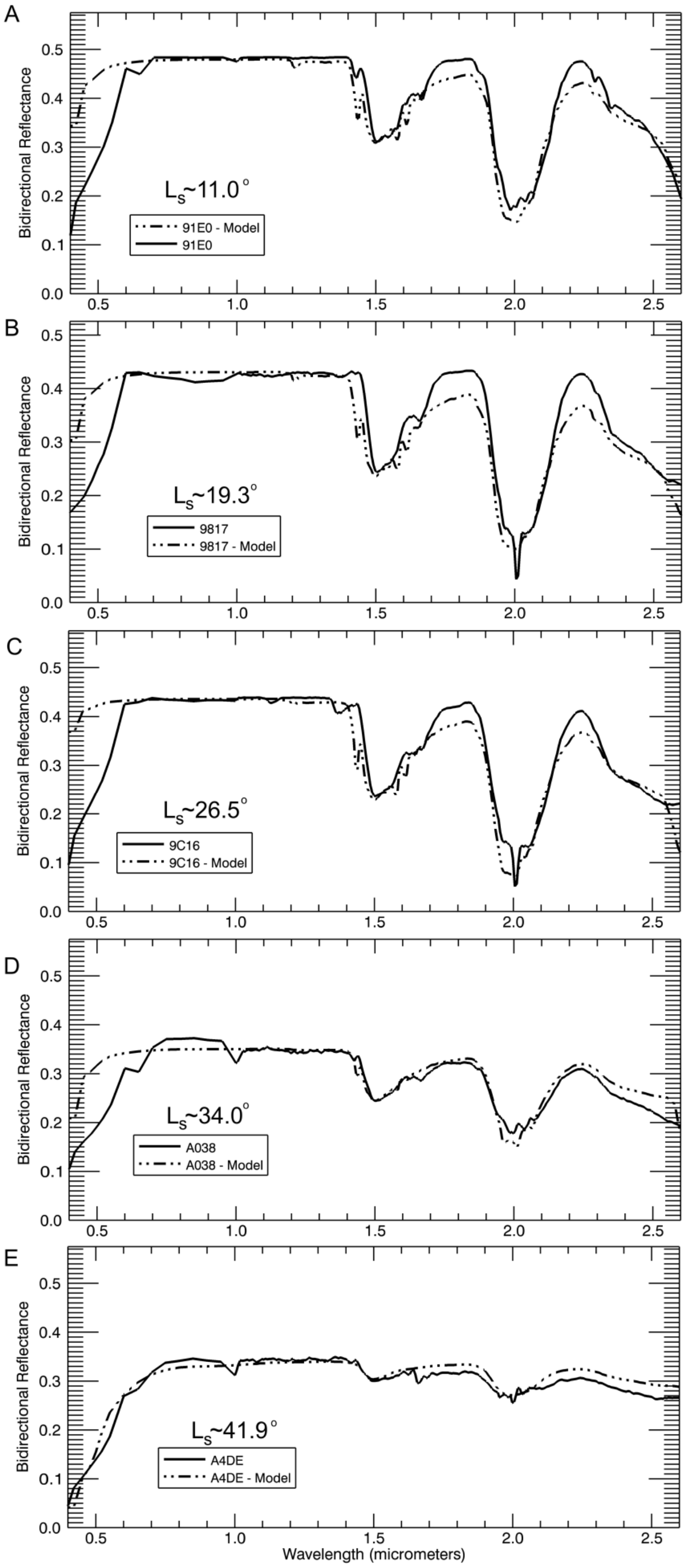
A
Bidirectional Reflectance
L_S~11.0°
91E0 - Model
91E0
B
L_S~19.3°
9817
9817 - Model
C
L_S~26.5°
9C16
9C16 - Model
D
L_S~34.0°
A038
A038 - Model
E
L_S~41.9°
A4DE
A4DE - Model
0.0
0.1
0.2
0.3
0.4
0.5
0.5
1.0
1.5
2.0
2.5
Wavelength (micrometers)

Figure 2.7 - spring CRISM observations over Phoenix site vs. model.

CRISM observations are solid lines, and model results are dotted lines. Water ice dominates spectra in the early spring; however, CO_2 ice-only absorptions are still visible through L_s~19˚. Model parameters for these observations are given in Table 2.2.

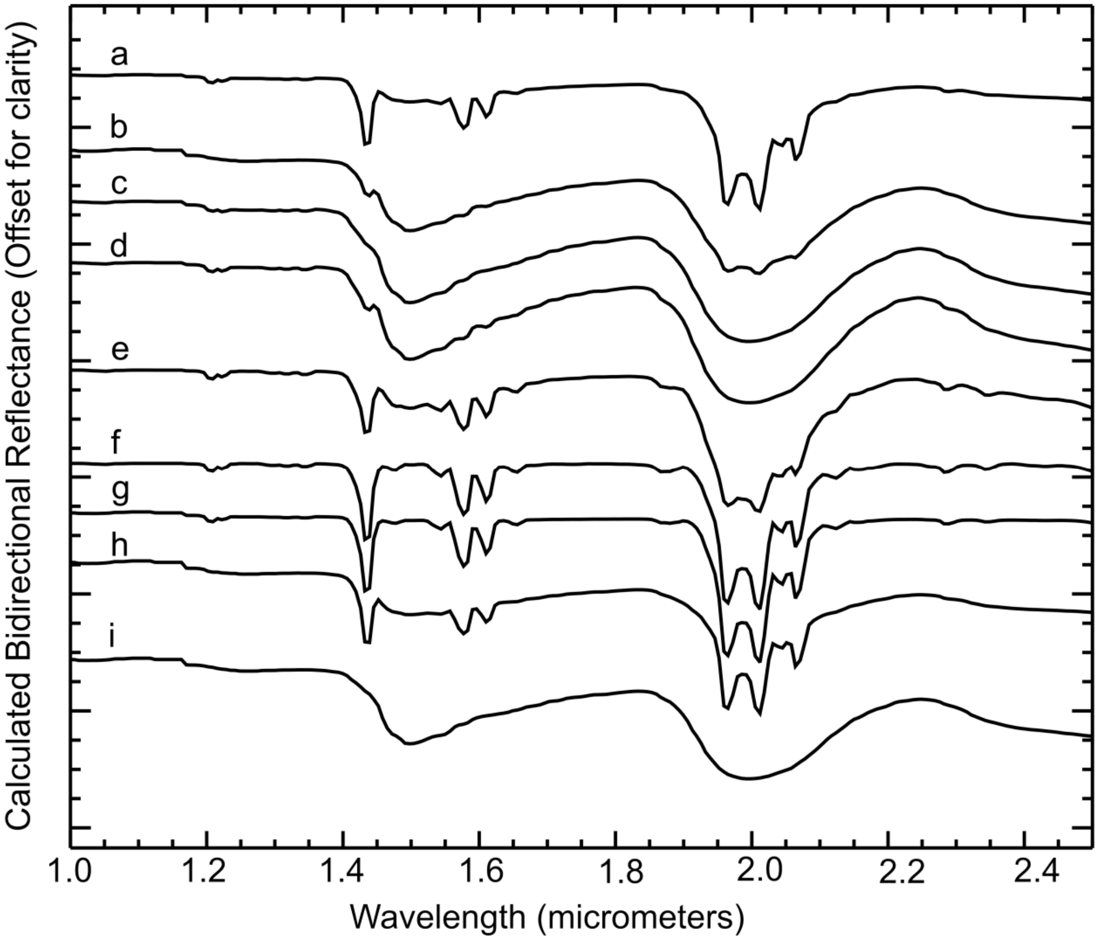

Figure 2.8 - Modeled results of intimate mixtures.

Mixtures of CO_2 ice and water ice are represented in a) and b), and layers of water ice on top of CO_2 ice (c, d, and e), and layers of CO_2 ice on top of water ice (g and h). An overlying layer of water ice more than 5 mg/cm^2 thick is sufficient to completely mask CO_2 ice absorptions; however, an overlying layer of CO_2 ice must be thicker than 1000 mg/cm^2 to completely mask water ice absorptions. A) Intimate mixture of

0.05 wt% water ice (10 μm grain size) + 99.95 wt% CO_2 ice (1mm grain size). The water ice absorptions are just barely visible. B) Intimate mixture of 5 wt% water ice (10 μm grain size) + 95 wt% CO_2 ice (1mm grain size). The CO_2 ice features are almost completely masked. C) 10 mg/cm^2 of water ice (10 μm grain size) overlying CO_2 ice (1 mm grain size). The underlying CO_2 is completely masked. D) 5 mg/cm^2 of water ice (10 μm grain size) overlying CO_2 ice (1 mm grain size). Some underlying CO_2 ice features are beginning to show up. E) 1 mg/cm^2 of water ice (10 μm grain size) overlying CO_2 ice (1 mm grain size). CO_2 ice dominates, with small water ice absorptions. F) Pure CO_2 ice (1 mm). G) 5000 mg/cm^2 CO_2 (1 mm) overlying 10 μm ice, the water absorptions are almost entirely hidden. H) 500 mg/cm^2 CO_2 (1 mm) overlying 10 μm ice, the water ice absorptions are pronounced. I) Pure 10 μm water ice.

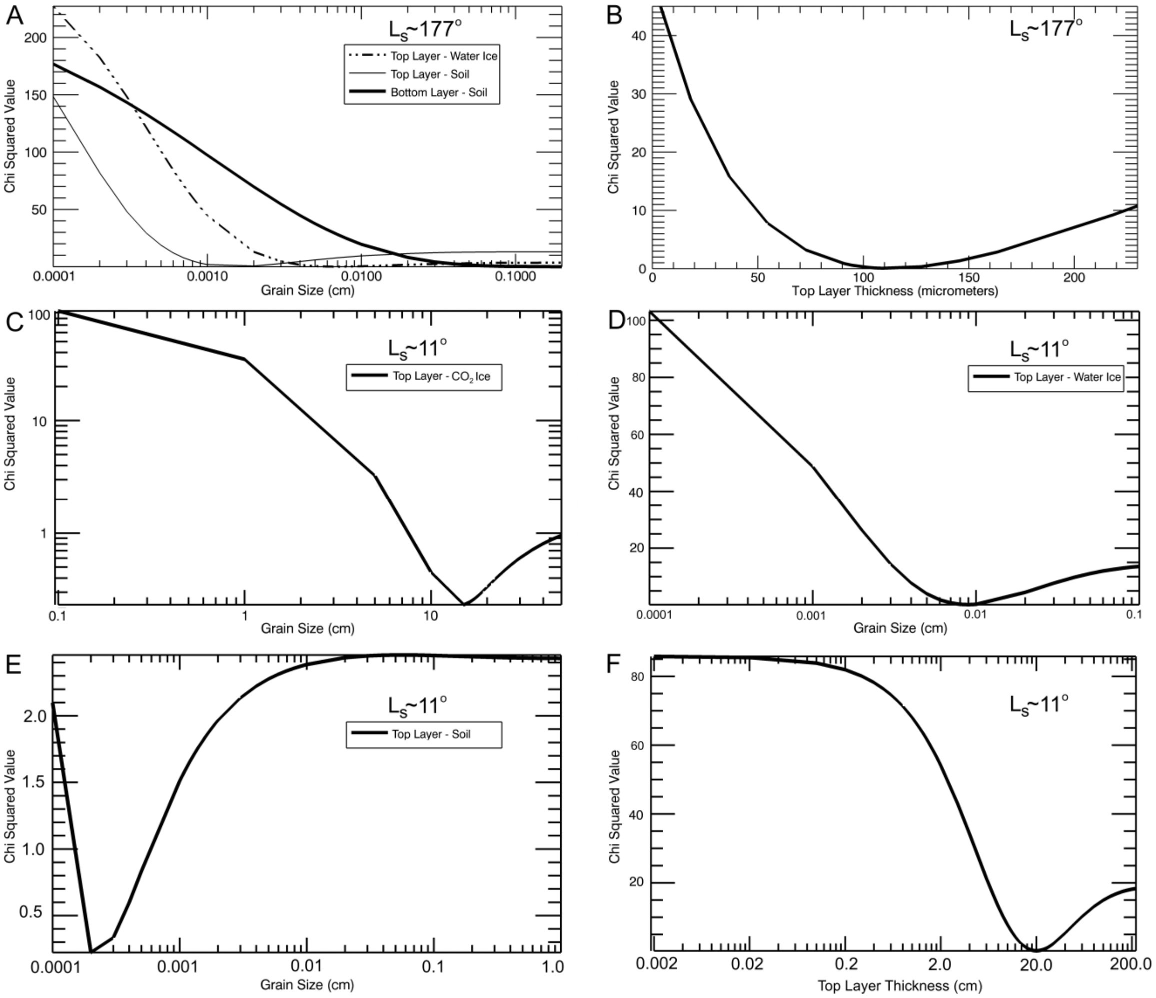

Figure 2.9 - Example of a sensitivity analysis.

For L_s~177˚ observation (A-B) and for L_s~11˚ observation (C-F).

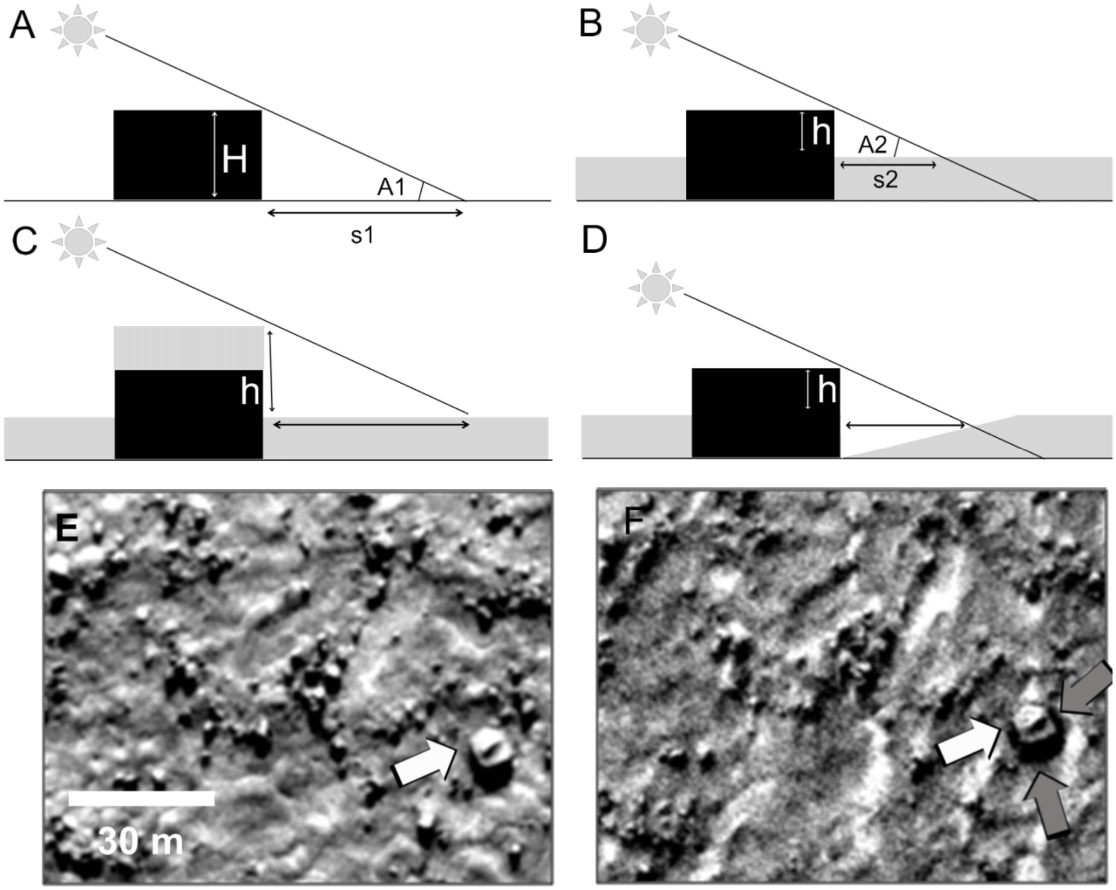

Figure 2.10 – Measuring snow depth.

A) Using rocks as "snowpoles." The rock shadow length (S1) was measured in summer, and the rock height estimated as H=tan(A1)*S1. B) The difference in heights between spring and summer was taken as the ice depth. C) Ice on top of the rock will make the shadow appear longer than what we would have measured without ice on top. This results in smaller calculated ice depths. D) A reduced-ice "moat" around a rock will make the shadow appear longer than what we would have measured without the moat. This results in smaller calculated ice depths. E) Subset of summer HiRISE image PSP_002012_2485. F) Subset of spring HiRISE image PSP_006561_2485, showing same scene. Rock marked with a white arrow shows surface morphology not obscured by ice. Gray arrows point to dark halo, which might indicate a reduced-ice moat around the rock.

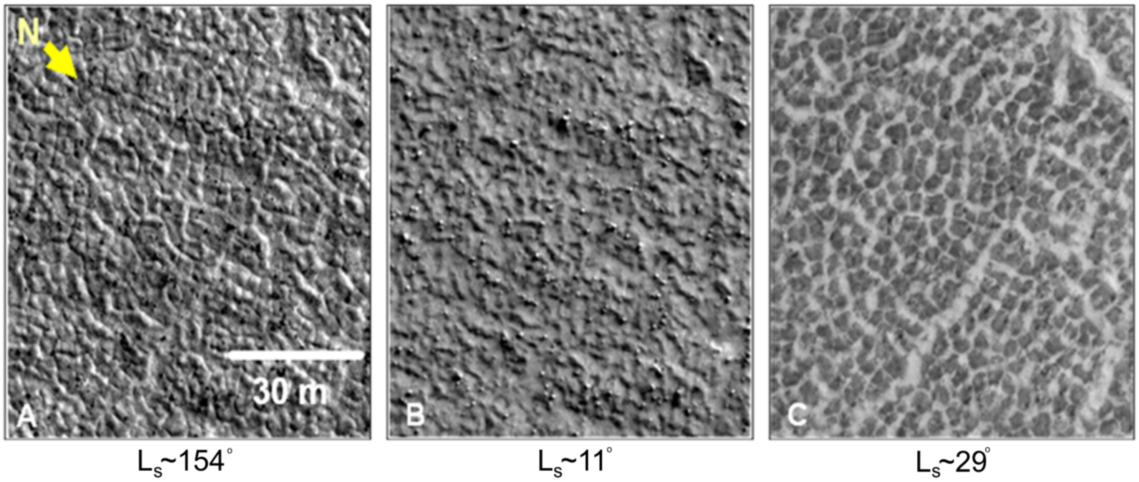

Figure 2.11 - HiRISE subsets illustrating frost coverage through time.

During the summer (left, L_s ~154˚), the surface is ice-free. In early spring (center, L_s ~11˚), the surface is completely covered with ice. By mid spring (L_s ~29˚), ice has disappeared from the centers of polygons, and is lingering in the polygon troughs.

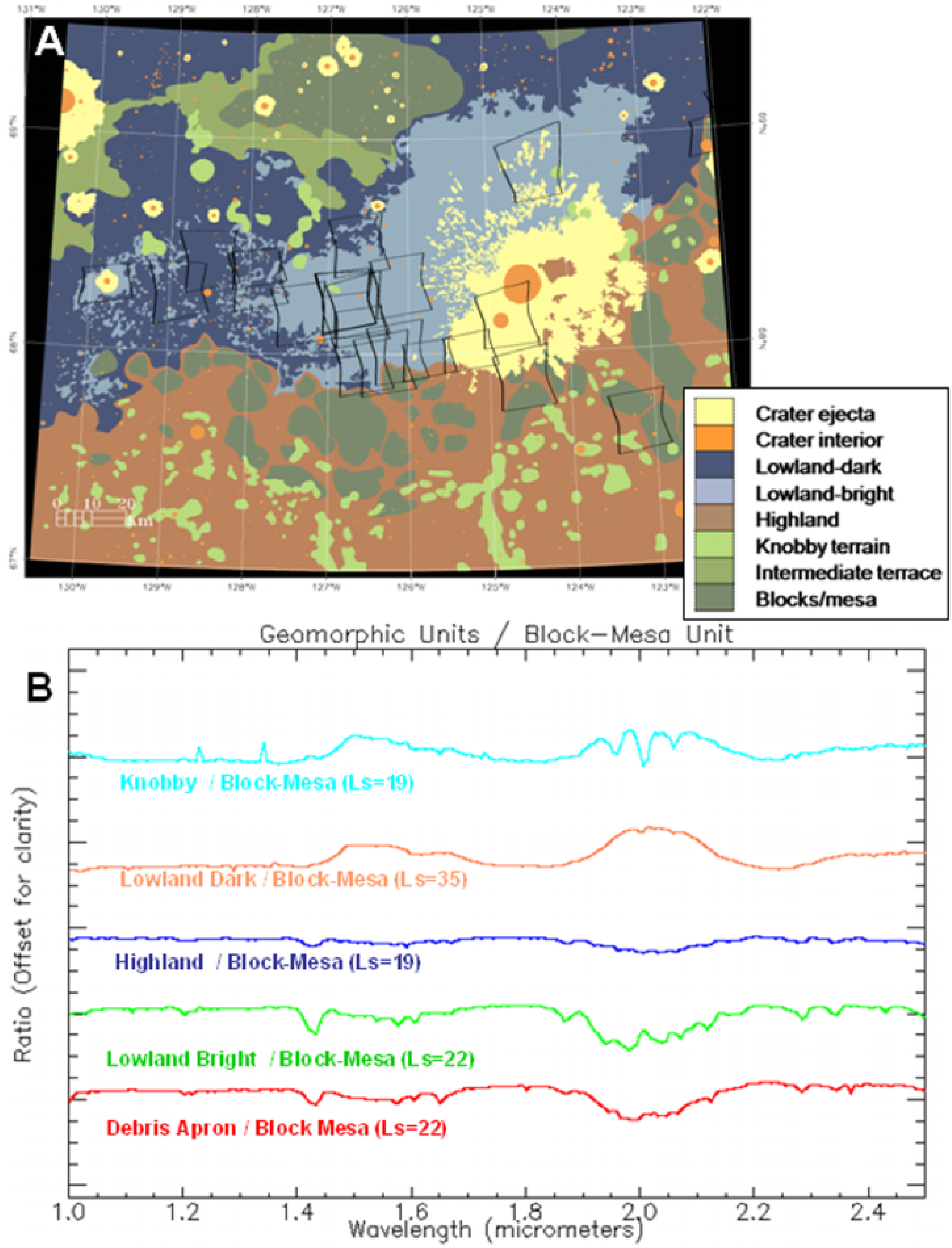
A
131°W
130°W
129°W
128°W
127°W
126°W
125°W
124°W
123°W
122°W
65°N
66°N
67°N
0 10 20 Km
🟨 Crater ejecta
🟧 Crater interior
🟦 Lowland-dark
🟦 Lowland-bright
🟫 Highland
🟩 Knobby terrain
🟩 Intermediate terrace
🟩 Blocks/mesa
Geomorphic Units / Block–Mesa Unit
B
Knobby / Block-Mesa (Ls=19)
Lowland Dark / Block-Mesa (Ls=35)
Highland / Block-Mesa (Ls=19)
Lowland Bright / Block-Mesa (Ls=22)
Debris Apron / Block Mesa (Ls=22)
Ratio (Offset for clarity)
1.0
1.2
1.4
1.6
1.8
2.0
2.2
2.4
Wavelength (micrometers)

Figure 2.12 - Defrosting patterns for different geomorphic units.

A) Geomorphic map of "Box 1" area in Region D (Kim Seelos, personal communication). Black boxes are CRISM FRT footprints. B) Ratios of different units. The Highland, Lowland Bright, and debris aprons all have deeper CO_2 absorptions than the Block/Mesa unit. Block/Mesa has deeper ice absorptions than both the Lowland Dark and Knobby terrains. By ratioing to the Block Mesa unit, we can contrast relative amount and retention of ices. Knobby and Lowland Dark material lose both CO_2 and water ice before the Block Mesa, as evidenced by the inverted shapes in the ratio. Highland, Lowland Bright, and debris aprons preserve ices longer than Block Mesa, as the ratios show typical ice features. From bottom to top, these ratios were made with CRISM observations FRT0000999F, FRT0000999F, FRT00009817, FRT0000A0C4, and FRT00009817.

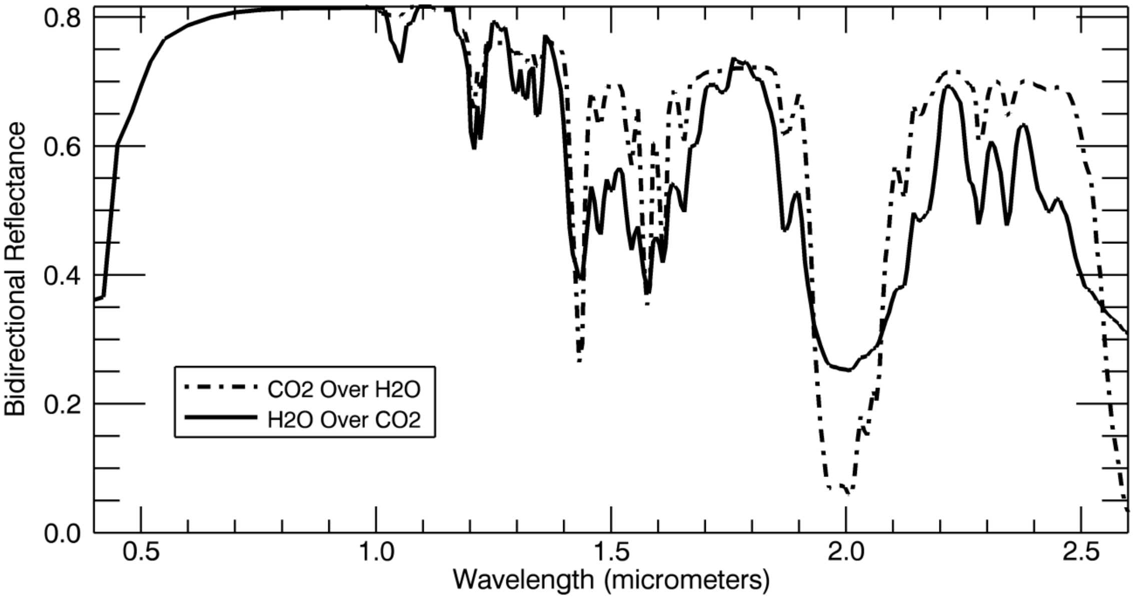

Figure 2.13 - CO_2 ice slab over water ice vs. a water ice layer over CO_2.

The CO_2 covering water ice almost entirely masks the H_2O underneath; however, a thin layer of water ice over CO_2 allows CO_2 absorptions to show.

References

Aharonson, O. (2004) Sublimation at the base of a seasonal CO_2 slab on Mars. *Lunar Planet. Sci.*, 35, Abstract 1918.

Arvidson, R. E., J. L. Gooding, and H. J. Moore (1989), The Martian Surface as Imaged, Sampled, and Analyzed by the Viking Landers, *Reviews of Geophysics*, 27(1), 39–60.

Arvidson, R.E., D. Adams, G. Bonfiglio, P. Christensen, S. Cull, M. Golombek, J. Guinn, E. Guinness, T. Heet, R. Kirk, A. Knudson, M. Malin, M. Mellon, A. McEwen, A. Mushkin, T. Parker, F. Seelos, K. Seelos, P. Smith, D. Spencer, T. Stein, L. Tamppari (2008) Mars Exploration Program 2007 Phoenix landing site selection and characteristics. *Journal of Geophysical Research*, 113, E00A03, doi:10.1029/2007JE003021.

Arvidson, R.E., R. Bonitz, M. Robinson, J. Carsten, R. Volpe, A. Trebi-Ollennu, M. Mellon, P. Chu, K. Davis, J. Wilson, A. Shaw, R. Greenberger, K. Siebach, T. Stein, S. Cull, W. Goetz, R. Morris, D. Ming, H. Keller, M. Lemmon, H. Sizemore, M. Mehta (2009), Results from the Mars Phoenix Lander Robotic Arm experiment, *Journal of Geophysical Research*, 114, E00E02, doi:10.1029/2009JE003408.

Benson, J.L. and P.B. James (2005) Yearly comparisons of the martian polar caps: 1999-2003 Mars Orbiter Camera observations. *Icarus* 174: 513-523. DOI: 10.1016/j.icarus.2004.08.025

Bibring, J-P., Yves Langevin, Aline Gendrin, Brigitte Gondet, François Poulet, Michel Berthé, Alain Soufflot, Ray Arvidson, Nicolas Mangold, John Mustard, P. Drossart, the OMEGA team (2005) Mars surface diversity as revealed by OMEGA/Mars Express observations. *Science* 307: 1576. DOI: 10.1126/science.1108806

Byrne, S., Colin M. Dundas, Megan R. Kennedy, Michael T. Mellon, Alfred S. McEwen, Selby C. Cull, Ingrid J. Daubar, David E. Shean, Kimberly D. Seelos, Scott L. Murchie, Bruce A. Cantor, Raymond E. Arvidson, Kenneth S. Edgett, Andreas Reufer, Nicolas Thomas, Tanya N. Harrison, Liliya V. Posiolova, and Frank P. Seelos (2008) Interannual and seasonal behavior of Martian residual ice-cap albedo. *Planetary and Space Science*: 56(2): 194-211.

Clancy, R. T., S. W. Lee, G. R. Gladstone, W. W. McMillan, and T. Rousch (1995), A new model for Mars atmospheric dust based upon analysis of ultraviolet through infrared observations from Mariner 9, Viking, and Phobos, *Journal of Geophysical Research*, 100(E3), 5251–5263.

Clancy, R. T., M. J. Wolff, and P. R. Christensen (2003), Mars aerosol studies with the MGS TES emission phase function observations: Optical depths, particle sizes, and ice cloud types versus latitude and solar longitude, *Journal of Geophysical Research*, 108(E9), 5098, doi:10.1029/2003JE002058.

Conrath, B. J., J. C. Pearl, M. D. Smith, W. C. Maguire, P. R. Christensen, S. Dason, and M. S. Kaelberer (2000), Mars Global Surveyor Thermal Emission Spectrometer (TES) observations: Atmospheric temperatures during aerobraking and science phasing, *Journal of Geophysical Research*, 105(E4), 9509–9519.

Cull, S.C., R. Arvidson, M. Mellon, RV Morris, M. Wolff, M Lemmon (2010) The seasonal ice cycle at the Mars Phoenix Landing site: II. Post-landing CRISM and ground observations. *Journal of Geophysical Research*, 115, E00E19, doi:10.1029/2009JE003410.

Domingue, D., B. Hartman, A. Verbiscer (1997) The scattering properties of natural terrestrial snows versus icy satellite surfaces. *Icarus* 128(1), 28-48, doi:10.1006/icar.1997.5733.

Eluszkiewicz, J. (1993) On the microphysical state of the Martian polar caps. *Icarus* 103(1), 43-48, doi:10.1006/icar.1993.1056.

Eluszkiewicz, J., J-L. Moncet, T.N. Titus, G.B. Hansen (2005) A microphysically-based approach to modeling emissivity and albedo of the martian seasonal caps. *Icarus* 174(2), 524-534, doi:10.1016/j.icarus.2004.05.025.

Forget, F., G. B. Hansen, and J. B. Pollack (1995), Low brightness temperatures of Martian polar caps: CO_2 clouds or low surface emissivity?, *Journal of Geophysical Research*, 100(E10), 21,219–21,234.

Forget, F., F. Hourdin, O. Talagrand (1998) CO_2 snowfall on Mars: Simulation with a general circulation model. *Icarus* 131(2), 302-316, doi:10.1006/icar.1997.5874.

Haberle, R.M., Forget, Francois, Colaprete, Anthony; Schaeffer, James; Boynton, William V.; Kelly, Nora J.; Chamberlain, Matthew A. (2008) The effect of ground ice on the Martian seasonal CO_2 cycle. *Planetary and Space Science* 56: 251-255.

Hansen, G.B. (1997) The infrared absorption spectrum of carbon dioxide ice from 1.8 to 333 μm. *Journal of Geophysical Research*, 102: 21569-21587, DOI: 10.1029/97JE01875.

Hansen, G.B. (2005) Ultraviolet to near-infrared absorption spectrum of carbon dioxide ice from 0.174 to 1.8 μm. *Journal of Geophysical Research* 110: E11003, doi: 10.1029/2005JE002531.

Hapke, B. (1981), Bidirectional Reflectance Spectroscopy 1. Theory, *Journal of Geophysical Research*, 86(B4), 3039–3054.

Hapke, B. (1984) Bidirectional reflectance spectroscopy. 3. Correction for Macroscopic Roughness. *Icarus* 59: 41-59.

Hapke, B. (1993) Theory of reflectance and emittance spectroscopy. Cambridge University Press: Cambridge, UK.

Heet, T,. R. E. Arvidson, S. C. Cull, M. T. Mellon, and K. D. Seelos (2009) Geomorphic and geologic settings of the Phoenix lander mission landing site. *Journal of Geophysical Research*, 114, E00E04, doi:10.1029/2009JE003416, 2009.

Henyey, L.G. and J.L. Greenstein (1941) Diffuse radiation in the galaxy, *Astrophysical Journal* 93:70-83, 1941.

Houben, H., R. M. Haberle, R. E. Young and A. P. Zent (1997) Evolution of the Martian water cycle. *Advances in Space Research* 19(8): 1233-1236. doi:10.1016/S0273-1177(97)00274-3

James, P.B., H. H. Kieffer, and D. A. Paige (1993) The seasonal cycle of carbon dioxide on Mars, in Mars (Hugh Kieffer, editor), University of Arizona Press: Tucson, Arizona.

James, P.B. and B.A. Cantor (2001) Martian north polar cap recession: 2000 Mars Orbiter Camera observations. *Icarus* 154: 131-144. doi:10.1006/icar.2001.6653

Johnson, J., R. Kirk, L. Soderblom, L. Gaddis, R. Reid, D. Britt, P. Smith, M. Lemmon, N. Thomas, J. Bell, N. Bridges, R. Anderson, K. Herkenhoff, J. Maki, S. Murchie, A. Dummel, R. Jaumann, F. Trauthan, F. Arnold (1999), Preliminary results on photometric properties of materials at the

Sagan Memorial Station, Mars, *Journal of Geophysical Research*, 104(E4), 8809-8830.

Johnson, J.R., W. Grundy, M. Lemmon, J. Bell, M. Johnson, R. Deen, R. Arvidson, W. Farrand, E. Guinness, A. Hayes, K. Herkenhoff, F. Seelos, J. Soderblom, S. Squyers (2006) Spectrophometric properties of materials observed by Pancam on the Mars Exploration Rovers: 1. Spirit. *Journal of Geophysical Research*, 111, E02S14, doi:10.1029/2005JE002494.

Jouglet, D., Francois Poulet, Ralph E. Milliken, John F. Mustard, J.-P. Bibring,Yves Langevin, B.Gondet, and C. Gomez (2007), Hydration state of the Martian surface as seen by Mars Express OMEGA: 1. Analysis of the 3 μm hydration feature, *Journal of Geophysical Research*, 112, E08S06, doi:10.1029/2006JE002846.

Kelly, N. J., W. V. Boynton, K. Kerry, D. Hamara, D. Janes, R. C. Reedy, K. J. Kim, and R. M. Haberle (2006), Seasonal polar carbon dioxide frost on Mars: CO_2 mass and columnar thickness distribution, *Journal of Geophysical Research*, 111, E03S07, doi:10.1029/2006JE002678.

Kieffer, H. H., T. N. Titus, K. F. Mullins, and P. R. Christensen (2000), Mars south polar spring and summer behavior observed by TES: Seasonal cap evolution controlled by frost grain size, *Journal of Geophysical Research*, 105(E4), 9653–9699. doi:10.1029/1999JE001136

Kieffer, H.H. and T.N. Titus (2001) TES mapping of Mars' northern seasonal cap. *Icarus* 154: 162-180. doi:10.1006/icar.2001.6670

Kieffer, H.H. (2007) Cold jets in the Martian polar caps. *Journal of Geophysical Research*, 112(E11), 8005. DOI: 10.1029/2006JE002816

Kirk, R. L., E. Howington-Kraus, M. Rosiek, B. Archinal, K. Becker, D. Cook, D. Galuszka, P. Geissler, T. Hare, I. Holmberg, L. Keszthelyi, B. Redding, W. Delamere, D. Gallagher, J. Chapel, E. Eliason, R. King, A. McEwen (2008), Ultrahigh resolution topographic mapping of Mars with MRO HiRISE stereo images: Meter-scale slopes of candidate Phoenix landing sites, *Journal of Geophysical Research*, 113, E00A24, doi:10.1029/2007JE003000.

Kossacki, K.J. and W.J. Markiewicz (2002) Martian seasonal CO_2 ice in polygonal troughs in southern polar region: Role of the distribution of subsurface H_2O ice. *Icarus* 160: 73-85. doi:10.1016/S0032-0633(03)00070-9

Kossacki, K.J., Wojciech J. Markiewicz , M. Smith (2003) Surface temperature of Martian regolith with polygonal features: influence of the subsurface water ice. *Planetary and Space Science* 51: 569-580.

Larson, H.P. and U. Fink (1972) Identification of carbon dioxide frost on the Martian polar caps. *The Astrophysical Journal* 171: L91-L95.

Litvak, M.L., I. Mitrofanov, A. Kozyrev, A. Sanin, V. Tretyakov, W. Boynton, D. Hamara, C. Shinohara, R. Saunders (2005) Modeling of Martian seasonal caps from HEND/ODYSSEY data. *Advances in Space Research* 36: 2156-2161. doi:10.1016/j.asr.2005.09.007

McEwen, A. S., E. Eliason, J. Bergstrom, N. Bridges, C. Hansen, W. Delamere, J. Grant, V. Gulick, K. Herkenhoff, L. Keszthelyi, R. Kirk, M. Mellon, S. Squyers, N. Thomas, C. Weitz (2007), Mars Reconnaissance Orbiter's High Resolution Imaging Science Experiment (HiRISE), *Journal of Geophysical Research*, 112, E05S02, doi:10.1029/2005JE002605.

Mellon, M. T., W. V. Boynton, W. C. Feldman, R. E. Arvidson, T. N. Titus, J. L. Bandfield, N. E. Putzig, and H. G. Sizemore (2008a), A prelanding assessment of the ice table depth and ground ice characteristics in Martian permafrost at the Phoenix landing site, *Journal of Geophysical Research*, 113, E00A25, doi:10.1029/2007JE003067.

Mellon, M. T., R. E. Arvidson, J. J. Marlow, R. J. Phillips, and E. Asphaug (2008b), Periglacial landforms at the Phoenix landing site and the northern plains of Mars, *Journal of Geophysical Research*, 113, E00A23, doi:10.1029/2007JE003039.

Milliken, R. E., J. F. Mustard, F. Poulet, D. Jouglet, J.-P. Bibring, B. Gondet, and Y. Langevin (2007), Hydration state of the Martian surface as seen by Mars Express OMEGA: 2. H_2O content of the surface, *Journal of Geophysical Research*, 112, E08S07, doi:10.1029/2006JE002853.

Murchie, S., et al., (2007), Compact Reconnaissance Imaging Spectrometer for Mars (CRISM) on Mars Reconnaissance Orbiter (MRO), *Journal of Geophysical Research*, 112, E05S03, doi:10.1029/2006JE002682.

Pike, W.T., H. Sykulska, S. Vigendran, and the Phoenix Microscopy Team (2009) Fractal analysis of the microstructure of the martian soil at the Phoenix landing site. LPSC XL, Abstract #1909.

Roush, T.L. (1994) Charon: More than water ice? *Icarus* 108: 243-254. doi:10.1006/icar.1994.1059

Seelos, K. D., R. Arvidson, S. Cull, C. Hash, T. Heet, E. Guinness, P. McGuire, R. Morris, S. Murchie, T. Parker, T. Roush, F. Seelos, M. Wolff (2008), Geomorphologic and mineralogic characterization of the northern plains of Mars at the Phoenix Mission candidate landing sites, *Journal of Geophysical Research*, 113, E00A13, doi:10.1029/2008JE003088.

Sizemore, H. G. and M. T. Mellon (2006) Effects of soil heterogeneity on martian ground-ice stability and orbital estimates of ice table depth, *Icarus* 185, 358-369. doi:10.1016/j.icarus.2006.07.018

Smith, D.E., M. Zuber, G. Neumann (2001) Seasonal variations of snow depth on Mars. *Science* 294: 2141-2146. DOI: 10.1126/science.1066556

Smith, M.D. (2002) The Annual Cycle of Water Vapor on Mars as Observed by the Thermal Emission Spectrometer. *Journal of Geophysical Research* 107, doi:10.1029/2001JE001522.

Smith, M. D. (2002), The annual cycle of water vapor on Mars as observed by the Thermal Emission Spectrometer, *Journal of Geophysical Research*, 107(E11), 5115, doi:10.1029/2001JE001522.

Smith, M.D. (2004) Interannual variability in TES atmospheric observations of Mars during 1999–2003. *Icarus* 167: 148-165. doi:10.1016/j.icarus.2003.09.010

Smith, P. H., L. Tamppari, R. Arvidson, D. Bass, D. Blaney, W. Boynton, A. Carswell, D. Catling, B. Clark, T. Duck, E. DeJong, D. Fisher, W. Goetz, P. Gunnlaugsson, M. Hecht, V. Hipkin, J. Hoffman, S. Hviid, H. Keller, S. Kounaves, C.F. Lange, M. Lemmon, M. Madsen, M. Malin, M. Markieqicz, J. Marshall, C. McKay, M. Mellon, D. Michaelangeli, D. Ming, R. Morris, N. Renno, W. Pike, U. Staufer, C. Stoker, P. Taylor, J. Whiteway, S. Young, A. Zent (2008) Introduction to special section on the Phoenix Mission: Landing Site Characterization Experiments, Mission Overviews, and Expected Science, *Journal of Geophysical Research*, 113, E00A18, doi:10.1029/2008JE003083.

Smith, P.H., L. K. Tamppari, R. E. Arvidson, D. Bass, D. Blaney, W. V. Boynton, A. Carswell, D. C. Catling, B. C. Clark, T. Duck, E. DeJong, D. Fisher, W. Goetz, H. P. Gunnlaugsson, M. H. Hecht, V. Hipkin, J. Hoffman, S. F. Hviid, H. U. Keller, S. P. Kounaves, C. F. Lange, M. T. Lemmon, M. B. Madsen, W. J. Markiewicz, J. Marshall, C. P. McKay, M. T. Mellon, D. W. Ming, R. V. Morris, W. T. Pike, N. Renno, U.

Staufer, C. Stoker, P. Taylor, J. A. Whiteway, A. P. Zent (2009) Water at the Phoenix Landing Site. *Science* 325: doi:10.1126/science.1172339.

Stamnes, K., S.-Chee., Tsay, K. Jayaweera, and W. Wiscombe (1988) Numerically stable algorithm for discrete-ordinate-method radiative transfer in multiple-scattering and emitting layered media. *Applied Optic*s 27: 2502-2509. DOI: 10.1364/AO.27.002502

Titus, T. N., H. H. Kieffer, K. F. Mullins, and P. R. Christensen (2001), TES premapping data: Slab ice and snow flurries in the Martian north polar night, *Journal of Geophysical Research*, 106(E10), 23,181–23,196. doi:10.1029/2000JE001284

Wagstaff, K.L., T. Titus, A. Ivanov, R. Castano, J. Bandfield (2008) Observations of the north polar water ice annulus on Mars using THEMIS. *Planetary and Space Sciences,* doi:10.1016/j.pss.2007.08.008

Warren, S.G. (1984) Optical constants of ice from the ultraviolet to the microwave. *Applied Optics* 23: 1206-1225.

Wiseman, S., Arvidson, R. E.; Griffes, J. L.; Murchie, S.; Poulet, F.; Crism Science Team (2007) Initial analysis of CRISM data over Meridiani Planum. LPSC XXXVIII: Abstract #1945.

Wiseman, S. (2009) Retrieval of atmospherically-corrected hyperspectral CRISM surface reflectance spectra using DISORT radiative transfer modeling:

Comparison to the emipirical ‘volcano scan’ correction method. *Journal of Geophysical Research*, submitted.

Wolff, M. J., and R. T. Clancy (2003), Constraints on the size of Martian aerosols from Thermal Emission Spectrometer observations, *Journal of Geophysical Research*, 108(E9), 5097, doi:10.1029/2003JE002057.

Wolff, M. J.; Clancy, R. T.; Smith, M. D.; Crism Science Team; Marci Science Team (2007) Some studies of Martian aerosol properties using MRO/CRISM and MRO/Marci, *Seventh International Conference on Mars:* 3121.

Wolff, M. J., M. D. Smith, R. T. Clancy, R. Arvidson, M. Kahre, F. Seelos IV, S. Murchie, and H. Savijärvi (2009), Wavelength dependence of dust aerosol single scattering albedo as observed by the Compact Reconnaissance Imaging Spectrometer, *Journal of Geophysical Research*, 114, E00D04, doi:10.1029/2009JE003350.

Chapter 3 - The seasonal ice cycle at the Mars Phoenix landing site: II. Post-landing CRISM and ground observations

Journal of Geophysical Research, 115, E00E19, doi:10.1029/2009JE003410.

3.1 Introduction

The Mars Phoenix lander touched down on 25 May 2008 at 68.22˚N, 234.25˚E (planetocentric; *Arvidson et al.*, 2009), and operated on the surface from solar longitude (L_s)~77° (late spring) to L_s~149° (mid summer), when a combination of decreased solar radiation and a dust storm resulted in a mission-ending lack of power. One objective of the Phoenix mission was to characterize the northern high-latitude environment during the summer season, including the water ice and dust cycles [*Smith et al.,* 2008]. A complete understanding of the water cycle and environment is necessary for understanding mechanisms that relate to habitability, for example the migration of thin films of water and the exchange of water between the atmosphere and ice table. The water ice cycle has particular interest for Phoenix because the landing site is covered for much of the year by the seasonal ice cap: a layer of CO_2 and H_2O ices that extends from the north pole to ~50°N [*James et al.,* 1993; *Cull et al., 2010a*]. Phoenix observations of the onset of the seasonal ice cap, when combined with orbital observations, provide a detailed view of the seasonal ice cycle at the northern high latitudes of Mars.

Previous studies have described the onset of the seasonal ice cap on a regional scale and have shown that cap development is spatially variable. *Kieffer and Titus* [2001] observed that by L_s~162° the atmosphere is cold enough for water ice clouds to form north of ~64°N. They also noted that daytime surface temperatures north of ~68°N become cold enough for water frost to form between L_s~164° and 184°. Based on Viking orbiter data, *Bass and Paige* [2000] estimated that water ice should be stable on the surface in the Phoenix latitude band as early as L_s~155°. Given the considerable disagreement about the timing of ice appearance in this latitude band, it is difficult to pinpoint when water ice first appears at the Phoenix landing site using past data sets.

Cull et al., [2010a] used data from the Compact Reconnaissance Imaging Spectrometer for Mars (CRISM) onboard Mars Reconnaissance Orbiter (MRO) and High-Resolution Imaging Science Experiment (HiRISE) to map seasonal ices from late summer to early spring, prior to Phoenix landing. In this paper, we examine the seasonal and diurnal ice cycles during and immediately after Phoenix operations, from late spring to late summer. High-resolution images and spectra from CRISM are used to identify water ice, and a non-linear mixing model is used to estimate ice grain sizes and relative abundances. CRISM spectra at various viewing geometries are used to constrain surface scattering and physical properties. Finally, CRISM findings are compared to Phoenix ground measurements from the Surface Stereo Imager (SSI, *Smith et al.*, 2008), LIDAR [*Whiteway et al.*, 2009], and Optical Microscope (OM, *Hecht et al.*, 2008).

3.2 Data Set and Methods

CRISM is a hyperspectral imaging spectrometer that covers 544 wavelengths between 0.364 and 3.936 μm at a spatial resolution of ~18 m/pixel in Full-Resolution Targeted (FRT) mode [*Murchie et al.*, 2007]. The detector is attached to a gimbal platform, which allows CRISM to acquire Emission Phase Functions (EPFs): multiple images of the same area taken from different angles as the spacecraft approaches, flies over, and moves away from the target. EPF sequences illustrate the effects of the atmosphere as well as scattering properties of the surface and aerosols.

This study uses 25 CRISM FRT images taken directly over the landing site (on the ejecta deposit of the 10-km diameter Heimdal Crater) and 13 FRTs taken near the landing site, covering, for example, portions of Heimdal [*Arivdson et al.*, 2009]. Most of the FRTs were taken either directly over the landing site or over Heimdal Crater, covering the area from 68.117°N to 68.364°N and from 230.379°E to 235.701°E. The FRTs were taken at either 3 p.m. or 3 a.m. Local True Solar Time (LTST) (Figure 3.1). These data were acquired as part of a coordinated MRO-Phoenix observation campaign to map atmospheric and surface dynamics [*Tamppari* *et al.,* 2009]. FRT data utilized in this study were processed to units of *I/F* (radiance at the sensor divided by solar irradiance divided by pi). This study also uses ground observations from the Surface Stereo Imager (SSI) [*Smith et al.,* 2008], a stereo camera with 24 filters covering the spectral range of 0.445 to 1.001 μm.

3.2.1 Atmospheric Removal

To remove atmospheric effects – gas and aerosol absorption and scattering – CRISM spectra were modeled with a Discrete Ordinate Radiative Transfer (DISORT) model [*Stamnes et al.*, 1988; *Wolff et al.*, 2007], which has been adapted for planetary applications ("DISORT_multi"; *Arvidson et al.*, 2005, 2006) and specifically for use with CRISM images [*Wiseman et al.,* 2009].

DISORT calculates the *I/F* that CRISM would measure if looking through the atmosphere at a surface with known scattering properties. The atmosphere is treated as parallel layers of CO, CO_2, and H_2O gas, each with a specific pressure and temperature, and evenly-distributed dust aerosols (ice aerosols are assumed to be well-mixed above the point of water condensation) [*Wiseman et al.*, 2009]. The atmosphere over the Phoenix landing site at a given solar longitude is estimated from historical data from the Thermal Emission Spectrometer (TES): water column abundances are from *Smith* [2002], ice aerosols are estimated from TES optical depths at 12.1 μm [*Smith* 2004], dust aerosols are estimated from CRISM EPF analysis at 0.9 μm [*Tamppari et al.,* 2009], surface pressure estimated from Viking 2 lander results, and the atmospheric pressure profile calculated by integrating the hydrostatic equilibrium equation [*Conrath et al.*, 2000]. Dust aerosols are assumed to have a radius of 1.5 μm, a reasonable assumption given that the average non-dust storm dust aerosol is estimated to be between 1.2 and 1.8 μm [*Wolff et al.*, 2009]. Dust aerosol indicies of refraction and a wavelength-dependent phase function were derived from CRISM observations [*Wolff et al.*, 2009]. Water ice aerosols are assumed to have scattering properties from *Clancy et al.*, [2003] and a radius of 2.0 μm, the median particle size observed by TES for ice aerosols in clouds [*Clancy et al.*, 2003].

For DISORT calculations, the surface is assumed to scatter light according to a nonlinear mixing model based on [*Hapke* 1981, 1993]:

$$r(i,e,g) = \frac{w}{4\pi}\frac{\mu_0}{\mu_0+\mu}\{[1+B(g)]p(g)+H(\mu_0)H(\mu)-1\}$$

Equation 3.1

where i, e, and g are the incidence, emergence, and phase angles, respectively; $r(i,e,g,)$ is the bidirectional reflectance observed, μ_0 is the cosine of the incidence angle, μ is the cosine of the emergence angle, w is the single-scattering albedo, $B(g)$ is the opposition effect, $p(g)$ is the single-particle phase function, and $H(\mu_0)$ $H(\mu)$ describe multiple scattering. The opposition effect is ignored in this paper, because all of our observations were taken at phase angles >40˚.

The single-particle phase function is modeled with a two-lobed Henyey-Greenstein model [*Henyey and Greenstein* 1941]:

$$p(g) = \frac{(1-\delta^2)(1-f)}{[1-2\delta\cos(g)+\delta^2]^{3/2}} + \frac{f(1-\delta^2)}{[1+2\delta\cos(g)+\delta^2]^{3/2}}$$

Equation 3.2

where *f* is a weighting factor that describes the scattering direction (*f*=0 for forward scatter, *f*=1 for backscatter), and δ is an asymmetry factor constrained to be between -1 and 1 (δ=0 for isotropic scatter). The selection of *B(g)*, δ, and *f* parameters is discussed in section 2.4.

CRISM center wavelengths shift slightly (<~1 nm) with instrument temperature changes [*Murchie et al.*, 2007]. To account for this, DISORT was run with 0.1 nm spacing over the CO_2 gas bands, and the wavelengths resampled and fit to the observed wavelengths to determine the offsets [*Wiseman* 2007]. The wavelength displacement is typically 0.3 to 0.7 nm for each wavelength.

For each FRT, DISORT was run for surfaces with various *w* values: 0.25, 0.5, 0.7, 0.8, 0.9, and 0.99. The relationship between *w* and *I/F* for each band was modeled as a 5th-order polynomial, and a look-up table was generated to relate observed *I/F* to *w*. Equation 3.1 and Equation 3.2 were then used to convert *w* to bidirectional reflectance. Atmospheric parameters were adjusted slightly to remove residual gas bands (or overcorrected gas bands), if needed (Figure 3.2). Typically, this adjustment consisted of small changes in ice or dust aerosols (tau ± 0.05) and was necessary for only a few FRTs considered in this study.

3.2.2 Modeling of Surface Spectra

This study addresses two surface components: water ice and soil. Ice-free surfaces at the Phoenix landing site have relatively featureless spectra between 1.0 and 2.7 μm, but are highly absorbing at wavelengths <1.0 μm (Figure 3.3a). Water ice, on the other hand, is translucent at short wavelengths, but has strong absorptions at 1.5 and 2.0 μm and dramatically changes the shape of the spectrum between 2.3 and 2.6 μm due to a strong 3.17 μm absorption (Figure 3.3a). For mixtures or layers of water and ice, light interacts with both components before reaching the detector, so the shape and albedo of the final spectrum is a non-linear mixture of the two components (Figure 3.3b).

CRISM bidirectional surface reflectance spectra were extracted from the Heimdal Outer Ejecta unit (Lowland Bright unit of *Seelos et al.,* [2008]) on which Phoenix landed [*Heet et al.,* 2009] and is widespread around the Phoenix landing site. Five-by-five pixel average spectra were compared across the unit in each scene and a representative spectrum selected for modeling. For observations taken over the landing site, spectra were selected from near the landing site itself. Spectra were extracted only from central areas of each image to avoid effects of spectral smile [*Murchie et al.,* 2007].

To extract grain sizes and relative abundances from CRISM observations, each spectrum was simulated using the non-linear mixing model based on Equation 3.1 and Equation 3.2 [*Hapke* 1981], and a two-layer model described in equations 9.31a-e in *Hapke* [1993]. Single-scattering albedos of component mixtures were calculated as:

$$w = \frac{\sum_{i=1}^{i=n}\left(Q_{Si} M_i / \rho_i D_i\right)}{\sum_{i=1}^{i=n}\left(Q_{Ei} M_i / \rho_i D_i\right)}$$

Equation 3.3

where M_i is the mass fraction of component *i*, ρ_i its solid density, D_i its diameter, Q_{Si} the scattering efficiency, Q_{Ei} the extinction efficiency, and the summation is carried out for all components in the *n*-component mixture. Scattering efficiency was calculated as described by *Roush* [1994], and extinction efficiency was set to 1, because the particles being considered are large compared to the wavelength and so are affecting the entire wavefront [*Hapke* 1981].

As described above, this model depends on viewing geometry, grain complex indicies of refractions, sizes, solid densities, relative mass fractions of each component; and the surface porosity and scattering parameters: δ and *f*. Water ice optical constants were used from *Warren* [1984]. Soil optical constants were from *Clancy et al.,* [1995], which are derived from Mauna Kea palagonite, a low-temperature alteration product of fine-grained basaltic ash. The Mauna Kea palagonite appears to be a good analog for the Phoenix site soils [*Hecht et al.,* 2008], although it has a slightly shallower slope between 0.7 and 1.0 μm. A solid density of ρ=0.9167 g/cm^3 was used for water ice, and ρ=2.700 g/cm^3 for soil. We assume a surface porosity of 50%, similar to the Viking 2 landing site [*Moore et al.,* 1979], because Phoenix soil physical properties appear similar to the Viking 2 landing site in general [*Arvidson et al.,* 2009]. The 50% porosity is also supported by modeling of Phoenix soil thermal inertia based on data from the Thermal and Electrical Conductivity Probe [TECP; *Zent,* personal communication]. For ice layers, we assume a porosity of 70%, similar to a typical winter snowpack on Earth; however, we find that, for very thin layers (<1 mm), top-layer porosity does not affect results for porosities between ~40 and ~80%. For each CRISM spectrum, we use the same scattering parameters used in DISORT modeling of that spectrum. Scattering parameter constraints are described in Section 2.4.

In the layered models, the thickness of the overlying layer was calculated based on the cross-sectional mass (e.g., mg/cm^2). To convert this to a layer thickness, the cross-sectional mass was divided by the material’s solid density.

With these assumptions, the grain sizes and relative mass fractions of the two components were varied to match each CRISM spectrum.

3.2.3 Sensitivity Analysis

Because Hapke modeling can produce non-unique results (for example, trading grain size for mass fraction can produce similar spectra), a sensitivity analysis was used to test the uniqueness of each result. First, a set of best-fit parameters was found by inspection and a chi-squared (X^2) value calculated:

$$X^2 = \sum_{\lambda=1}^{n} \frac{(r_0 - r_m)^2}{r_0^2}$$

Equation 3.4

where r_o is the observed bidirectional reflectance, r_m is the modeled bidirectional reflectance, and the summation is carried out over all wavelengths (except between 1.95 μm and 2.1 μm, an area sometimes disrupted by residual CO_2 gas bands in DISORT-derived spectra).

This initial set of parameters represented a local minimum in X^2 space. To test for other local minima, one parameter (grain size, mass ratio, or upper layer thickness) was stepped away from the initial value while the other parameters were allowed to vary and new X^2 values calculated. In this way, for each spectrum, one to three local minima were identified. Some of these could be discarded as actual best-fit solutions either because their absorption band depths did not match the band depths of the CRISM spectrum, or because they were physically unreasonable (for example, 30 μm grains in a layer of material only 15 μm thick). After discarding unreasonable local minima, if the FRT still had more than one local minimum, then the FRT was discarded as being too poorly constrained.

Once a single best-fit local minimum was found, we tested how well-constrained were each of the variables within that solution by systematically varying one parameter and re-calculating X^2 values. If the parameter was well-constrained, the X^2 value should increase quickly as it is varied (e.g., Figure 3.8C). If the parameter is poorly constrained, it should increase slowly away from the best fit value (e.g., Figure 3.8B).

3.2.4 Constraining Surface Scattering Parameters

DISORT-based single-scattering albedo retrievals and non-linear mixing model results are sensitive to the surface phase function parameters (δ and f), and the magnitude (B_0) and width (h) of the opposition effect (the latter two are ignored, as discussed above). Deriving these parameters for the Phoenix landing site is beyond the scope of this paper; however, the parameters selected must approximate the behavior of the Phoenix surface for the DISORT and Hapke modeling to be effective.

Johnson et al., [2006] used Spirit Rover data to derive scattering parameters for various materials at Gusev Crater. To approximate the Phoenix landing site, DISORT was used to model surfaces with Gusev scattering parameters over a range of viewing geometries. The resulting relationships between radiance and viewing geometry were compared to the CRISM EPFs, and the closest-fitting set of scattering parameters selected. Spectra for the EPF sequences were selected by averaging the central 20 pixels of each line within the EPF.

3.2.5 Separating Ice Aerosols from Surface Ice

Water ice produces major absorptions at 1.52, 1.94, 2.02, 2.96, and 3.17 μm [*Gaffey et al.*, 1997], regardless of whether it is on the surface or in the atmosphere. Although the DISORT modeling removes contributions from ice aerosols, the initial inputs are based on historical ice optical depths, which vary slightly from year to year (Figure 3.4). An incomplete removal of ice aerosol signatures could result in a positive identification for surface ice, when in fact the ice bands are due to ice aerosols.

To assess whether water ice bands are due to surface ice, ice aerosols, or a combination of the two, the relative band depths of the 1.5 μm and 3.17 μm bands were compared for each scene. Band depths were calculated as defined by *Pelkey et al.*, [2007]:

$$BD = 1 - \frac{\mathrm{R}(\lambda\mathrm{C})}{\mathrm{a} * \mathrm{R}(\lambda S) + \mathrm{b} * \mathrm{R}(\lambda\mathrm{L})}$$

Equation 3.5

where R(λ) is the reflectance measured at wavelength λ, λ_C is the center wavelength for the band depth being measured, the continuum is defined between wavelengths λ_S

and λ_L, $b=(\lambda_C-\lambda_S)/(\lambda_L-\lambda_S)$, and $a=1-b$. For the 1.5 μm band depth, $\lambda_C=1.510$ μm, $\lambda_S=1.330$ μm, and $\lambda_L=1.695$ μm. For the 3.17 μm band depth, $\lambda_C=3.170$ μm, $\lambda_S=2.22$ μm, $\lambda_L=3.72$ μm.

The 3.17 μm band is more sensitive to the presence of water ice than the 1.5 μm band, as noted in OMEGA data by *Langevin et al.,* [2007]. This is because the 3.17 μm feature is due to the fundamental ν_1 vibration and is approximately an order of magnitude stronger than the 1.5 μm, which is due to the $2\nu_3$ overtone. The 3.17 μm band appears for very small water ice grain sizes or abundances, and, with increasing grain size, saturates quickly. The 1.5 μm band appears for larger grain sizes and abundances and deepens more slowly with increasing grain size. The ratio between the 3.17 μm band depth and the 1.5 μm band depth, then, is high for small grain sizes or abundances, and smaller for large grain sizes or abundances.

To illustrate the relationship between surface ice grain size and the 3.17- to 1.5-μm band depth ratio, bidirectional reflectances were calculated for icy surfaces with varying ice grain sizes, using the model described in Section 2.2. To illustrate the relationship between atmospheric ice and the 3.17- to 1.5-μm band depth ratio, DISORT models were run with varying ice optical depths (0.0, 0.01, 0.02, 0.04, 0.05, 0.06, 0.07, 0.08, 0.09, 0.1, 0.15). Results from these runs are presented in Section 3.2 below.

To distinguish between surface and atmospheric ice in the CRISM observations, the 1.5-μm and 3.17-μm band depths were calculated for the atmospherically-uncorrected observations. For each, the 3.17/1.5-μm band depth ratio was compared to those for surface and atmospheric ices. Results from these analyses are presented in Section 3.2 below.

3.3 Results

3.3.1 Constraining Scattering Parameters

An example of an ice-free CRISM EPF sequence over Phoenix is shown in Figure 3.5 for FRT0000B1D2 at 1.08 μm. The EPFs are poorly approximated by a Lambertian surface, which produces a scattered radiance that is independent of emergence or phase angles. They are also poorly approximated by scattering properties similar to the Gray Rock or Red Rock endmembers described by *Johnson et al.,* [2006]. The Phoenix EPFs are closer to the Soil endmembers derived by *Johnson et al.,* [2006] for the Spirit landing site at Gusev Crater: an asymmetry parameter of 0.498, forward-scattering fraction of 0.817, B_0 of 1, and h of 0.385. The Gusev Crater Soil endmember is a wide-spread plains unit that is photometrically to similar to many Martian soils, including dusty surfaces at the Viking 1 landing site [*Arvidson et al.*, 1989] and soils at the Mars Pathfinder landing site [*Johnson et al.,* 1999].

3.3.2 Atmospheric vs. Surface Ice

The 3.17- to 1.5- μm band depth ratio described in Section 2.5 were used to distinguish between atmospheric and surface ices. For surface ice (Figure 3.6), the ratio decreases with increasing grain sizes; however, the ratio is always relatively small: in the 1 to 8 range. Ice aerosols (Figure 3.7) follow a similar pattern: higher 3.17/1.5 ratio for lower ice optical depths. For example, an ice optical depth of 0.05 produced a 3.17/1.5 ratio of 234, while an optical depth of 0.1 produced a ratio of 109. Although the ratio becomes smaller for high ice optical depths, it is always much higher than for surface ice: between 100 and 500. The 3.17/1.5 ratio is so much lower for surface ices because, due to their higher concentration and larger grain sizes, the 3.17 μm band is saturated; the more surface ice, the deeper the 1.5 μm band, and the lower the 3.17/1.5 ratio. Ice aerosols, on the other hand, are not densely packed enough to saturate the 3.17 μm band and have only a minor impact on the 1.5 μm band.

The 3.17/1.5 ratio, then, can be used to distinguish between ice signatures due to surface ice, atmospheric ice, or a combination of the two. High 3.17/1.5 ratios (>50) are taken to indicate that most of the ice band contributions are from ice aerosols. Low 3.17/1.5 ratios (<10) are taken to indicate mostly surface contributions. Intermediate 3.17/1.5 ratios (10-50) are taken to indicate a combination of surface and atmospheric ice contributions.

Water molecules adsorbed onto the surface also produce an absorption at 3.05 μm, which, when strong enough, could affect the spectrum at 3.17 μm. Adsorbed water does not produce a 1.5 μm absorption (its $2\nu_3$ overtone appears at 1.45 μm) [*Gaffey et al.,* 1997], so its presence could affect the 3.17/1.5- μm ratios. However, because the 3.17 μm band is already saturated in all of the icy FRTs considered here, adsorbed water does not influence the 3.17/1.5- μm ratio.

To test the validity of the 3.17/1.5- μm ratio method for distinguishing ice aerosols from surface ice, we performed the same analysis on three CRISM cubes: an early spring (L_s~34°) observation known to have significant amounts of surface ice [*Cull et al., 2010*], a mid-spring (L_s~42°) observation with small amounts of surface ice, and a late spring (L_s~68°) observation with no surface ice at all. These observations have comparable ice aerosol optical depths (~0.03 from historical TES data). The early spring observation was found to have a 3.17/1.5- μm ratio of 2.9, mid-spring a ratio of 13.25, and late spring a ratio of 255.0.

3.3.3 Late spring to Early summer

3.3.3-a Ice-Free Spectrum

The last of the seasonal cap water ice disappears from the Phoenix landing site by L_s~59° [*Cull et al., 2010*]. Between L_s ~59° and L_s~104°, 13 FRTs were acquired; these show an ice-free surface. Hapke modeling of three observations produced a best fit using two layers of soil: a fine-grained (15 μm) thin layer (~100 μm thick) on top of a layer of sand-sized (2 mm) soil particles (analysis of FRT0000B1D2 is shown in Figure 3.8a). A sensitivity analysis conducted on these models shows that the size of the sand-sized particles is poorly constrained on the upper end (Figure 3.8b); however, the dust grain size is constrained to be between ~10 and 30 μm, with a clear minimum at 15 μm. This combination was seen consistently for ice-free observations over multiple L_s and multiple observations, including ice-free observations reported in *Cull et al., [2010]*.

3.3.3-b Permanent and Mobile summer Ices

Although the surface in general is ice-free during the late spring and early summer, several patches of permanent ice were observed. *Seelos et al.,* [2008] reported permanent patches of summertime ices on the north-facing wall of Heimdal Crater (Figure 3.9) and the northern slopes of ejecta deposits to the northeast of Heimdal (Figure 3.10), similar to the permanent patches of water ice observed on the walls of Louth Crater by *Brown et al.,* [2008]. These ices were monitored throughout the summer as part of the CRISM-Phoenix coordinated observation campaign.

The water ice patches - both of the north-facing wall of Heimdal and on the north-facing slopes of the mountains to the northeast – do not appear to grow or shrink during the summer (Figure 3.9 and Figure 3.10). However, for both ice patches, the overall albedo darkens from early to late summer (L_s~94° to ~160°), and the water ice band depths deepen from ~3% at L_s~119° to ~6% at L_s~160° (Figure 3.9 and Figure 3.10), implying that the water ice is becoming coarser grained. It is possible that fine-grained water ice is cold-trapped onto the ice patches during the spring defrost period, when water ice is sublimating from the surrounding terrain and filling the atmosphere with water vapor. The fine-grained surface ice could then either sinter into coarser grains – a relatively common and rapid processes for polar ices [*Eluszkiewicz* 1993] – or sublimate as atmospheric temperatures continue to rise during mid- and late summer, exposing the coarser-grained permanent ice.

In addition to the patches of permanent ice, mobile patches of summertime ices were observed. At 3 p.m. at L_s~86°, water ice was observed on the shadowed wall of an ~85-meter crater located ~6.5 km northeast the landing site (68.29°N, 234.46°W; Figure 3.11). A 3 a.m. LTST CRISM observation of the same crater, taken four sols earlier, shows the ice on the opposite crater wall. The ices in both these images are best modeled as fine-grained (~50 μm) water ice overlying a silt-sand mixture (Figure 3.12), presumably cold-trapped onto the soil. The nighttime observation is significantly brighter than the daytime observation, perhaps due to a combination of a slightly thicker ice deposit (~165 μm vs. ~150 μm), a higher ice:dust ratio (40% ice vs. 30% ice), or different viewing geometry (g=83.1, i=77.4 vs. g=38.6, i=52.8).

3.3.3-c Nighttime: Surface Frost and Atmospheric Ice

Sixteen nighttime observations (3 a.m. LTST) were made over the Phoenix landing site between L_s~84° and L_s~154°. Prior to L_s~114°, the nighttime observations have high 3.17/1.5 band depth ratios (median ~104), indicating a high ice aerosol optical depth (>0.08; Figure 3.13). Two observations (L_s~104° and 109°, sols 61 and 70) have 3.17/1.5 ratios less than 50, indicating either exceptionally high ice optical depth, or a significant contribution from surface ice.

The nighttime water ice spectrum is best-fit by a thin layer (~115 μm) of ~30% 20-μm water ice with ~70% 30-μm dust overlying sand-sized (2 mm) soil particles (X^2=0.197) (Figure 3.14a). Alternative layer configurations (e.g., ice over icy dust, a single layer of icy dust, etc.) did not fit the observed spectrum. The grain sizes for the overlying layer are well-constrained for both the ice and the soil; however, the underlying soil grain size is poorly constrained, except to say it must be sand-sized (>1 mm; Figure 3.14b). The thickness of the overlying ice-soil layer and the fraction of water ice in the upper layer are both well-constrained.

3.3.3-d Afternoon: Surface Frost and Atmospheric Ice

Similar to the nighttime ice pattern, afternoon ice absorptions are dominated by ice aerosols (3.17/1.5 ratios > 50) until L_s~154°, after which there are only five observations. The 3.17/1.5 ratios tend to be higher for afternoon surface ice absorptions, probably because the daytime ice optical depths are lower than those for the nighttime. Surface ice is dominating water ice absorptions after L_s~154° (Figure 3.13): the 3.17/1.5 band depth ratios of ~10 to ~30 over non-cloud-covered areas indicate a contribution from both surface ice and atmospheric ice. The surface ice is best modeled as a thin layer (~100 μm) of ~15% 20-μm water ice with ~85% 15-μm dust overlying sand-sized (2 mm) soil particles (X^2=0.089) (Figure 3.16a). As with previous observations, the sand size is poorly constrained (Figure 3.16b), while the other variables are better constrained (Figure 3.16C-D).

Afternoon water ice clouds were observed in CRISM images starting at L_s~157° (Figure 3.17). The clouds appeared as distinct hazes in the FRT and had obvious 1.5 and 3.17 μm water ice absorptions, with 3.17/1.5 band depth ratios of ~50 to 165, indicating a combination of surface ice and atmospheric ice. Phoenix's LIDAR instrument did not detect afternoon clouds during surface operations, which ended at L_s~149° [*Whiteway et al.,* 2009]

3.4 Discussion

3.4.1 Ice-Free Soils

CRISM spectra over the Phoenix landing site are consistently best-fit only by including a sand-sized (2 mm) component to the lower layer of soil (adding it to the upper layer darkens the spectrum more than is observed). Phoenix's OM experiment measured a mean grain size of ~90 μm by mass [*Pike*, personal communication]. However, the OM experiment is biased toward smaller grain sizes, because samples were first delivered to the imaging substrate, then rotated 90 degrees prior to imaging, and, as a result of tilting, larger particles may have fallen off. Additionally, Phoenix observations indicate that the soil was highly cohesive and large aggregates of small particles were commonly observed [*Arvidson et al.,* 2009]. RAC images of soil attached to the "divot" of the Icy Soil Acquisition Device (ISAD; *Bonitz et al.,* 2008) routinely show aggregates of soil on the order of 5 mm (in for example, RAC images RS 072 EFF 902585678_18230MB M1 and RS 099 FFL 904986760_1B7F0MR M1). We therefore conclude that the 2-mm "grains" needed for modeling these spectra are in fact aggregates of small particles that behave like larger grains.

Ice-free spectra have a slight negative slope between 2.3 and 2.6 μm, caused by the strong water absorption near 3 μm, indicating a low level of hydration or adsorption of water, an effect seen throughout the northern hemisphere in both CRISM and OMEGA data [*Joulet et al.,* 2007; *Poulet et. al.* 2008]. *Milliken et al.,* [2007] speculated that this was due to hydrated minerals, which contributed ~10 wt.% water to the surface. However, the lack of a 1.9 μm absorption argues against the water feature being due to hydrated mineral phases. Additionally, surface samples analyzed by the Thermal Evolved Gas Analyzer (TEGA) contained less than ~1 wt % water [*Smith et. al.* 2009]. *Arvidson et al.,* [2009] proposes that the 1.9- and 3-μm bands are more likely due to thin layers of water molecules adsorbed onto the surface.

3.4.2 The Appearance of Ice

This study first observed nighttime water ice on the surface around L_s~109°, corresponding to sol 70 of Phoenix operations. Although MARCI images taken during the L_s~109° observation show bright water ice clouds west of the landing site, SSI imaging at 7 a.m. LTST on the morning of sol 71 show no water ice aerosols [*Tamppari et al.,* 2009], indicating that the water ice signature observed by CRISM is most likely from surface frost. The LIDAR (LIght Detection And Ranging) instrument first observed nighttime water ice clouds at L_s~111° [*Whiteway et al.,* 2009]. After L_s~114°, the nighttime 3.17/1.5 band depth ratio is consistently low, indicating that most of the ice absorptions are coming from surface ice (Figure 3.13). The SSI first observed frost on the surface on sol 79 (L_s~112°) at ~6 a.m. LTST. The next sol, it observed 2 a.m. LTST frost on the telltale experiment, and afternoon (1 p.m.) frost in the shadows of large rocks (Figure 3.15). The low 3.17/1.5 band depth ratio and appearance of water ice absorptions lead us to conclude that the first water ice condenses on the surface in the nighttime between L_s~104° and 109°.

We observed water ice form on the surface in the afternoon at L_s~154°, earlier than CRISM observations in the previous year [*Cull et al., 2010a*]. During the 2007 observing cycle, CRISM first observed afternoon (3 p.m. LTST) water ice on the surface at L_s~167° [*Cull et al., 2010a*]; however, the 2007 observations were not directly over the Phoenix landing site – most were 1-2 degrees below the landing site.

Phoenix SSI images first show evidence of afternoon (1 p.m. LTST) water ice in the shadows of large rocks on operations sol 80 (L_s~112°; Figure 3.15). Ice was also observed later in the mission on the shadowed walls of trenches. Presumably, this is remnant ice from nighttime frost deposits. Ice does not appear to be stable on the sunlit surface until after L_s~154°.

3.5 Conclusions

Surface scattering parameters at the Phoenix landing site are well-approximated by scattering parameters that also fit model observations of Gusev Crater soils [e.g. *Johnson et al.,* 2006], presumably because they are both dusty plains surfaces.

Figure 3.18 summarizes the seasonal ice cycle at the Phoenix landing site based on CRISM and HiRISE observations prior to, during, and immediately after Phoenix operations, combined with Phoenix ground measurements by the SSI, OM and LIDAR instruments.

- During late spring and early summer (L_s~59° to ~109°), the surface is ice-free. The continued presence of a 3-μm water band during this time period indicates the surface is hydrated, probably by a thin layer of water adsorbed onto surface grains.

- Permanent patches of water ice in the shadowed sides of Heimdal and large mountains to the northeast exist throughout the summer, and do not appreciably grow or shrink. The permanent ices darken between L_s~119° and L_s~160°, possibly due to the sublimation or sintering of fine-grained ices cold-trapped onto the ice deposits during the spring defrost period.
- CRISM observations indicate the first nighttime (3 a.m. LTST) surface frosts form at L_s~109°, consisting of fine-grained (~20 μm) water ices.
- SSI onboard Phoenix saw the first early morning (6 a.m. LTST) frosts at L_s~112°.
- LIDAR onboard Phoenix saw the first nighttime water ice clouds at L_s~111° [*Whiteway et al.,* 2009]. LIDAR did not observe daytime water ice clouds during operations (L_s~77° to ~149°).
- CRISM observes the first afternoon (3 p.m. LTST) water ice clouds form at L_s~157°.
- In 2007, CRISM observed the first afternoon (3 p.m. LTST) water ice form on the surface at L_s~165° [*Cull et al., 2010a*]. In 2009, the first afternoon water ice formed on the surface sometime around L_s~156°.
- CRISM does not observe CO_2 frost form on the surface before CRISM observations cease at L_s~177°, its final observation before the onset of the polar hood.

Figures

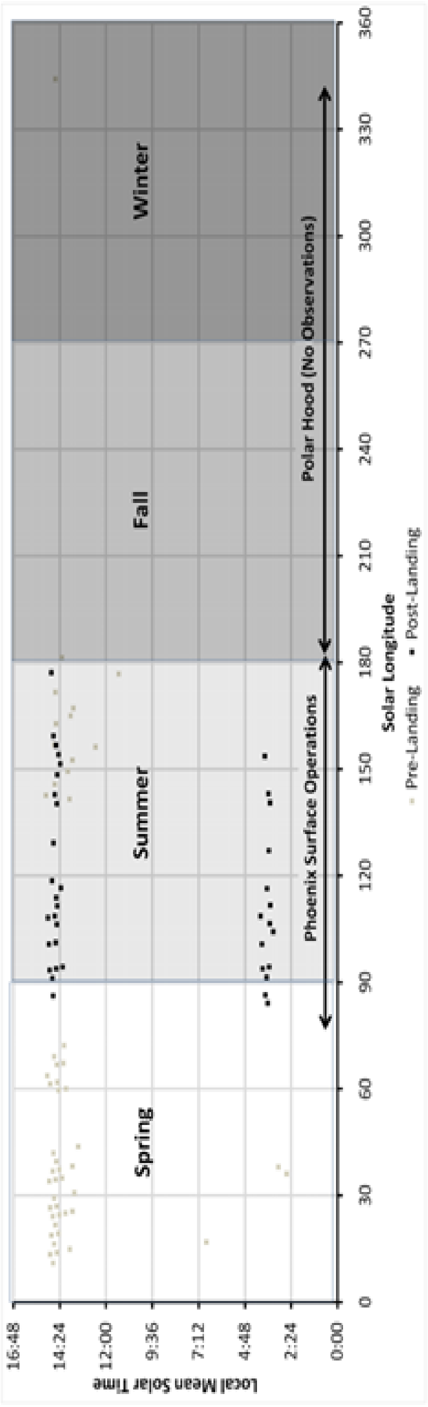
Local Mean Solar Time
16:48
14:24
12:00
9:36
7:12
4:48
2:24
0:00
0
30
60
90
120
150
180
210
240
270
300
330
360
Solar Longitude
Spring
Summer
Fall
Winter
Phoenix Surface Operations
Polar Hood (No Observations)
Pre-Landing
Post-Landing

Figure 3.1 - CRISM FRT observations over the Phoenix landing site.

Gray squares are pre-landing observations examined in *Cull et al., [2010]*. Black squares are post-landing observations examined here. All of the observations considered in this paper were taken either at 3 p.m. LTST or 3 a.m. LTST. No observations were taken between L_s~181° and 344° due to the presence of the polar hood.

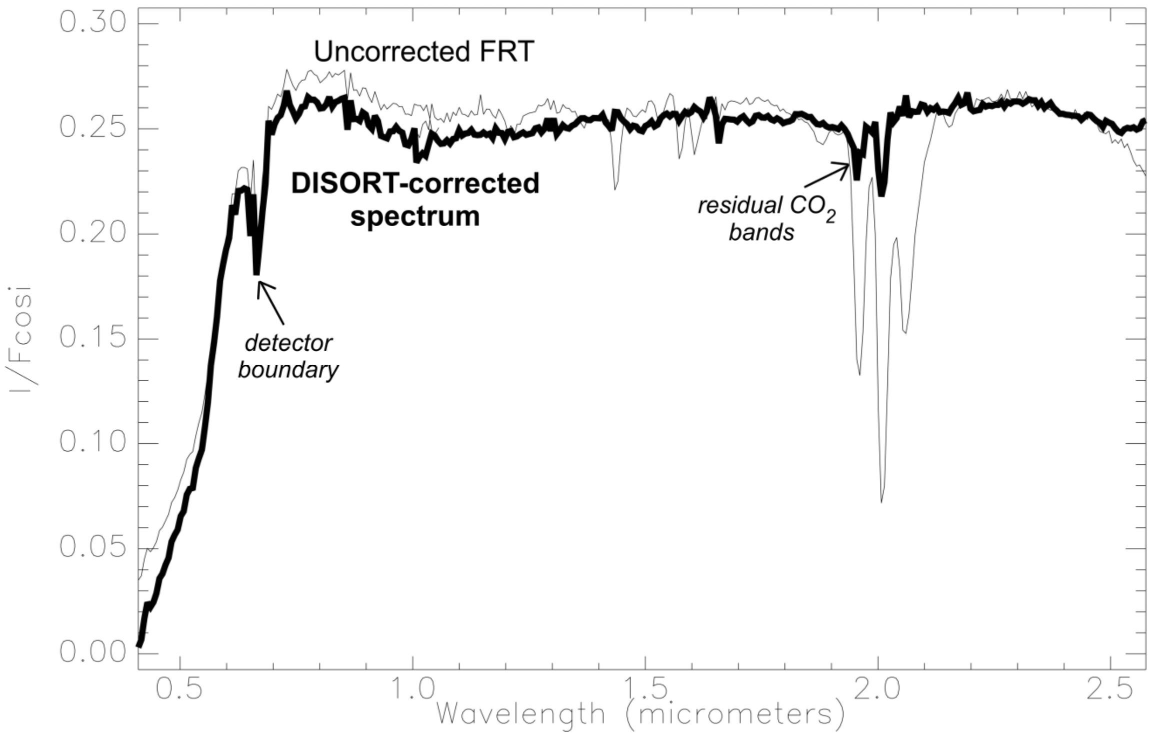

Figure 3.2 - Uncorrected vs. corrected spectra.

CRISM spectrum over Phoenix landing site (thin line), and DISORT-corrected spectrum (thick line). The sharp feature at ~0.65 μm is a detector boundary, and the two narrow features in the DISORT-corrected spectrum at 1.954 and 2.007 μm are residual CO_2 gas features.

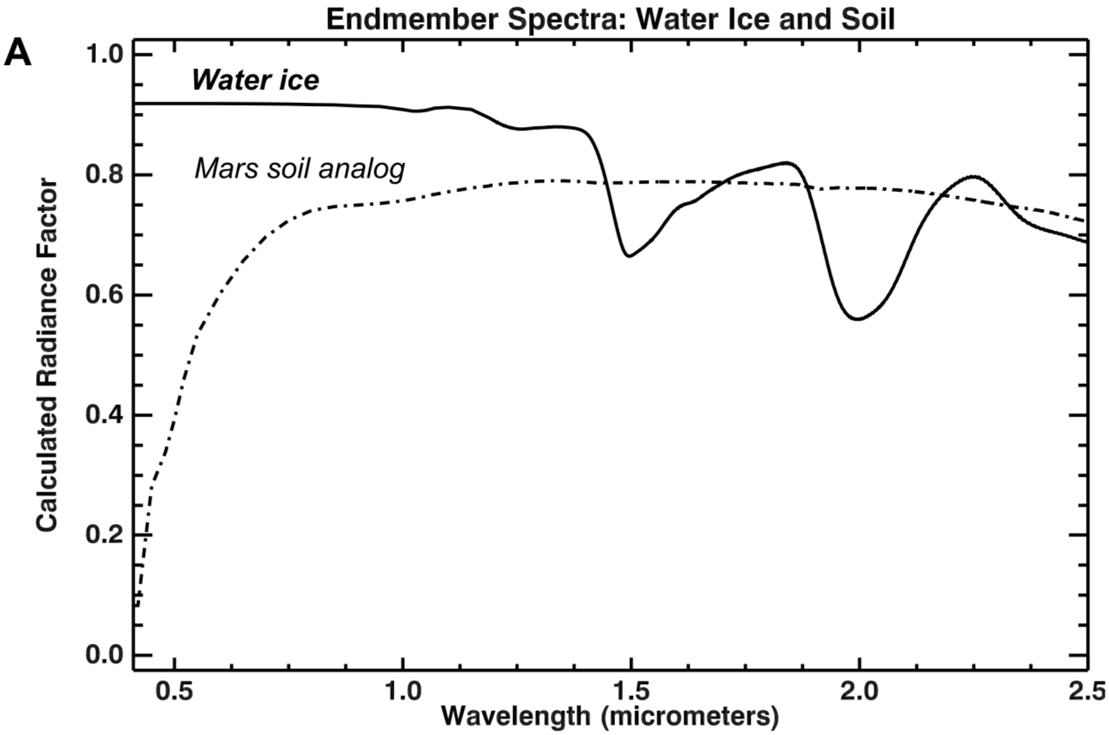

Endmember Spectra: Water Ice and Soil

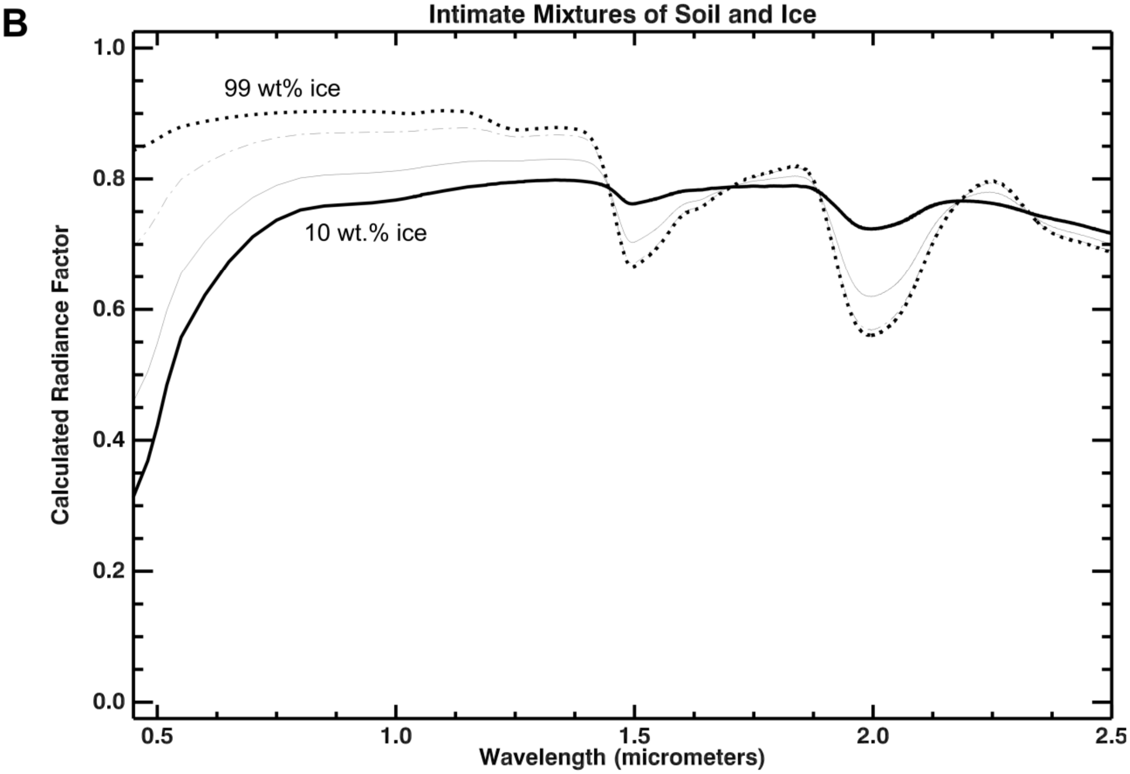

Intimate Mixtures of Soil and Ice

Figure 3.3 – Mixtures of spectral components.

A) Example spectra for 10-μm water ice (solid line) and 5-μm Mars soil analog (dotted line). Water ice is featureless at shorter wavelengths, and has strong absorptions at 1.5 μm, 2.0 μm, and a distinctive negative slope between 2.3 and 2.6 μm. Soil is featureless at longer wavelengths, but has a sharp "red edge" at short wavelengths. B) Examples of intimate mixtures of soil and ice with various mass ratios: 10 wt% ice (heavy line), 50 wt% ice (thin line), 90 wt% ice (dash-dotted line), and 99 wt% ice (dotted line). Dust mass fractions greater than ~90 wt% will mask water ice absorptions; however, >99 wt% ice is needed to completely mask the ferric red edge. In these examples, we assume a viewing geometry representative of CRISM observations over Phoenix: i=54.0°, e=32.0°, g=42.0°.

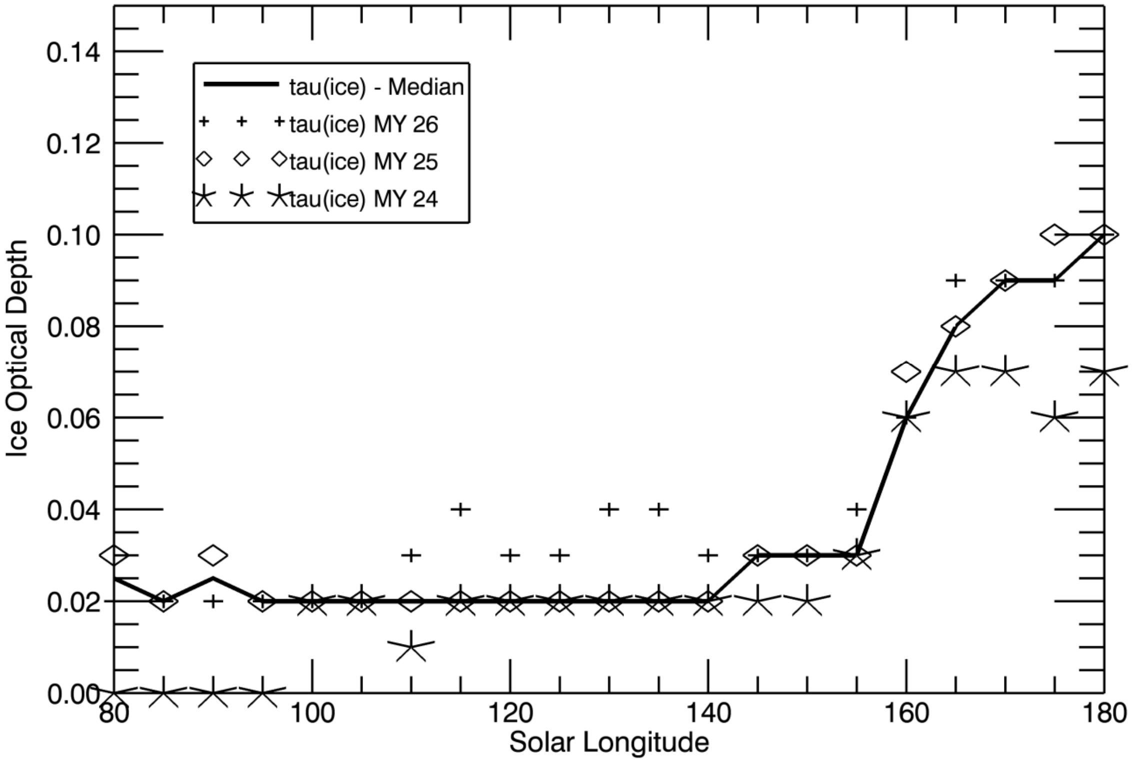

Figure 3.4 - Historical ice aerosol optical depths.

Ice optical depths as observed by TES for Mars Year (MY) 24, 25, and 26.

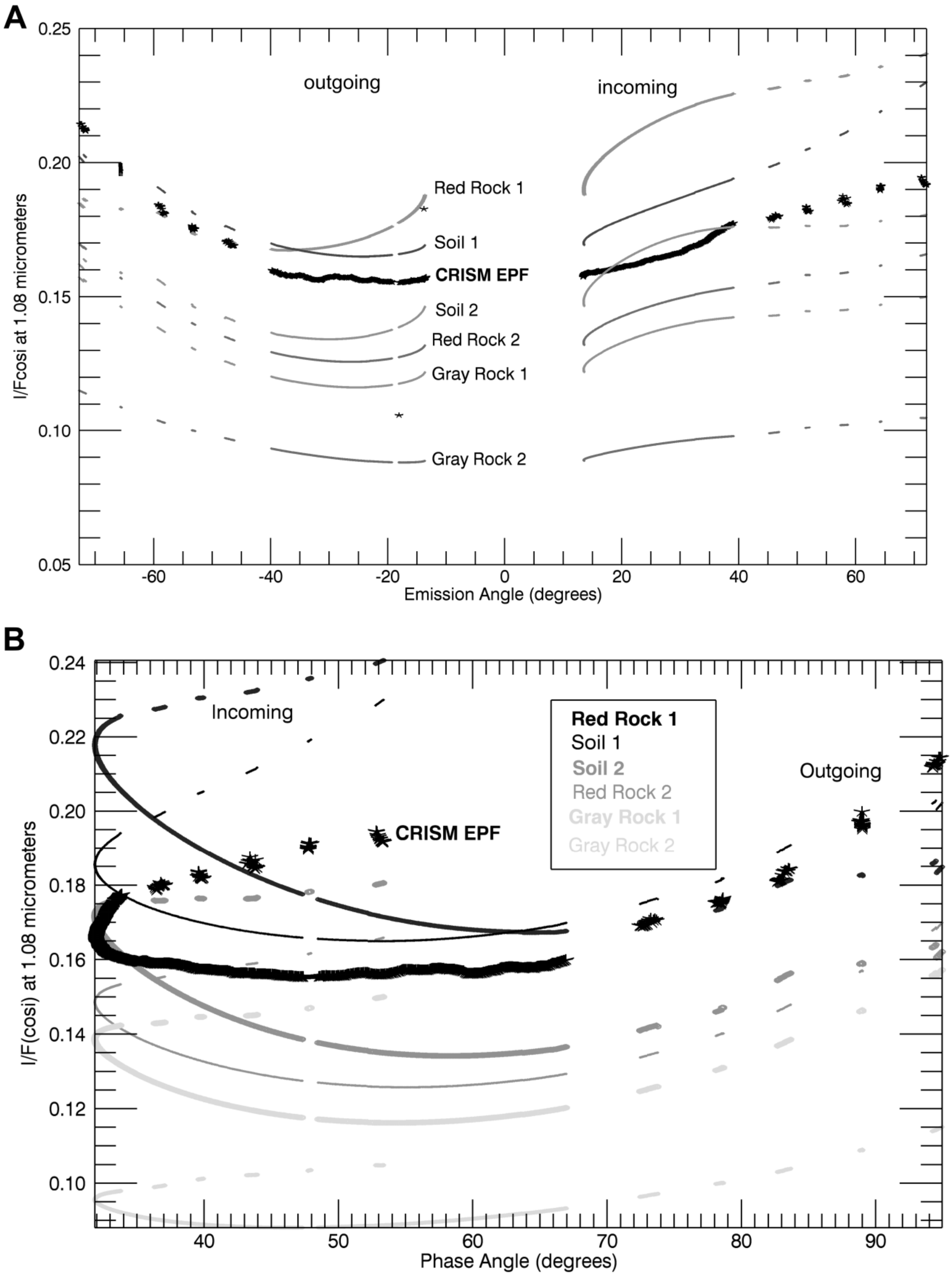
A
0.25
0.20
0.15
0.10
0.05
I/Fcosi at 1.08 micrometers
outgoing
incoming
Red Rock 1
Soil 1
CRISM EPF
Soil 2
Red Rock 2
Gray Rock 1
Gray Rock 2
-60
-40
-20
0
20
40
60
Emission Angle (degrees)
B
0.24
0.22
0.20
0.18
0.16
0.14
0.12
0.10
I/F(cosi) at 1.08 micrometers
Incoming
CRISM EPF
Red Rock 1
Soil 1
Soil 2
Red Rock 2
Gray Rock 1
Gray Rock 2
Outgoing
40
50
60
70
80
90
Phase Angle (degrees)

Figure 3.5 – Simulating CRISM coverage for various viewing geometries.

DISORT models (gray lines) simulating FRT0000B1D2 (black line) over the Phoenix landing site for various emergence (A) and phase (B) angles. Each gray line represents a Hapke surface with scattering parameters (*w*, δ, f, B0, h) from one of the Gusev Crater materials described by *Johnson et al.*, [2006]. The surfaces were overlaid with a model atmosphere based on FRT0000B1D2, and the viewing geometry varied to observe the effects on radiance. The emergence angle gap between -13° and 13° is due to the spacecraft roll angle during acquisition.

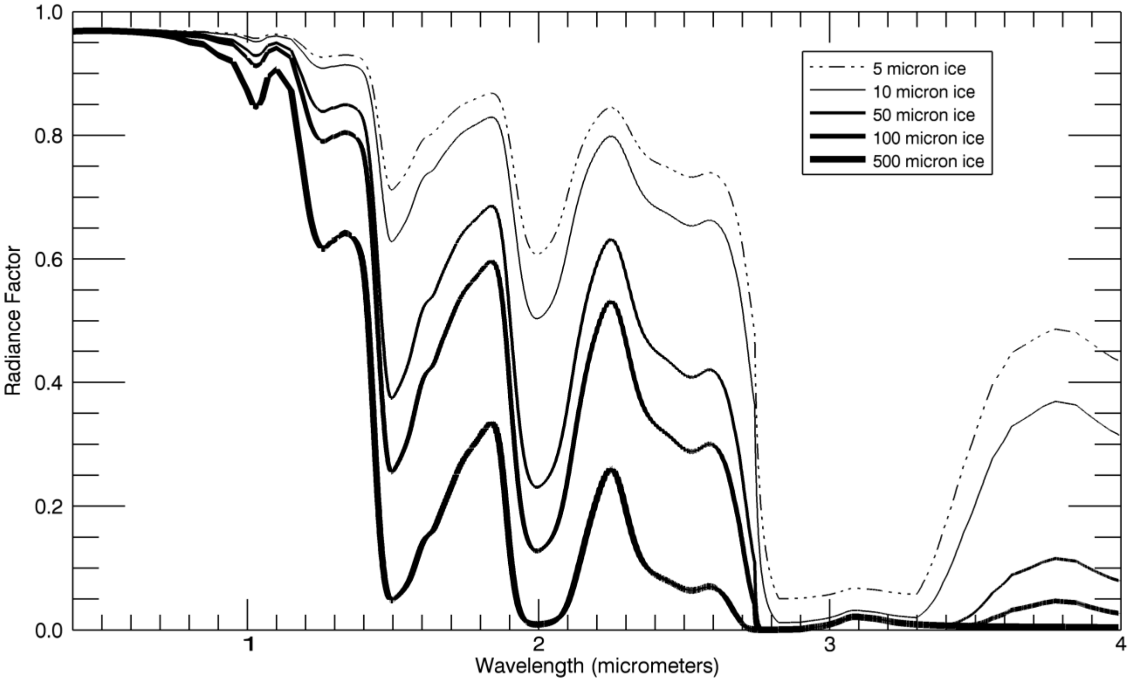

Figure 3.6 – Affect of grain size on 3.17/1.5 μm band depth ratio.

The 3.17 μm water ice band saturates for even small grain sizes, resulting in a small 3.17/1.5- μm band depth ratio. For larger grain sizes, as the 1.5 μm band nears saturation, the 3.17/1.5- μm band depth ratio approaches 1.

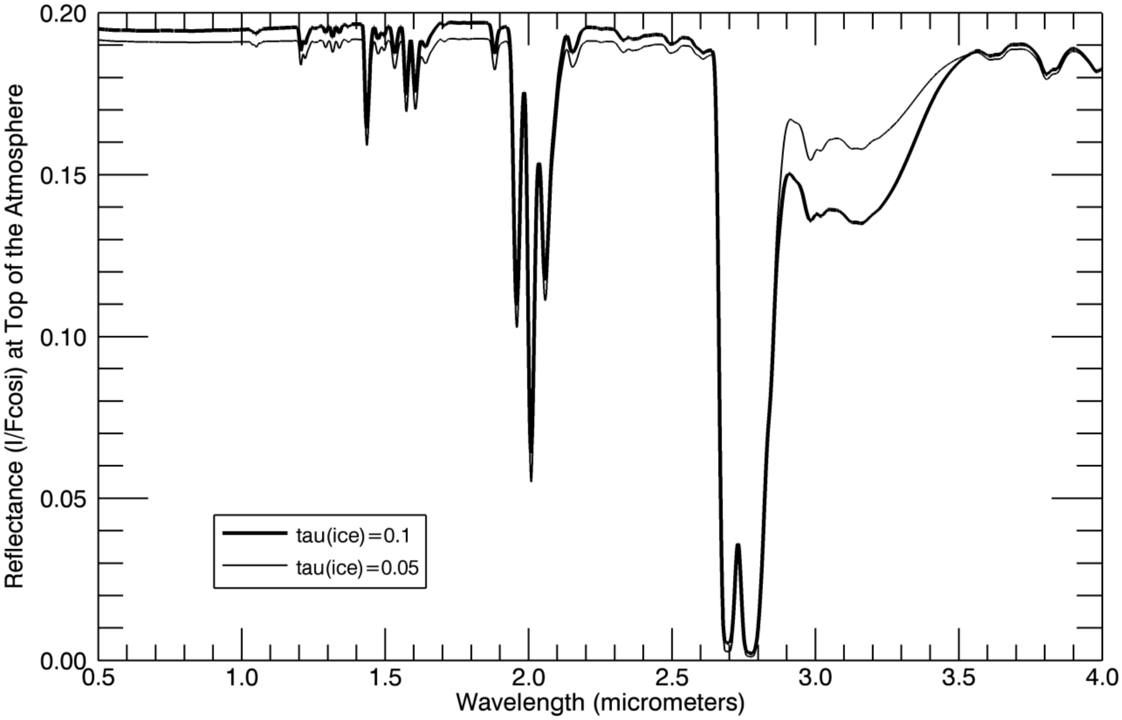

Figure 3.7 – Affect of ice opacity on 3.17 /1.5 µm band depth ratio.

The 1.5 µm absorption is shallow for all opacities; whereas, the 3.17 µm absorption deepens significantly with increasing opacity. The result is a high 3.17/1.5- µm band depth ratio that only falls below 100 for ice opacities greater than ~0.1. Ice opacities are relative to 12.1 µm.

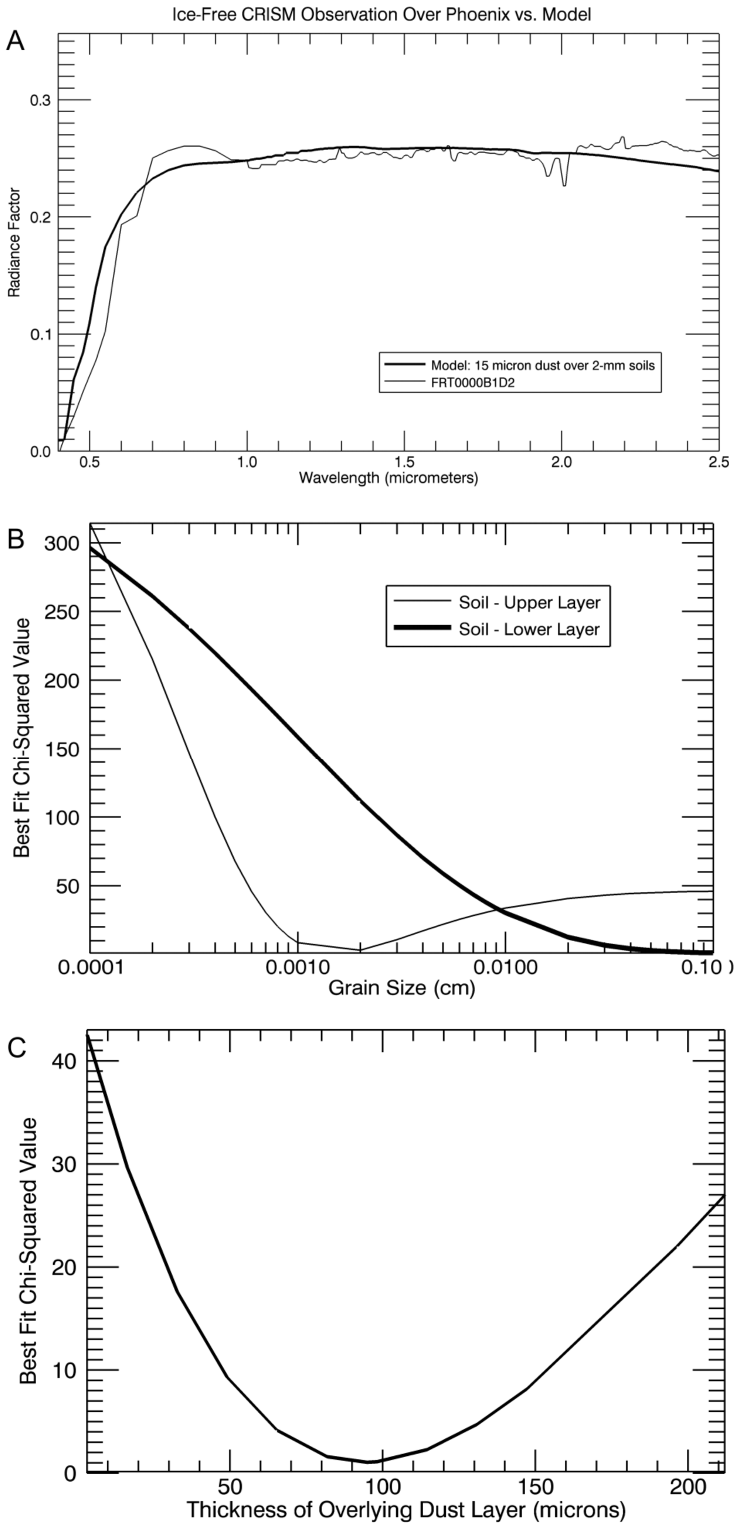
A
Ice-Free CRISM Observation Over Phoenix vs. Model
Radiance Factor
0.0
0.1
0.2
0.3
0.5
1.0
1.5
2.0
2.5
Wavelength (micrometers)
Model: 15 micron dust over 2-mm soils
FRT0000B1D2
B
Best Fit Chi-Squared Value
50
100
150
200
250
300
0.0001
0.0010
0.0100
0.10
Grain Size (cm)
Soil - Upper Layer
Soil - Lower Layer
C
Best Fit Chi-Squared Value
0
10
20
30
40
50
100
150
200
Thickness of Overlying Dust Layer (microns)

Figure 3.8 – Ice-free spectra over Phoenix

A) Ice-free summer spectrum over the Phoenix landing site (FRT0000B1D2, thin line), and model results (thick line). The spectrum is best modeled by a ~100- µm thick layer of silt-sized particles (~15- µm) overlying sand-size particles (~2 mm). B) Sensitivity analysis for grain sizes and (C) thickness of dust layer.

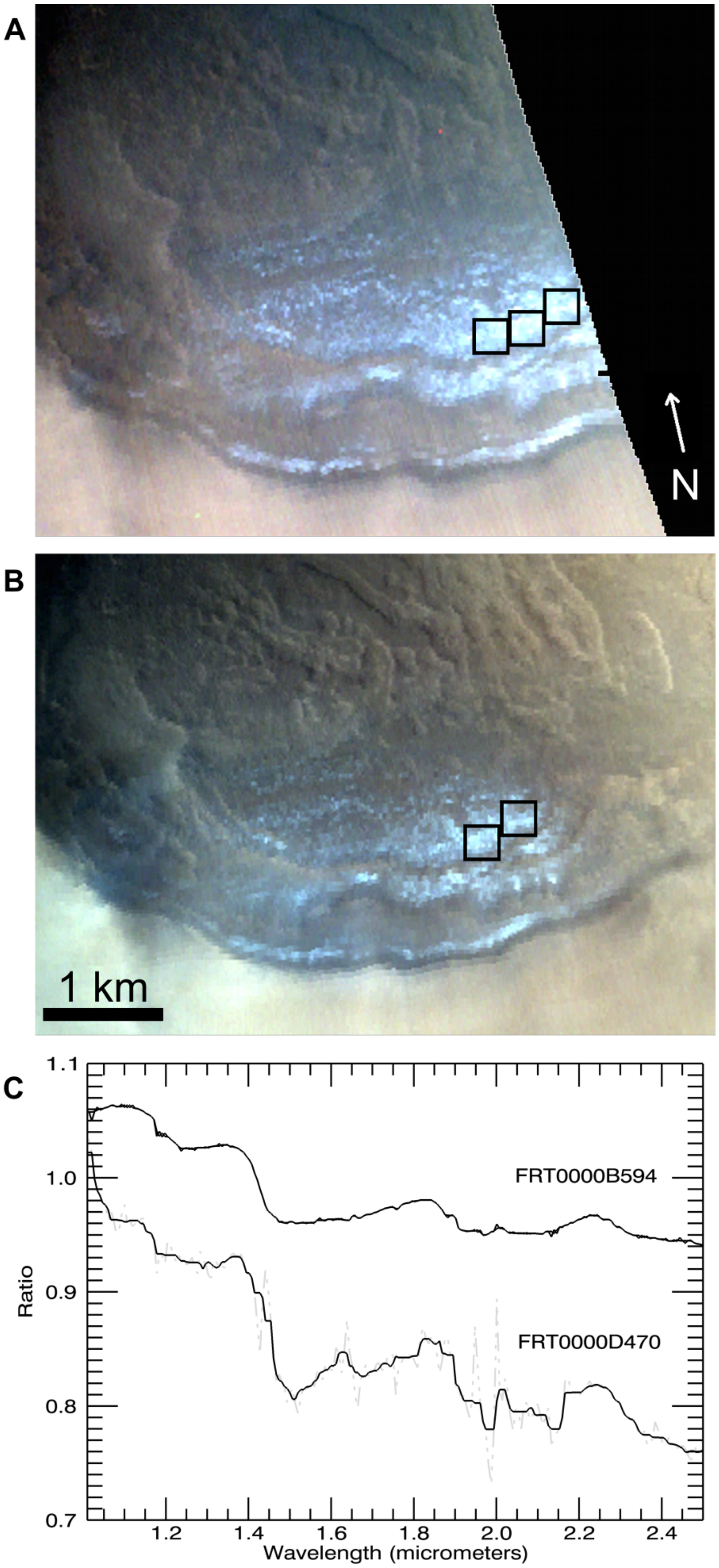
A
N
B
1 km
C
1.1
1.0
0.9
0.8
0.7
Ratio
FRT0000B594
FRT0000D470
1.2
1.4
1.6
1.8
2.0
2.2
2.4
Wavelength (micrometers)

Figure 3.9 - Permanent H_2O ice, north-facing slopes of Heimdal.

A) FRT0000B594, L_s~94°. B) FRT0000D470, L_s~154°. C) Ratio spectra of icy patches to non-icy patches (dotted gray lines) and with a median filter applied (solid lines). The absorptions at 1.5 and 2.0 μm are due to water ice.

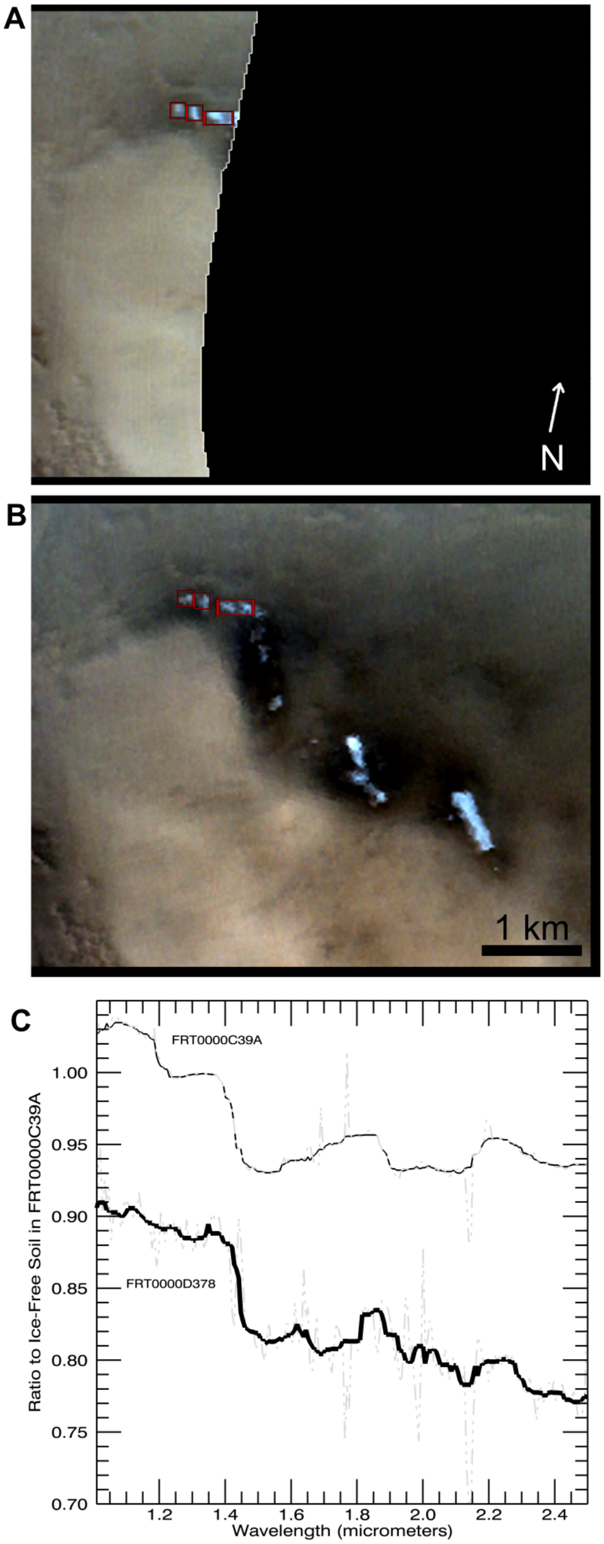
A
N
B
1 km
C
FRT0000C39A
FRT0000D378
Ratio to Ice-Free Soil in FRT0000C39A
1.00
0.95
0.90
0.85
0.80
0.75
0.70
1.2
1.4
1.6
1.8
2.0
2.2
2.4
Wavelength (micrometers)

Figure 3.10 - Permanent water ice, north-facing slopes of plateau.

This plateau is just northeast of Heimdal Crater. A) FRT0000C39A, L_s~119°. B) FRT0000D378, L_s~151°. C) Ratio spectra of icy patches to non-icy patches (dotted gray lines) and with a median filter applied (solid lines). The absorptions at 1.5 and 2.0 μm are due to water ice.

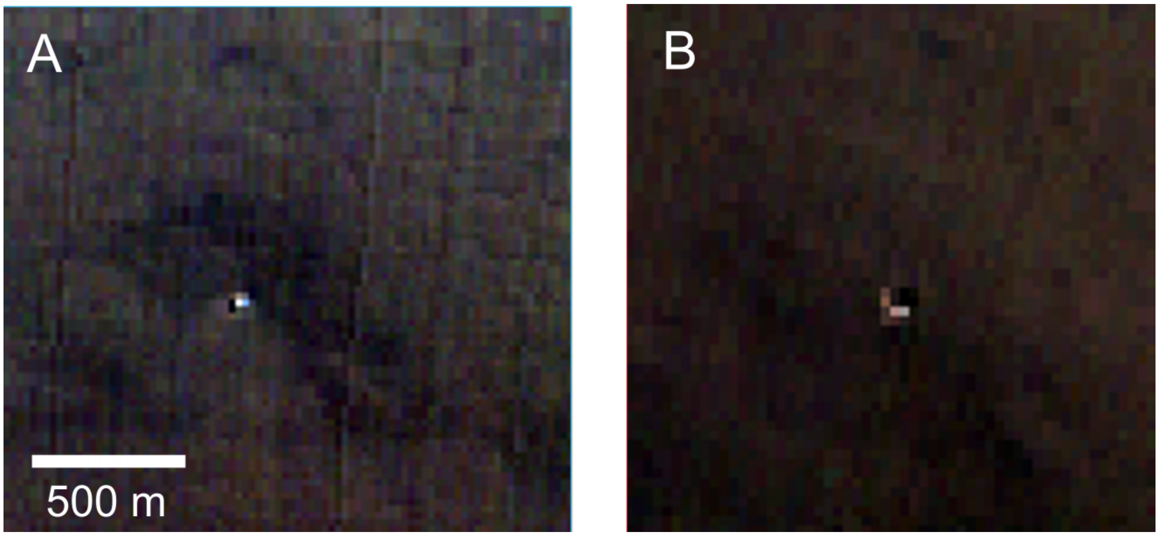

Figure 3.11 - Water ice in "Runaround Crater."

Runaround Crater is an 85-meter crater northeast of the Phoenix landing site. A) FRT0000B1D2, L_s~86°, 3 p.m. LTST. B) FRT0000B079, L_s~84°, 3 a.m. LTST. In the nighttime image, the ice has moved from one crater wall to the opposite, avoiding the sunlight.

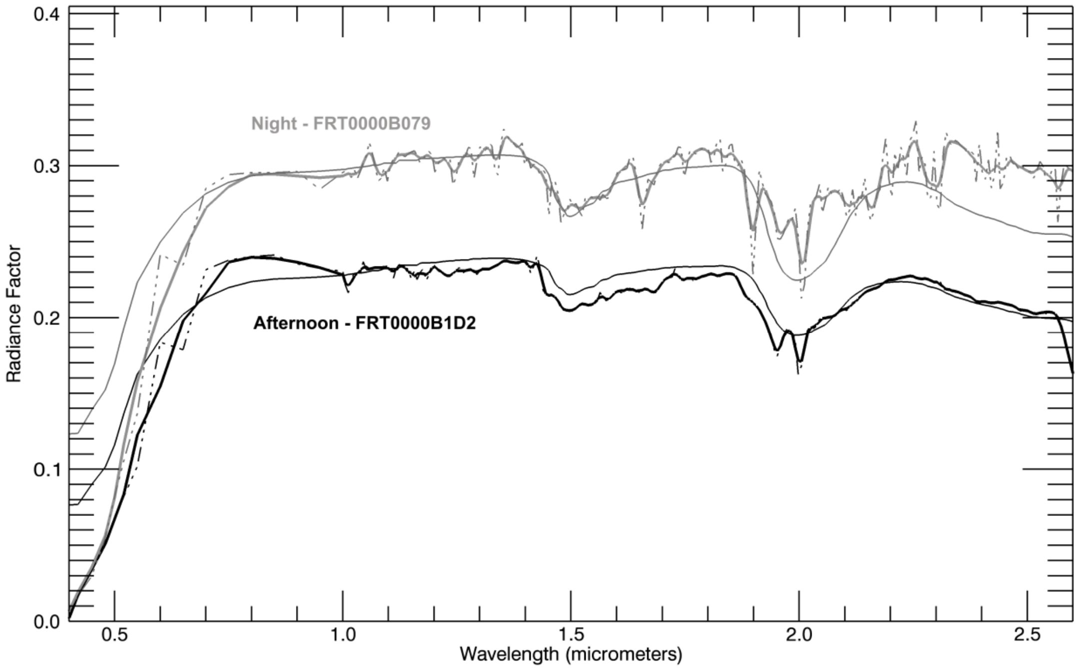

Figure 3.12 – CRISM spectra of "Runaround Crater".

CRISM spectra of ice (thick lines) in the 85-meter crater at 3 p.m. (black) and 3 a.m. (gray) with model results (thin lines) for each. The afternoon observation is modeled an ~150 μm -thick layer of 50-μm ice overlying a typical ice-free mixture (silt- and sand-sized particles). The nighttime observation is best-modeled as a slightly thicker (~165 μm) layer of 50 μm ice over the same mixture.

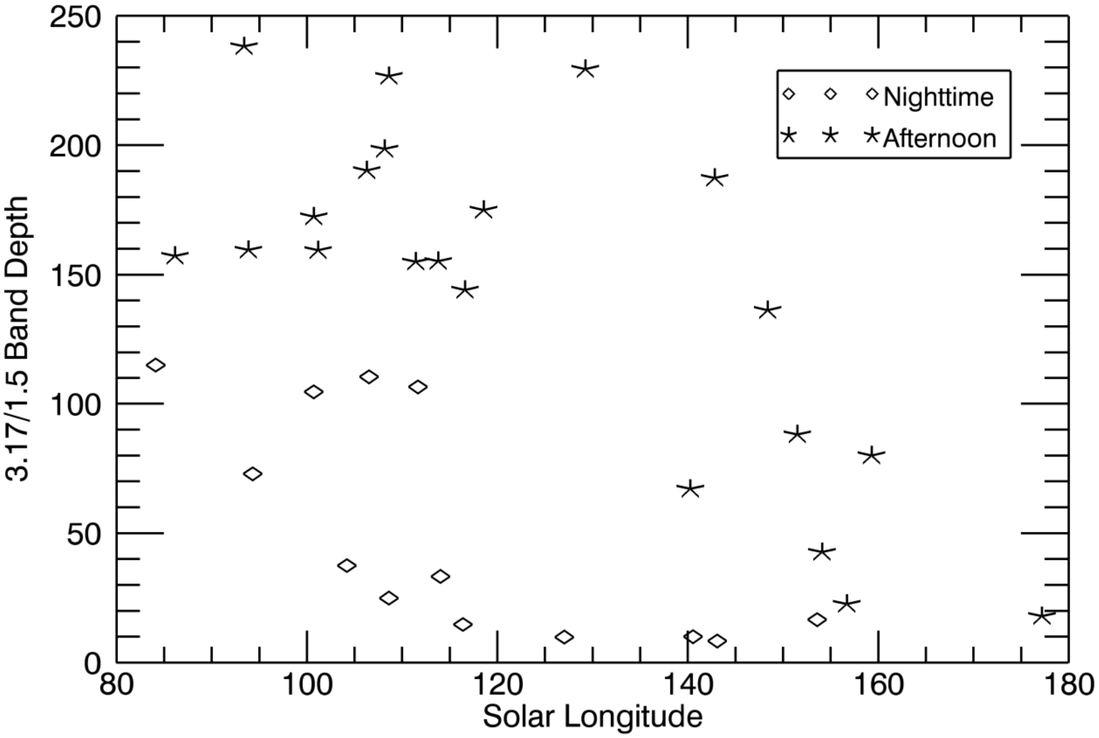

Figure 3.13 - The 3.17/1.5-µm band depth ratio through time.

Measurements of the ratio for CRISM observations over the Phoenix landing site, through time. In the late spring and early summer, the ratios are higher, indicating small ice optical depths and no surface ice. The nighttime ratios drop quickly starting at Ls~104°, indicating a growing contribution from surface ice. The afternoon ratios begin dropping around Ls~155°.

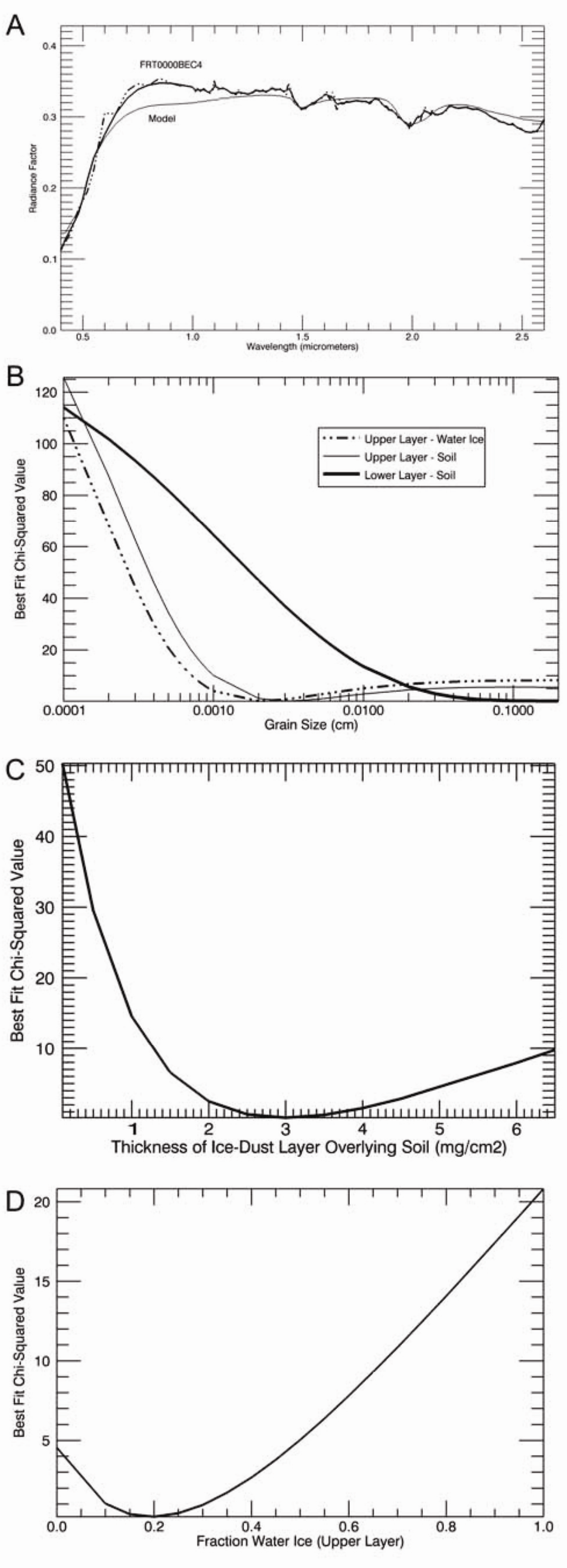
A
FRT0000BEC4
Model
Radiance Factor
0.0
0.1
0.2
0.3
0.4
0.5
1.0
1.5
2.0
2.5
Wavelength (micrometers)
B
Upper Layer - Water Ice
Upper Layer - Soil
Lower Layer - Soil
Best Fit Chi-Squared Value
20
40
60
80
100
120
0.0001
0.0010
0.0100
0.1000
Grain Size (cm)
C
Best Fit Chi-Squared Value
10
20
30
40
50
1
2
3
4
5
6
Thickness of Ice-Dust Layer Overlying Soil (mg/cm2)
D
Best Fit Chi-Squared Value
5
10
15
20
0.0
0.2
0.4
0.6
0.8
1.0
Fraction Water Ice (Upper Layer)

Figure 3.14 – Nighttime spectra over the Phoenix landing site.

A) Nighttime spectrum over the Phoenix landing site (FRT0000BEC4, thick line), and model results (thin line): a thin (~115 μm) layer of water ice (20 μm) and dust (30 μm) overlying sand-sized (2 mm) soil (X^2=0.1968). The absorptions at 1.5 and 2.0 μm are due to water ice. Sensitivity analysis on this model illustrates that (with all other parameters set to the above values) the grain sizes (B) are well-constrained at the lower end, but poorly constrained on the higher ends. The grain sizes of the lower layer of soil are particularly poorly constrained on the high end, being best-fit for grain sizes > 1 mm. The thickness of the overlying soil (C) and the fraction of water ice in the overlying layer (D) are well-constrained.

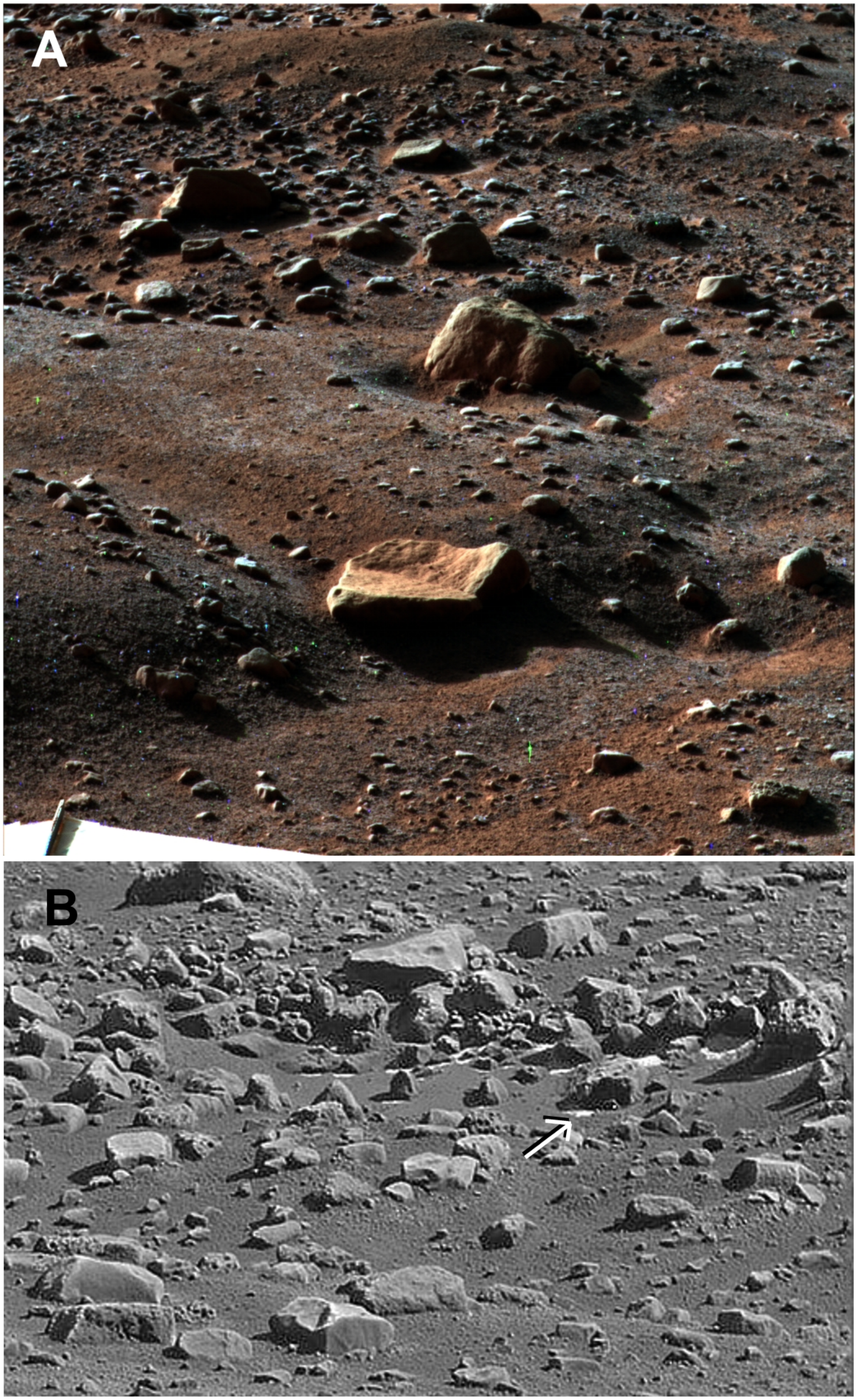
A
B

Figure 3.15 - Surface frost as seen by the Phoenix SSI instrument.

A) SSI false-color (R: 0.75 μm, G: 0.53 μm, B: 0.44 μm) composite of “Winkies” (an ~27-cm rock in the foreground) on Sol 79 at ~6 a.m. LTST. White-blue frost is visible on the soil behind Winkies. B) Ratio of SSI filters L2 to LC (0.445 μm to 0.967 μm) for “Jumping Cow” area on Sol 80 at ~1 p.m. LTST. The white patches on the shadowed sides of the rocks are interpreted to be water ice.

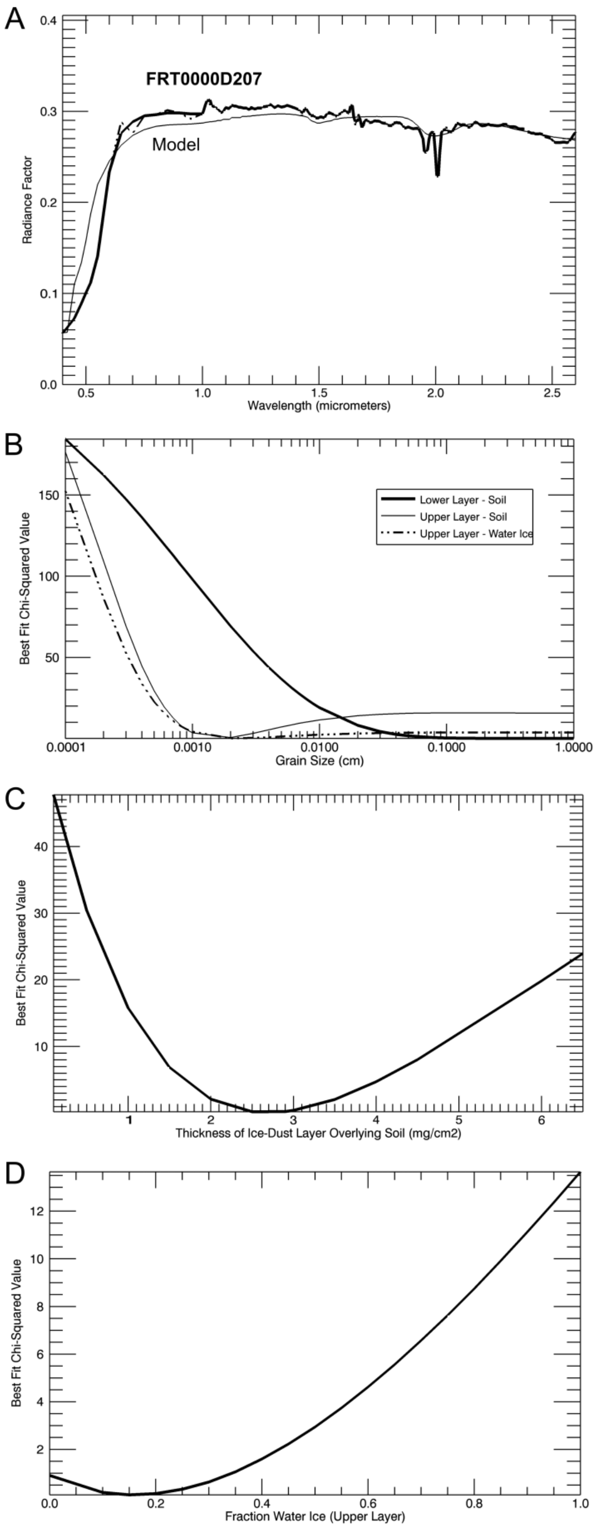
A
FRT0000D207
Model
Radiance Factor
0.0
0.1
0.2
0.3
0.4
Wavelength (micrometers)
0.5
1.0
1.5
2.0
2.5
B
Lower Layer - Soil
Upper Layer - Soil
Upper Layer - Water Ice
Best Fit Chi-Squared Value
50
100
150
Grain Size (cm)
0.0001
0.0010
0.0100
0.1000
1.0000
C
Best Fit Chi-Squared Value
10
20
30
40
Thickness of Ice-Dust Layer Overlying Soil (mg/cm2)
1
2
3
4
5
6
D
Best Fit Chi-Squared Value
2
4
6
8
10
12
Fraction Water Ice (Upper Layer)
0.0
0.2
0.4
0.6
0.8
1.0

Figure 3.16 - Afternoon frost at the Phoenix landing site.

A) Afternoon surface frost at the Phoenix landing site (thick line, FRT0000D207) vs. model result (thin line): a thin layer (~100 μm) of ~15% 20-μm water ice with ~85% 15-μm dust overlying sand-sized (2 mm) soil particles (X^2=0.089). Sensitivity analyses were performed with all parameters set to these values, and only the parameter of interest allowed to vary.

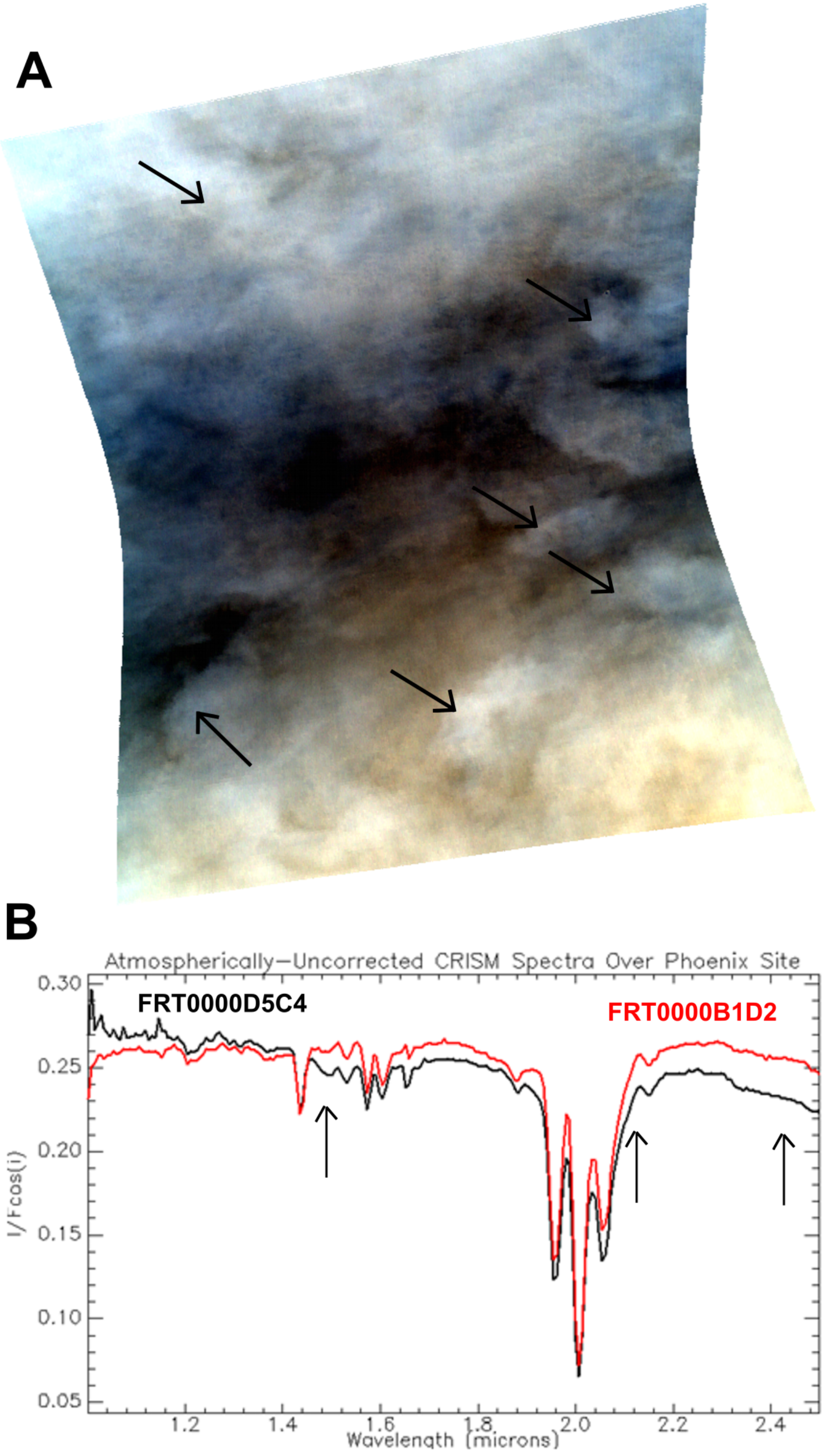
A
B
Atmospherically-Uncorrected CRISM Spectra Over Phoenix Site
FRT0000D5C4
FRT0000B1D2
I/Fcos(i)
0.30
0.25
0.20
0.15
0.10
0.05
1.2
1.4
1.6
1.8
2.0
2.2
2.4
Wavelength (microns)

Figure 3.17 - Afternoon clouds over the Phoenix landing site.

A) False-color CRISM observation of afternoon clouds over the Phoenix landing site (FRT0000D5C4, R: 0.7097 µm, G: 0.5989 µm, B: 0.5337 µm). B) Cloudy spectrum (black, an average of the areas marked by the black arrows above) compared to a spectrum with low ice aerosols (FRT0000B1D2, red). The cloudy observation has a clear water ice absorption at 1.5 µm, and the shape of the spectrum has changed significantly at 2.0 µm and between 2.3 and 2.5 µm.

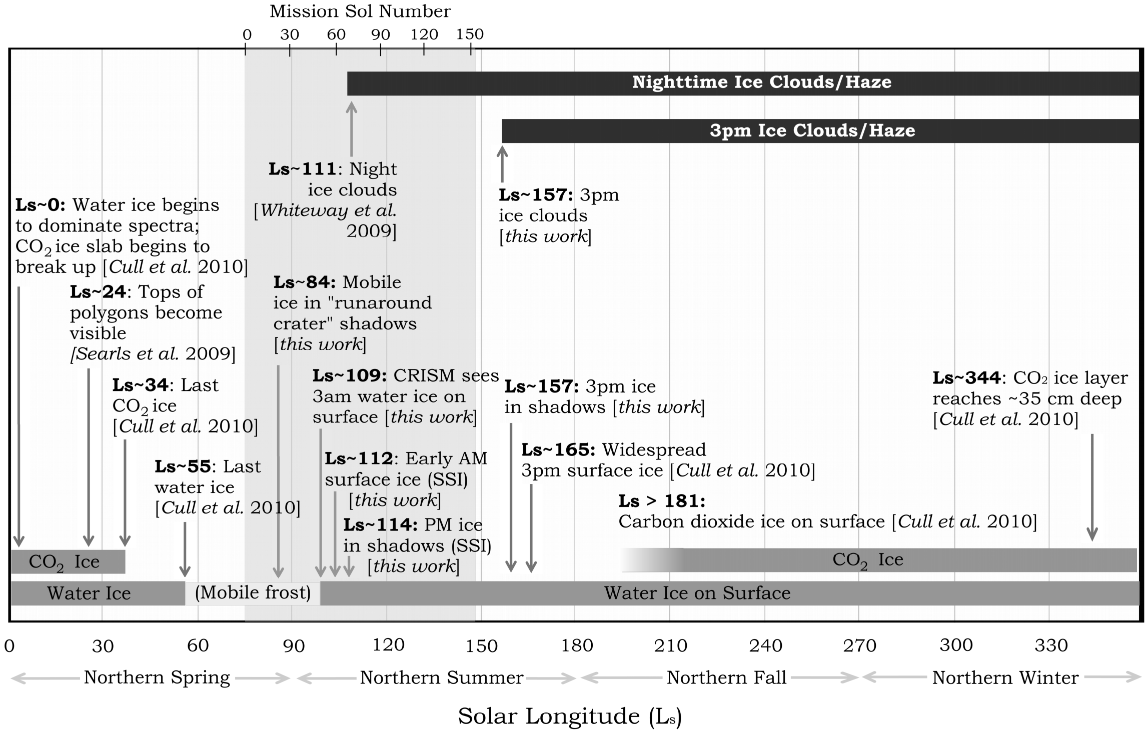

Figure 3.18 - The seasonal ice cycle at the Phoenix landing site.

References

Arvidson, R. E., J. L. Gooding, and H. J. Moore (1989), The Martian Surface as Imaged, Sampled, and Analyzed by the Viking Landers, *Reviews in Geophysics*, 27(1), 39–60.

Arvidson, R.E., F. Poulet, J.-P. Bibring, M. Wolff, A. Gendrin, R. V. Morris, J. J. Freeman, Y. Langevin, N. Mangold, G. Bellucci (2005), Spectral reflectance and morphologic correlations in Eastern Terra Meridiani, Mars, *Science* 307(5715), 1591-1594, DOI: 10.1126/science.1109509.

Arvidson, R. E., S. Squyres, R. Anderson, J. Bell, D. Blaney, J. Bruckner, N. Cabrol, W. Calvin, M. Carr, P. Christensen, B. Clark, L. Crumpler, D. Des Marais, P. de Souza, D. 'd'Uston, T. Economou, J. Farmer, W. Farrand, W. Folkner, M. Golombek, S. Gorevan, J. Grant, R. Greeley, J. Grotzinger, E. Guinness, B. Hahn, L. Haskin, K Herkenhoff, J. Hurowitz, S. Hviid, R. Johsson, G. Klingerlhofer, A. Knoll, G. Landis, C. Leff, M. Lemmon, R. Li, M. Madsen, M. Malin, S. McLennan, H. McSween, D. Ming (2006), Overview of the Spirit Mars Exploration Rover Mission to Gusev Crater: Landing site to Backstay Rock in the Columbia Hills, *Journal of Geophysical Research*, 111, E02S01, doi:10.1029/2005JE002499.

Arvidson, R.E., R. Bonitz, M. Robinson, J. Carsten, R. Volpe, A. Trebi-Ollennu, M. Mellon, P. Chu, K. Davis, J. Wilson, A. Shaw, R. Greenberger, K.

Siebach, T. Stein, S. Cull, W. Goetz, R. Morris, D. Ming, H. Keller, M. Lemmon, H. Sizemore, M. Mehta (2009), Results from the Mars Phoenix Lander Robotic Arm experiment, *Journal of Geophysical Research*, 114, E00E02, doi:10.1029/2009JE003408.

Bass, D. and D.A. Paige (2000) Variability of Mars' north polar water ice cap: II. Analysis of Viking IRTM and MAWD data. *Icarus*, 144: 297-409. doi:10.1006/icar.1999.6301

Bonitz, R. G., L. Shiraishi, M. Robinson, R. Arvidson, P. Chu, J. Wilson, K. Davis, G. Paulsen, A. Kusack, D. Archer, P. Smith. (2008), NASA Mars 2007 Phoenix Lander Robotic Arm and Icy Soil Acquisition Device, *Journal of Geophysical Research*, 113, E00A01, doi:10.1029/2007JE003030.

Brown, A.J., S. Bryne, L. Tornbene, T. Roush (2008) Louth crater: Evolution of a layered water ice mound. *Icarus* 196: 433-445. doi.org/10.1016/j.icarus.2007.11.023.

Clancy, R. T., S. W. Lee, G. R. Gladstone, W. W. McMillan, and T. Rousch (1995) A new model for Mars atmospheric dust based upon analysis of ultraviolet through infrared observations from Mariner 9, Viking, and Phobos, *Journal of Geophysical Research*, 100(E3), 5251–5263.

Clancy, R. T., M. J. Wolff, and P. R. Christensen (2003) Mars aerosol studies with the MGS TES emission phase function observations: Optical depths, particle sizes, and ice cloud types versus latitude and solar longitude, *Journal of Geophysical Research*, 108 (E9), 5098, doi:10.1029/2003JE002058.

Conrath, B. J., J. C. Pearl, M. D. Smith, W. C. Maguire, P. R. Christensen, S. Dason, and M. S. Kaelberer (2000), Mars Global Surveyor Thermal Emission Spectrometer (TES) observations: Atmospheric temperatures during aerobraking and science phasing, *Journal of Geophysical Research*, 105(E4), 9509–9519.

Cull, S.C., R.E. Arvidson, M. Mellon, S. Wiseman, R. Clark, T. Titus, RV Morris, P. McGuire (2010) Seasonal H_2O and CO_2 Ices at the Mars Phoenix Landing Site: Results from Pre-Landing CRISM and HiRISE Observations. *Journal of Geophysical Research*, 115, E00E19, doi:10.1029/2009JE003410.

Eluszkiewicz, J. (1993) On the microphysical state of the Martian polar caps. *Icarus* 103: 43-48.

Gaffey, S.J., L.A. McFadden, D. Nash, C.M. Pieters (1997) Ultraviolet, visible, and near-infrared reflectance spectroscopy: Laboratory spectra of geologic minerals. In Remote Geochemical Analysis: Elemental and Mineralogical Composition, C.M. Pieters and P.A.J. Englert (editors), Cambridge University Press.

Hapke, B. (1981), Bidirectional Reflectance Spectroscopy 1. Theory, *Journal of Geophysical Research*, 86(B4), 3039–3054.

Hapke, B. (1993) Theory of reflectance and emittance spectroscopy. Cambridge University Press: Cambridge, UK.

Hecht, M. H., J. Marshall, W. Pike, U. Staufer, D. Blaney, D. Braendlin, S. Gautsch, W. Goetz, H. Hidber, H. Keller, W. Markiewicz, A. Mazer, T. Melroy, J. Morookian, C. Mogensen, D. Parrat, P. Smith, H. Sykulska, R. Tanner, R. Reynolds, A. Tonin, S. Vijendran, M. Weilert, P. Woida (2008), Microscopy capabilities of the Microscopy, Electrochemistry, and Conductivity Analyzer, *Journal of Geophysical Research*, 113, E00A22, doi:10.1029/2008JE003077.

Heet, T., R.E. Arvidson, S.C. Cull, M.T. Mellon, K.D. Seelos (2009) Geomorphic and geologic settings of the Phoenix lander mission landing site. *Journal of Geophysical Research*, 114, E00E04, doi:10.1029/2009JE003416.

Henyey, L.G. and J.L. Greenstein (1941) Diffuse radiation in the galaxy, *Astrophysical Journal* 93:70-83, 1941.

James, P.B., H.H. Kieffer and D.E. Paige (1993) The Seasonal Cycle of Carbon Dioxide on Mars, in Mars (Hugh Kieffer, editor), University of Arizona Press: Tucson, Arizona.

Johnson, J., R. Kirk, L. Soderblom, L. Gaddis, R. Reid, D. Britt, P. Smith, M. Lemmon, N. Thomas, J. Bell, N. Bridges, R. Anderson, K. Herkenhoff, J. Maki, S. Murchie, A. Dummel, R. Jaumann, F. Trauthan, F. Arnold (1999), Preliminary results on photometric properties of materials at the

Sagan Memorial Station, Mars, *Journal of Geophysical Research*, 104(E4), 8809-8830.

Johnson, J.R., W. Grundy, M. Lemmon, J. Bell, M. Johnson, R. Deen, R. Arvidson, W. Farrand, E. Guinness, A. Hayes, K. Herkenhoff, F. Seelos, J. Soderblom, S. Squyers (2006) Spectrophometric properties of materials observed by Pancam on the Mars Exploration Rovers: 1. Spirit. *Journal of Geophysical Research*, 111, E02S14, doi:10.1029/2005JE002494.

Jouglet, D., F. Poulet, R. E. Milliken, J. F. Mustard, J.-P. Bibring,Y. Langevin, B.Gondet, and C. Gomez (2007), Hydration state of the Martian surface as seen by Mars Express OMEGA: 1. Analysis of the 3 µm hydration feature, *Journal of Geophysical Research*, 112, E08S06, doi:10.1029/2006JE002846.

Kieffer, H.H. and T.N. Titus (2001) TES mapping of Mars' northern seasonal cap. *Icarus* 154: 162-180.

Langevin, Y, J.-P. Bibring, F. Montmessin, F. Forget, M. Vincendon, S. Douté, F. Poulet, and B. Gondet (2007), Observations of the south seasonal cap of Mars during recession in 2004–2006 by the OMEGA visible/near-infrared imaging spectrometer on board Mars Express, *Journal of Geophysical Research*, 112, E08S12, doi:10.1029/2006JE002841.

Milliken, R. E., J. F. Mustard, F. Poulet, D. Jouglet, J.-P. Bibring, B. Gondet, and Y. Langevin (2007), Hydration state of the Martian surface as seen by Mars

Express OMEGA: 2. H_2O content of the surface, *Journal of Geophysical Research*, 112, E08S07, doi:10.1029/2006JE002853.

Moore, H.J. et al., (1987) Physical Properties of the surface materials at the Viking Landing Sites on Mars. USGS Professional Paper 1389.

Murchie, S., et al., (2007), Compact Reconnaissance Imaging Spectrometer for Mars (CRISM) on Mars Reconnaissance Orbiter (MRO), *Journal of Geophysical Research*, 112, E05S03, doi:10.1029/2006JE002682.

Pelkey, S.M, J. Mustard, S. Murchie, R. Clancy, M. Wolff, M. Smith, R. Milliken, J. Bibring, A. Gendrin, F. Poulet, Y. Langevin, B. Gondet (2007), CRISM multispectral summary products: Parameterizing mineral diversity on Mars from reflectance, *Journal of Geophysical Research*, 112, E08S14, doi:10.1029/2006JE002831.

Poulet, F., Y. Langevin, G. Boubin, D. Jouglet, J.-P. Bibring, and B. Gondet, 2008, Spectral variability of the Martian high latitude surfaces, *Geophysical Research Letters,* 35, L20201, doi:10.1029/2008GL035450

Roush, T.L. (1994) Charon: More than water ice? *Icarus* 108: 243-254. doi:10.1006/icar.1994.1059

Seelos, K. D., R. Arvidson, S. Cull, C. Hash, T. Heet, E. Guinness, P. McGuire, R. Morris, S. Murchie, T. Parker, T. Roush, F. Seelos, M. Wolff (2008), Geomorphologic and mineralogic characterization of the northern plains of

Mars at the Phoenix Mission candidate landing sites, *Journal of Geophysical Research*, 113, E00A13, doi:10.1029/2008JE003088.

Smith, M.D. (2002) The Annual Cycle of Water Vapor on Mars as Observed by the Thermal Emission Spectrometer. *Journal of Geophysical Research* 107, doi:10.1029/2001JE001522.

Smith, M.D. (2004) Interannual variability in TES atmospheric observations of Mars during 1999–2003. *Icarus* 167: 148-165.

Smith, P. H., L. Tamppari, R. Arvidson, D. Bass, D. Blaney, W. Boynton, A. Carswell, D. Catling, B. Clark, T. Duck, E. DeJong, D. Fisher, W. Goetz, P. Gunnlaugsson, M. Hecht, V. Hipkin, J. Hoffman, S. Hviid, H. Keller, S. Kounaves, C.F. Lange, M. Lemmon, M. Madsen, M. Malin, M. Markieqicz, J. Marshall, C. McKay, M. Mellon, D. Michaelangeli, D. Ming, R. Morris, N. Renno, W. Pike, U. Staufer, C. Stoker, P. Taylor, J. Whiteway, S. Young, A. Zent (2008) Introduction to special section on the Phoenix Mission: Landing Site Characterization Experiments, Mission Overviews, and Expected Science, *Journal of Geophysical Research*, 113, E00A18, doi:10.1029/2008JE003083.

Smith, P.H., L. K. Tamppari, R. E. Arvidson, D. Bass, D. Blaney, W. V. Boynton, A. Carswell, D. C. Catling, B. C. Clark, T. Duck, E. DeJong, D. Fisher, W. Goetz, H. P. Gunnlaugsson, M. H. Hecht, V. Hipkin, J. Hoffman, S. F. Hviid, H. U. Keller, S. P. Kounaves, C. F. Lange, M. T.

Lemmon, M. B. Madsen, W. J. Markiewicz, J. Marshall, C. P. McKay, M. T. Mellon, D. W. Ming, R. V. Morris, W. T. Pike, N. Renno, U. Staufer, C. Stoker, P. Taylor, J. A. Whiteway, A. P. Zent (2009) Water at the Phoenix Landing Site. *Science* 325: doi:10.1126/science.1172339.

Stamnes, K., Tsay, S.-Chee; Jayaweera, Kolf; Wiscombe, Warren (1988) Numerically stable algorithm for discrete-ordinate-method radiative transfer in multiple-scattering and emitting layered media. *Applied Optics* 27: 2502-2509.

Tamppari, L.K., D. Bass, B. Cantor, I. Daubar, C. Dickinson, D. Fisher, K. Fujii, H.P. Gunnlauggson, T.R. Hudson, D. Kass, A. Kleinbohl, L. Komguem, M.T. Lemmon, M. Mellon, J. Moores, A. Pankine, M. Searls, F. Seelos, M.D. Smith, S. Smrekar, P. Taylor, C. von Holstein-Rathlou, W. Weng, J. Whiteway, M. Wolff (2009) Phoenix and MRO Coordinated Atmospheric Measurements. *Journal of Geophysical Research*, doi:10.1029/2009JE003415.

Warren, S.G. (1984) Optical constants of ice from the ultraviolet to the microwave. *Applied Optics* 23: 1206-1225

Whiteway, J. M., L. Komguem, Cameron Dickinson, C. Cook, M. Illnicki, J. Seabrook, V. Popovici, T. Duck, R. Davy, P. Taylor, J. Pathak, David Fisher, A. Carswell, M. Daly, V. Hipkin, A.Zen, M. Hecht, S. Wood, L. Tamparri, N. Renno, J. Moores, M. Lemmon, F. Daerden, P. Smith (2009)

Mars Water Ice Clouds and Precipitation, *Science*, 325(68). DOI:10.1126/science.1172344.

Wiseman, S., Arvidson, R. E.; Griffes, J. L.; Murchie, S.; Poulet, F.; Crism Science Team (2007) Initial analysis of CRISM data over Meridiani Planum. LPSC XXXVIII: Abstract #1945.

Wiseman, Sandra (2009) Spectral and stratigraphic mapping of hydrated sulfate and phyllosilicate-bearing deposits: Implications for the aqueous history of Sinus Meridiani, Mars. Ph.D. Dissertation, Washington University in St. Louis, St. Louis, Missouri.

Wolff, M. J., and R. T. Clancy (2003), Constraints on the size of Martian aerosols from Thermal Emission Spectrometer observations, *Journal of Geophysical Research*, 108(E9), 5097, doi:10.1029/2003JE002057.

Wolff, M. J.; Clancy, R. T.; Smith, M. D.; Crism Science Team; Marci Science Team (2007) Some studies of Martian aerosol properties using MRO/CRISM and MRO/Marci, *Seventh International Conference on Mars,* Pasadena, California*:* Abstract #3121.

Wolff, M.J, M.D. Smith, R.T. Clancy, R. E. Arvidson, M. Kahre, F. Seelos IV, S. Murchie, H. Savijarvi, and the CRISM Science Team. (2009) Wavelength dependence of dust aerosol single scattering albedo as observed by the Compact Reconnaissance Imaging Spectrometer, *Journal of Geophysical Research*, 114, E00D04, doi:10.1029/2009JE003350.

Chapter 4 - Compositions of subsurface ices at the Mars Phoenix landing site

Geophysical Research Letters, doi:10.1029/2010GL045372, in press.

4.1 Introduction

NASA's Mars Phoenix Lander landed on the northern plains of Mars on 25 May 2008. One of its primary objectives was to characterize the nature of shallow subsurface water ice on Mars, in an ongoing effort to understand the past and current water cycle on the planet [*Smith et al.*, 2009]. The lander was equipped with several instruments capable of characterizing the ice, including a Robotic Arm (RA) to remove overlying soil, a Wet Chemistry Laboratory (WCL) to analyze salt concentrations of the ice and soil, a Thermal and Evolved Gas Analyzer (TEGA) to analyze water concentrations and other chemical species, and a Surface Stereo Imager (SSI) to record multi-spectral observations of ice and other surface features.

Over the course of the 151-sol mission, the lander dug 12 trenches (Figure 4.1) at the landing site [*Arvidson et al.*, 2009]. Eight of these (Dodo-Goldilocks, Upper Cupboard, Ice Man, La Mancha, Pet Donkey, Neverland, Burn Alive 3, and Snow White) exposed subsurface water ice [*Mellon et al.*, 2009].

The subsurface ices fall into two distinct categories: a relatively bright ice found in the Dodo-Goldilocks and Upper Cupboard trenches (called here “Dodo-Goldilocks type ice”) (Figure 4.2a), and a relatively dark ice found in the Snow White, Neverland, Pet Donkey, Ice Man, Burn Alive, and La Mancha trenches (called here “Snow White type ice”) (Figure 4.2b). The two ice types had noticeably different physical properties. The formation of a sublimation lag was rapid in Snow White, relative to Dodo-Goldilocks, perhaps reflecting different soil contents available to form a lag. The Snow White ice was impossible for the RA to scrape because of exposure geometry, and so the material’s hardness cannot be compared to Dodo-Goldilocks [*Arvidson et al.*, 2009; *Shaw et al.*, 2009]. The RA used its backhoe on Dodo-Goldilocks, chipping off several large chunks of ice from the trench, indicating that Dodo-Goldilocks was easily fractured and likely in slab form. The inferred differences in the physical properties of the two types of ice suggest that they may have different formation and/or evolutionary histories, as proposed by *Mellon et al.* [2009]; however, because the RA did not perform the same types of digs on both ices, their physical properties cannot be compared directly.

Several mechanisms have been proposed for the origin of subsurface ice in the Martian northern plains. Based on thermal modeling and ice depth estimates from the Gamma Ray Spectrometer (GRS) aboard Mars Odyssey, *Mellon et al.* [2004]

concluded that, on a regional scale, the subsurface ice is in diffusive equilibrium with water vapor in the atmosphere, suggesting that the subsurface ice must be pore ice that was emplaced by vapor diffusion and condensation. Others have proposed that the subsurface ice may more closely resemble relatively-pure massive ice that was originally emplaced by freezing of a body of surface water (e.g., a lake or ocean; *Carr et al.,* 1990), accumulation and burial of packed snow during periods of high obliquity (e.g., *Mischna et al.,* 2003), or buried glaciers [*Prettyman et al.,* 2004].

One of the most important criteria for distinguishing between these two categories of ice formation (pore ice versus pure massive ice) is the ice:soil ratio of the layer. For massive ice, the ice:soil ratio should be high, assuming that the original ice was contaminated by only small amounts of soil or dust. For pore ice, the ice:soil ratio should be low, the exact ratio being limited by the available pore space within the original soils.

In this study, we use spectra from the SSI instrument to estimate the ice:soil ratio in the two types of subsurface ice observed at the Phoenix landing site. We first model the photometric functions of the two types of ices. We then use a non-linear mixing model to estimate contributions of ice and soil to the SSI spectra. Finally, we estimate the weight percent of soil present in each type of ice, with an eye toward understanding their different formation histories.

4.2 Methods

The SSI is a stereo imager with 12-position filter wheels at 13 unique wavelengths from 0.445 µm to 1.001 µm [*Smith et al.*, 2009].

To estimate the ratio of ice to soil in the two types of ices, we compare SSI spectra to model spectra produced using a non-linear mixing model. The SSI spectra were 5x5 pixel averages chosen to be representative of the ices examined.

The model spectra are calculated as:

$$r(i,e,g) = \frac{w}{4\pi}\frac{\mu_0}{\mu_0+\mu}\{p(g)+H(\mu_0)H(\mu)-1\}K$$

Equation 4.1

where *r(i,e,g)* is the bidirectional reflectance; *i, e,* and *g* are the incidence, emergence, and phase angles, respectively; *w* is the single-scattering albedo, μ_0 is the cosine of *i*, μ is the cosine of *e*, *p(g)* is the surface phase function, $H(\mu_0)$ $H(\mu)$ describe multiple scattering, and *K* describes the porosity of the material [*Hapke* 1993, 2008].

The single-scattering albedos of mixtures of ice and soil were calculated from *Hapke* [1993] as:

$$w = \frac{\sum_{i=1}^{i=n}\left(Q_{Si}M_i/\rho_i D_i\right)}{\sum_{i=1}^{i=n}\left(Q_{Ei}M_i/\rho_i D_i\right)}$$

Equation 4.2

where M_i is the mass fraction of component i, ρ_i the solid density, D_i the grain diameter, Q_{Si} the scattering efficiency, Q_{Ei} the extinction efficiency, and the summation is carried out for all components in the mixture. Two components were considered: soil and water ice. Secondary phases (e.g., perchlorate) might be present, but will only begin to affect spectral signatures at high mass fractions (>10 wt% for perchlorate, *Cull et al.,* 2010b). Because Phoenix detected only small fractions of these (0.4-0.6 wt% for perchlorate, *Hecht et al.*, 2009), we exclude them from our spectral modeling.

The scattering and extinction efficiencies were calculated as described by *Roush* [1994], a procedure which requires optical constants for both components. The soil component utilized optical constants based on a Mauna Kea palagonite sample: a low-temperature alteration product of fine-grained basaltic ash [*Clancy et al.,* 1995]. Based on orbital observations from the Compact Reconnaissance Imaging Spectrometer for Mars, dehydrated palagonite mixed with nanophase iron oxides accurately predicts the grain sizes observed at the Phoenix landing site [*Cull et al.,* 2010a], although it produces a poor fit at lower wavelengths. Optical constants for ice were used from *Warren* [1984]. Solid densities of ρ=0.9167 g/cm^3 and ρ=2.700 g/cm^3 [e.g., *Allen et al.,* 1997] were used for water ice and palagonite, respectively. The soil grain size was assumed to be ~60 micrometers, based on observations from Phoenix’s Optical Microscope [*Goetz et al.,* 2010]. This leaves the spectrum dependent only on the relative amounts of ice and soil in each spectrum, the ice grain size, and the porosity of the material.

Moore et al. [1987] estimated that soils at the Viking landing sites had porosities varying between 25 and 60%. *Zent et al*. [2010] estimated a porosity for Phoenix surface soils between 50 and 55%, based on heat capacity measurements. For the sake of modeling, we restrict porosities of Phoenix materials to 25 to 60%; however, we find that porosity has a negligible effect on our mixtures.

To estimate the ice grain size parameter, we ran two types of models: one assuming the ice was in massive form, and one assuming pore ice. For pore ice, the ice grain sizes were assumed to be no larger than the pore space within the soil. For massive ice, "grain size" is actually representing path length through a single ice crystal before being refracted at the crystal boundary, and was defined as being between 0.1 μm and 1 cm: the lower and upper limits expected for subsurface ice.

The surface phase function was modeled as a single-lobed Henyey-Greenstein model [*Henyey and Greenstein* 1941]:

$$p(g) = \frac{(1-\delta^2)}{(1+2\delta\cos(g)+\delta^2)^{3/2}}$$

Equation 4.3

where δ is an asymmetry factor constrained to be between -1 and 1 (δ=0 for isotropic scatter). The asymmetry factor for Snow White ice was calculated using multiple observations of ices exposed less than two hours previously, taken at varying phase angles (Figure 4.3). The brightness of each observation at 1.001 µm (a relatively noise-free band) was plotted against phase angle and fit to model results of varying δ values. The asymmetry factor could not be found for Dodo-Goldilocks, because it lacked a wide enough range of phase angle observations.

4.3 Results

Because the asymmetry factor (δ) for the Dodo-Goldilocks ice could not be determined, the model contained too many unconstrained parameters, and an exact ice:soil ratio could not be determined. However, because Dodo-Goldilocks ices have a strong water ice-induced slopeat 1.001 µm, modeling can be used to estimate the ice:soil ratio (Figure 4.4a). The modeling shows that soil dominates the spectrum at all wavelengths, and even a small amount of soil mixed with ice is capable of masking the water ice signature. Any ice-soil mixture with >1 wt% soil masks the 1.001 µm absorption; hence, Dodo-Goldilocks must be at least 99 wt% pure water ice.

The δ factor was calculated for the Snow White type ice (Figure 4.3). The scattering behavior was best fit by δ=0.15, a moderately forward-scattering material. Of the two types of models run – pore ice vs. massive ice – the Snow White ice was poorly fit by massive ice and well fit by pore ice (Figure 4.4b). Massive ice, with its higher ice:soil ratio and larger ice grain sizes, produced a spectrum that was too bright to fit the Snow White ice.

Because soil dominates the spectrum in this wavelength region, an exact ice:soil ratio could not be obtained for the Snow White ices. However, by matching the overall albedo of the spectrum, we were able to place an upper limit on the ice fraction in the material. The Snow White ice spectrum albedo was best fit by a model that included ~30 ± 20 wt% ice, as shown in Figure 4.4b. Albedo at 0.445 µm is not well fit by this model; however, this poor fit was expected because the analog we use for soil does not perfectly fit Phoenix soils at very short wavelengths [*Cull et al.*, 2010a].

4.4 Discussion

Although modeling was unable to produce exact ice:soil ratios, it has constrained the ice fraction in both the Dodo-Goldilocks and Snow White types of ice. Because the 1.001 µm slope is not masked in Dodo-Goldilocks ices, Dodo-Goldilocks must be at least 99wt% pure water ice. The Snow White ices are estimated to have <50 wt% ice, with a best fit of ~30 ± 20 wt% ice. These estimates are consistent with other Phoenix observations: ~30 wt% ice is ~55 vol.% ice , which is consistent with Thermal and Electrical Conductivity Probe (TECP) estimates of 50-55% porosity for average ice-free soils derived from measured heat capacity [*Hudson* *et al*., 2009; *Zent et al.,* 2010]. If ice were to diffuse into this soil, filling the pore space, it would represent ~50-55 vol.% of the mixture.

These results have important implications for our understanding of subsurface ice at the Phoenix landing site. It is likely that the two ices were emplaced via different mechanisms. The pore ice observed in Snow White is probably the result of vapor diffusion through the overlying soil layer and condensation of pore ice in the cold soil subsurface, as proposed by *Mellon et al.* [2004]. This type of ice is the dominate form, found at 90% of trenched ice exposures [*Mellon et al.,* 2009]. The relatively-pure, light-toned ice typified at Dodo-Goldilocks, on the other hand, represents a concentrated deposition of ice. This light-toned ice may have formed from a buried surface ice, such as snow; however, supraposed decimeter-scale surface rocks argue for an in-situ formation mechanism, such as ice lenses or needle ice (see *Mellon et al.,* 2009 for a detailed discussion). It is likely that an in-situ formation would involve the migration of thin films of adsorbed water, a phenomenon that appears to be active at the Phoenix landing site, based on concentrated patches of perchlorate salts [*Cull et al.,* 2010b].

Our spectral analysis supports the contention that these two ice deposits exhibit distinct concentrations and formed by different mechanisms. The presence of these two types of ice within the relatively small sample space of the Phoenix lander implies that both emplacement mechanisms are common throughout the northern plains. Moreover, the lack of gradation between the two types of ices suggests two different periods of emplacement.

4.5 Conclusions

We conclude that the two types of ices exposed at the Mars Phoenix landing site are both physically and compositionally distinct. The Snow White type ice is best modeled as ~55 vol.% ice, indicating that it is probably pore ice trapped between grains of soil. The Dodo-Goldilocks ice, on the other hand, is >99% pure water ice, with only a small amount of dust present. These two distinctly different compositions point to different formation mechanisms and/or subsequent evolutions of these two ices.

Figures

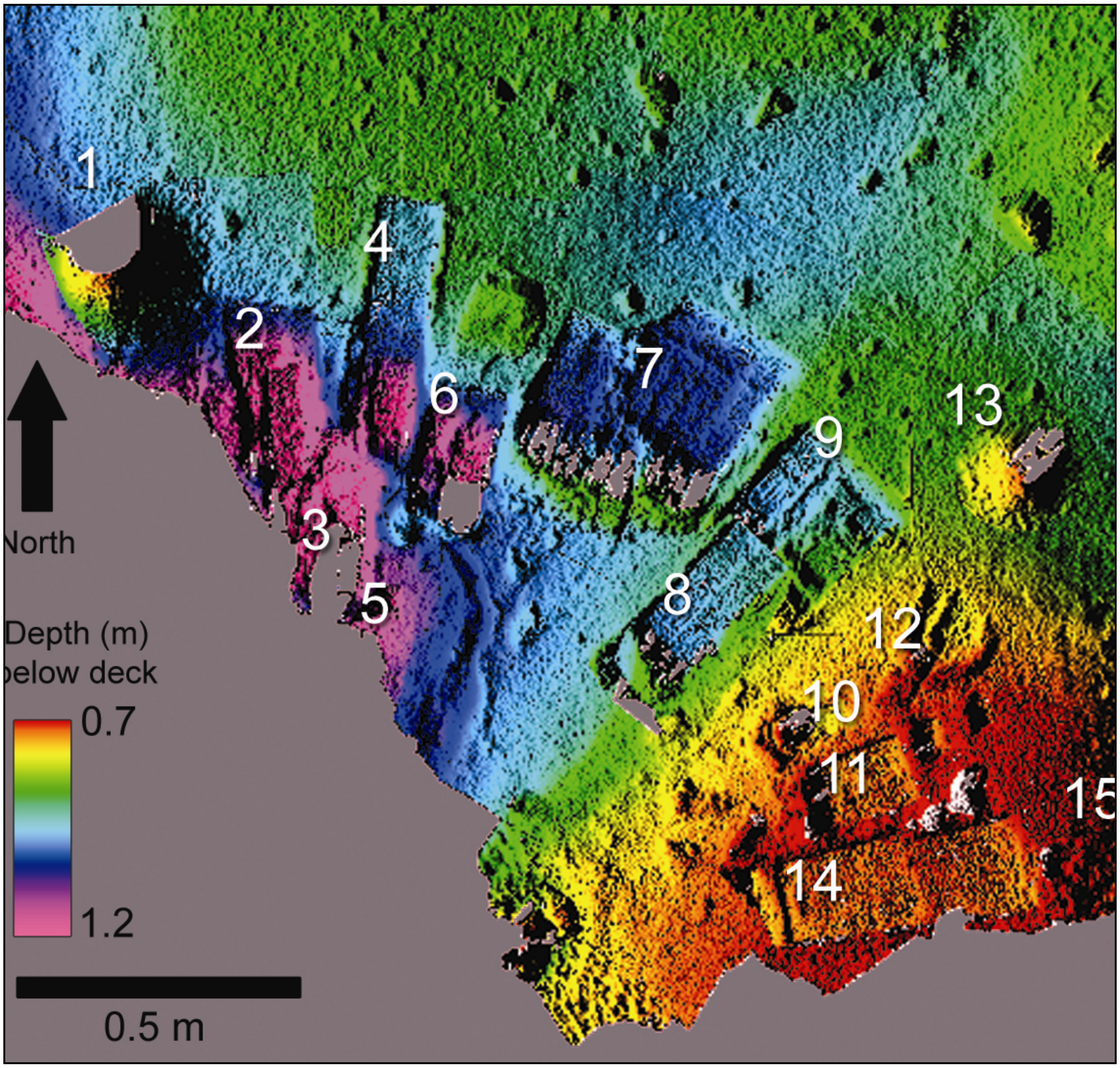

Figure 4.1 - The workspace at the Phoenix landing site.

The lander excavated 12 trenches and produced three dump piles along its northeast side (right): Caterpillar Dump Pile (1), Dodo-Goldilocks trench (2), Stone Soup trench (3), Upper Cupboard trench (4), Lower Cupboard trench (5), Ice Man trench (6), La Mancha trench (7), Neverland trench (8), Pet Donkey trench (9), Bear’s Lodge trench (10), Burn Alive 3 trench (11), Runaway trench (12), Bee Tree dump pile (13), Snow White trench (14), and Croquet Ground dump pile (15).

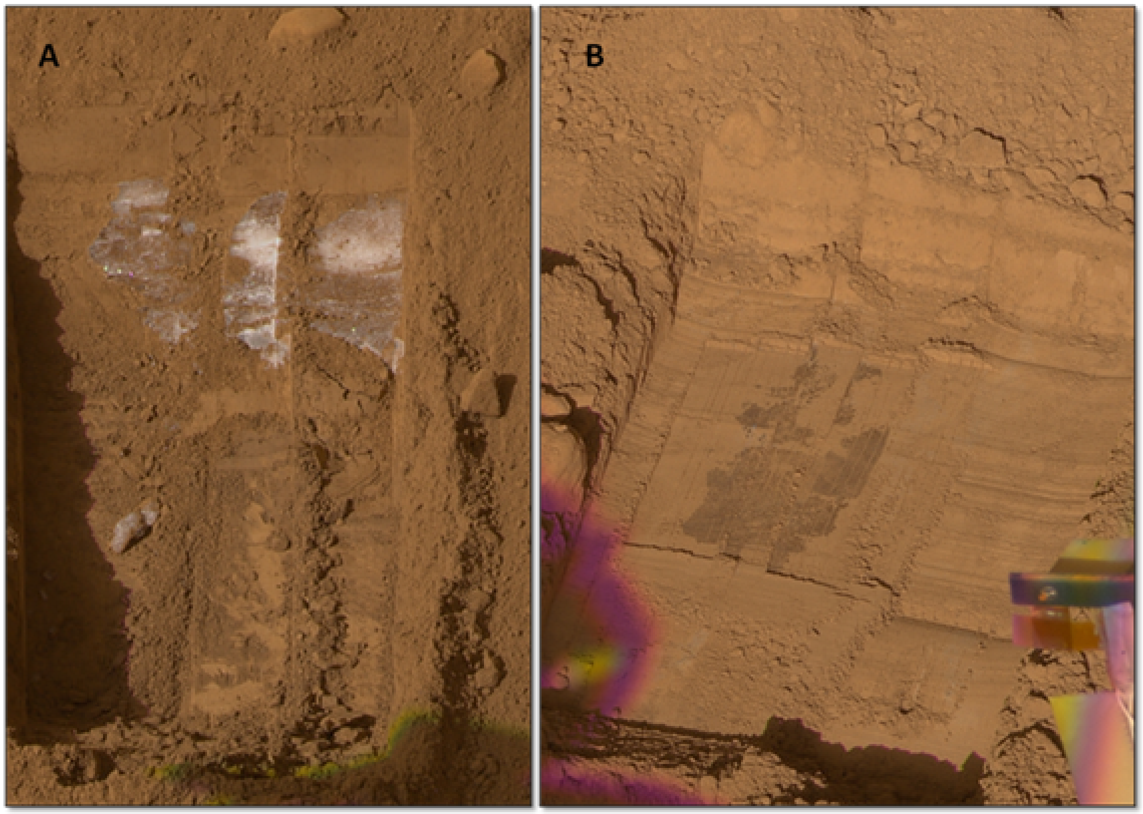

Figure 4.2 – Types of subsurface ice at the Phoenix landing site.

A) The Dodo-Goldilocks trench at the Phoenix landing site. The white material in the trench is water ice, confirmed by SSI spectra. B) The Snow White trench. The dark material in the trench bottom is water ice, confirmed by TEGA analysis.

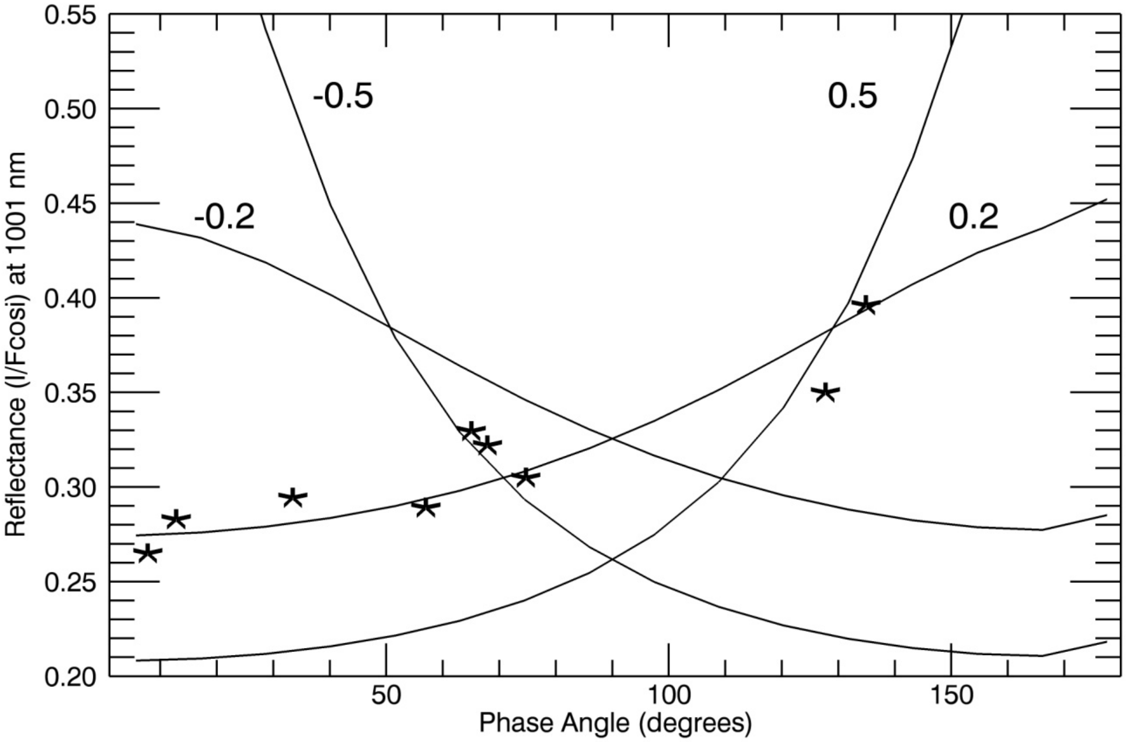

Figure 4.3 – Scattering behavior of Snow White ice.

Comparing scattering behavior at the Snow White trench (stars) to calculated phase functions from Equation 2 (lines). The Snow White ice is clearly forward-scattering, with a best-fit asymmetry parameter of ~0.15.

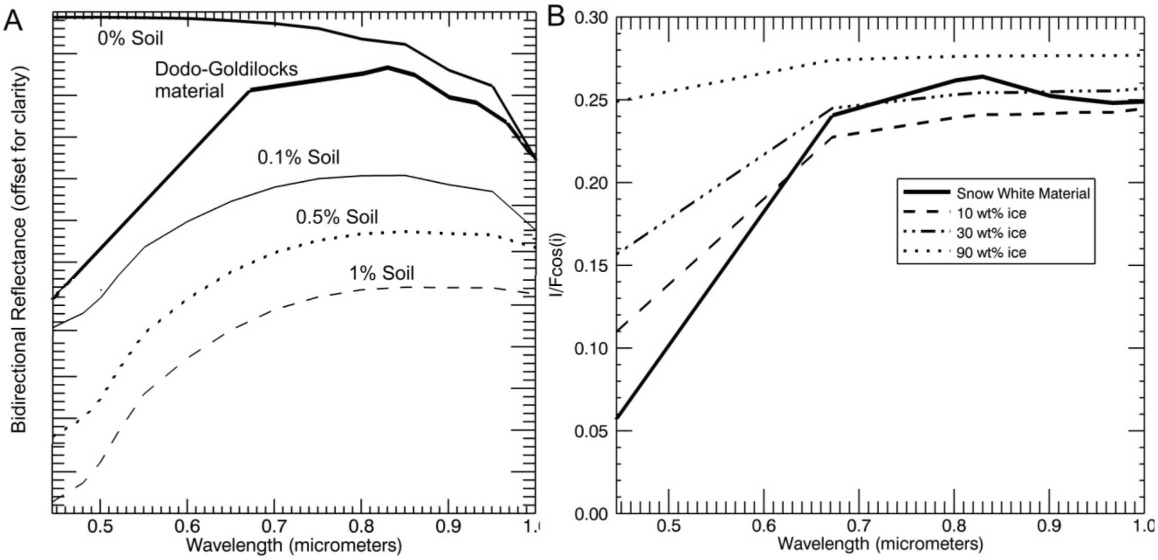

Figure 4.4 – The 1001 nm band depth.

A) Comparing 1.001 µm band depths in various model results. Any composition with >1 wt% soil masks the 1.001 µm absorption, illustrating that Dodo-Goldilocks must be at least 99wt% pure water ice. B) Freshly exposed (<2 hours old) ice at the Snow White trench (thick line) vs. model results of ice-soil mixtures. The shorter wavelengths do not fit the observed spectrum; however, this is expected due to the soil analog used in the model. The overall albedo and shape of the longer wavelengths is the basis for interpretation.

References

Arvidson, R.E., R. Bonitz, M. Robinson, J. Carsten, R. Volpe, A. Trebi-Ollennu, M. Mellon, P. Chu, K. Davis, J. Wilson, A. Shaw, R. Greenberger, K. Siebach, T. Stein, S. Cull, W. Goetz, R. Morris, D. Ming, H. Keller, M. Lemmon, H. Sizemore, M. Mehta (2009), Results from the Mars Phoenix Lander Robotic Arm experiment, *Journal of Geophysical Research*, 114, E00E02, doi:10.1029/2009JE003408.

Byrne, S., Colin M. Dundas, Megan R. Kennedy, Michael T. Mellon, Alfred S. McEwen, Selby C. Cull, Ingrid J. Daubar, David E. Shean, Kimberly D. Seelos, Scott L. Murchie, Bruce A. Cantor, Raymond E. Arvidson, Kenneth S. Edgett, Andreas Reufer, Nicolas Thomas, Tanya N. Harrison, Liliya V. Posiolova, Frank P. Seelos (2009) Distribution of mid-latitude ground-ice on Mars from new impact craters. *Science*, 325(5948): 1674-1676. doi: 10.1126/science.1175307

Carr, M. (1990) D/H on Mars: Effects of floods, volcanism, impacts, and polar processes. *Icarus* 87: 210-227.

Clancy, R. T., S. W. Lee, G. R. Gladstone, W. W. McMillan, and T. Rousch (1995), A new model for Mars atmospheric dust based upon analysis of ultraviolet through infrared observations from Mariner 9, Viking, and Phobos, *Journal of Geophysical Research*, 100(E3), 5251–5263.

Hapke, B. (1993) Theory of reflectance and emittance spectroscopy. Cambridge University Press: Cambridge, UK.

Hapke, B. (2008) Bidirectional reflectance spectroscopy: 6. Effects of porosity. Icarus 195: 918-926.

Heet, T,. R. E. Arvidson, S. C. Cull, M. T. Mellon, and K. D. Seelos (2009) Geomorphic and geologic settings of the Phoenix lander mission landing site. *Journal of Geophysical Research*, 114, E00E04, doi:10.1029/2009JE003416, 2009.

Henyey, L.G. and J.L. Greenstein (1941) Diffuse radiation in the galaxy, *Astrophysical Journal* 93:70-83, 1941.

Mellon, M., W. Feldman, T. Prettyman (2004) The presence and stability of ground ice in the southern hemisphere of Mars. *Icarus* 169: 324-340. doi:10.1016/j.icarus.2003.10.022

Mischna, M., M. Richardson, J. Wilson, and D. McCleese (2003) On the orbital forcing of Martian water and CO2 cycles: A general circulation model study with simplified volatile schemes. *Journal of Geophysical Research,* 208: 1-25.

Pike, W.T., H. Sykulska, S. Vigendran, and the Phoenix Microscopy Team (2009) Fractal analysis of the microstructure of the martian soil at the Phoenix landing site. LPSC XL, Abstract #1909.

Prettyman, T.H., W. Feldman, M. Mellon, F. McKinney, W. Boynton, S. Karunatillake, D. Lawrence, S. Maurice, J. Murphy, S. Squyers, R. Starr, R. Tokar (2004) Composition and structure of the Martian surface in the high southern latitudes from neutron spectroscopy. *Journal of Geophysical Research,* 109: E05001.

Roush, T.L. (1994) Charon: More than water ice? *Icarus* 108: 243-254. doi:10.1006/icar.1994.1059

Shaw, A., R. Arvidson, R. Bonitz, J. Carsten, H. Keller, M. Lemmon, M Mellon, M. Robinson, A. Trebi-Ollennu (2009) Phoenix soil physical properties investigation. *Journal of Geophysical Research*, 114, doi:10.1029/2009JE003455, 2009

Smith, P.H., L. K. Tamppari, R. E. Arvidson, D. Bass, D. Blaney, W. V. Boynton, A. Carswell, D. C. Catling, B. C. Clark, T. Duck, E. DeJong, D. Fisher, W. Goetz, H. P. Gunnlaugsson, M. H. Hecht, V. Hipkin, J. Hoffman, S. F. Hviid, H. U. Keller, S. P. Kounaves, C. F. Lange, M. T. Lemmon, M. B. Madsen, W. J. Markiewicz, J. Marshall, C. P. McKay, M. T. Mellon, D. W. Ming, R. V. Morris, W. T. Pike, N. Renno, U. Staufer, C. Stoker, P. Taylor, J. A. Whiteway, A. P. Zent (2009) Water at the Phoenix Landing Site. *Science* 325: doi:10.1126/science.1172339.

Chapter 5 - Concentrated perchlorate at the Mars Phoenix landing site: Evidence for thin film liquid water on Mars

Geophysical Research Letters, doi:10.1029/2010GL045269, in press. © Copyright 2010 by the American Geophysical Union.

5.1 Introduction

One of the primary goals of NASA's Phoenix mission, which landed on the northern plains of Mars on 25 May 2008, was to characterize the past and present water-ice cycle on Mars, including the concentrations of salt species in the soil [*Smith et al.,* 2009]. To search for soluble salts, three soil samples were added to Phoenix's Wet Chemistry Laboratory (WCL; *Kounaves et al.,* 2009),, which registered a strong signal that was interpreted as resulting from perchlorate [*Hecht et al.,* 2009]. Because perchlorates are strongly deliquescent salts, their homogeneous distribution through the soil column was cited as evidence that the Phoenix soils have not interacted extensively with liquid water [*Hecht et al.,* 2009].

In this paper, we use data from Phoenix's Surface Stereo Imager (SSI) to map the perchlorate distribution at the Phoenix landing site. Because several minerals are spectrally similar to perchlorate (including bischofite and some zeolite and phyllosilicate minerals), we also use a geochemical model to assess the stability of these minerals under conditions at the Phoenix landing site.

5.2 Methods

5.2.1 Spectral Mapping

Phoenix's SSI instrument acquired images and spectra (0.445 to 1.001 μm) of the landing site (68.2188N, 234.2508E, IAU 2000 areocentric), including the 12 trenches that Phoenix excavated using its Robotic Arm (RA, Figure 5.1, *Arvidson et al.,* 2009). With SSI, we examined soil features in each of the 12 trenches and compared them to undisturbed surface soils.

For identification purposes, a perchlorate spectrum was obtained with an ASD spectrometer in a Mars-like chamber filled with a dry N_2 atmosphere (0.4% relative humidity, 100 ppmv H_2O, T~23C) after purging dry N2 for 1176 hours. The perchlorate sample was tested with powder XRD and confirmed to be $Mg(ClO_4).6H_2O$.

5.2.2 Geochemical Modeling

Because zeolite minerals are spectrally similar to perchlorate, a model was created to evaluate the plausibility of zeolite formation at the Phoenix landing site. In this model, a fluid of the composition reported by the WCL measurements that was in equilibrium with calcite [*Boyton et al.,* 2009] at a partial pressure of CO_2 of 5.7 mbar

[*Tamppari et al.,* 2008] and contained an estimated sulfate content for charge balance was reacted with equal amounts of hematite and mineral components of basaltic sand [*McSween et al.,* 2006]. This assemblage was chosen to approximate the chemical environment present at the Phoenix lander site.

All calculations were performed using The Geochemist's Workbench® [*Bethke et al.,* 2009]. The Lawrence Livermore National Laboratory thermochemical database [*Delaney and Lundeen* 1990] was employed with an extended Debye-Huckel activity correction model that is parameterized to be accurate in up to 3 m NaCl solution and approximately 0.5-1 m ionic strengths of other electrolytes [*Helgeson* 1969; *Helgeson et al.,* 1974a, 1974b]. All calculations were performed at 25˚C as the database lacked thermodynamic data for zeolites at other temperatures. Chabazite was not included in the database and was thus not considered in the calculations.

5.3 Results

5.3.1 Spectral Mapping Results

We identified small, relatively high albedo soil patches (Figure 5.2) with unique spectral properties in material excavated during generation of six trenches: Dodo-Goldilocks, Upper Cupboard, Snow White, Ice Man, Neverland, and Stone

Soup. SSI spectra of the patches have a steep positive slope between 0.445 and 0.65 µm, typical of the "red edge" resulting from nanophase iron oxide materials [*Morris et al.,* 2006]. Unlike other Phoenix soils, which are featureless and relatively flat from 0.65 to 1.001 µm, the spectra of these patches also have a pronounced minimum reflectance at 0.967 µm (Figure 5.3).

The patches with the 0.967 µm feature are each several millimeters across and appear as distinct surface patches on soil clods and exposed trench floors. The clods are subangular fragments that keep their form under Mars surface conditions over the Phoenix mission timescale. The patches on trench floors occur as rounded lumps, morphologically similar to smoothed trench floor soil. The patches are found only in areas of disturbed soil (trenches and dump piles); none are observed on undisturbed surface soil, and none are found in contact with ice.

Spectra of soils with the 0.967 µm feature did not change through time. Each patch was uncovered during an RA excavation, exposed for two or more sols, and in some cases re-buried by new trenching. One patch was left undisturbed for 113 sols, during which no changes were observed to the shape of its spectrum, its overall albedo, or the depth of the 0.967 µm feature. In addition, the size and shape of the clods did not change. Thus, the patches are stable on the surface on timescales of hundreds of sols.

The feature is interpreted as an absorption feature due to the third overtone of the asymmetric OH stretch, which can result from either bound water or OH within the mineral structure [*Roush et al.*, 1997].

5.3.2 Geochemical Modeling Results

Zeolites with potential spectral matches to the 0.967 µm feature include heulandite, chabazite, laumontite, mesolite, natrolite, scolecite, and stilbite [*Crowley* 1991]. Of these, only heulandite, chabazite, laumontite, and natrolite are reported to form under low-temperature conditions consistent with pedogenic formation at the Phoenix lander site [*Passaglia and Sheppard* 2001; *Ming and Boettinger* 2001]. Zeolite crust formation would require aqueous pedogenic processes, with weathering of basaltic sand material originating as dust providing the main chemical components required for zeolite formation.

Our geochemical modeling demonstrates that this reaction will not produce any of the plausible zeolite phases. All zeolites that potentially match the feature are thermodynamically unstable in this system (Figure 5.4A). Mesolite is the most likely zeolite to form under Phoenix conditions; however, this phase has not been reported to occur or form in any soil or sedimentary environments on Earth [*Ming and Boettinger* 2001; *Hay and Sheppard* 2001], suggesting that formation of this phase under non-hydrothermal conditions is inhibited. Our modelling shows that smectites (Fe/Mg saponite and nontronite) and minor gibbsite are the most thermodynamically stable weathering products at the Phoenix site (Figure 5.4B). Gibbsite is likely a proxy for Al incorporation into the predicted smectites, which is not well accounted for in the thermodynamic model as data is only available for smectites of fixed end-member composition.

5.4 Discussion

5.4.1 Patch Spectral Properties

The high-albedo patches all have pronounced absorptions at 0.967 µm. The 0.967 µm filter is prone to artifacts, because it was the final filter taken during the sequence of images, and illumination conditions can change. However, we have used several criteria to rule out the possibility of artifacts. First, the pixels are clumped together, not randomly distributed across an image. Second, they are not located in or near shadows. Third, they were observed repeatedly and have the same feature on multiple sols (up to 113 sols). Fourth, these pixels have the same feature in images taken at multiple phase angles (Figure 5.3), ruling out the possibility of a viewing geometry artifact. Fifth, each image had a slightly different pointing, so the pixels in question are not confined to specific parts of the detector.

We conclude that the 0.967 µm feature is not an artifact, but rather is caused by a material exposed during RA operations. Additionally, because the feature is found only as patches on the clods, we conclude that the material is a surface coating or crust.

5.4.2 Patch Spectral Candidates

Water ice, which is also observed in trenches, has absorptions at 0.98 and 1.04 µm, which cause a negative slope from 0.85 to 1.001 µm. Water ice is a poor spectral fit to spectra of the patches described here, thus is an unlikely candidate. Additionally, the long-term stability of these patches rules out water ice, which was observed to sublimate in a matter of hours to sols when exposed at the surface [*Smith et al.,* 2009].

Several minerals (e.g., Figure 5.3C) produce a 0.967 µm feature, including hydrated Mg- and Ca-perchlorates, some zeolite and phyllosilicate minerals, and at least one hydrated chloride mineral (bischofite, *Crowley et al.,* 1991). WCL could detect and measure Cl ions, and did not detect bischofite [*Kounaves et al.,* 2010]. Our geochemical modeling indicates that zeolites are unlikely candidates for the patches described here, because they are unlikely to form under Phoenix site conditions (see Section 3.1 above). Zeolite formation generally requires an aqueous environment with pH > 9 [*Hay and Sheppard* 2001], and though the Phoenix landing site may have experienced aqueous activity in its past [*Smith et al.,* 2009], the 7.7 pH of the soil appears to be buffered by calcite [*Boyton et al.,* 2009], making a highly alkaline aqueous environment unlikely.

In one soil sample, Phoenix's Thermal and Evolved Gas Analyzer (TEGA) recorded a very small H_2O release between 700 and 800˚C that was interpreted as possible evidence of a phyllosilicate mineral (possibly smectites, *Boyton et al.,* 2008). However, material discussed here is present only in concentrated subsurface patches, indicating that some mechanism is translocating them down in the soil column, and concentrating them into patches. Phyllosilicate minerals have a very low solubility and would not be expected to be redistributed by dissolution and reprecipitation in water. Aqueous clay illuviation can physically move phyllosilicates from the surface to subsurface, forming argillic horizons or clay coatings on peds; however, this process requires repeated flushings with a substantial quantity of water [e.g., *Eswaran and Sys* 1979]. Additionally, Phoenix soils undergo pedoturbation resulting from seasonal freeze-thaw cycles [*Mellon et al.,* 2008]; hence, the high-volume wetting events would have had to occurred recently in order for the argillic horizons to remain intact. We see no evidence to suggest that the Phoenix landing site has been repeatedly flushed with large volumes of liquid water in the geologically recent past, and so conclude that physically translocated phyllosilicates are unlikely candidates for the patches reported here.

Additionally, our geochemical modeling suggests that the stable phyllosilicates would all contain substantial iron because of their formation from basaltic material, and they would display a green or brown color, which is inconsistent with the observed crust. Their original formation would also require substantial aqueous alteration of basaltic sand; corroborating evidence for such alteration at the site is lacking.

Perchlorate, on the other hand, is highly soluble in even very small amounts of water, and would be easily transported from the surface to the subsurface by fluids. In the subsurface, it would form concentrated crusts as the water evaporated or froze then sublimated. Given the previous WCL detection of perchlorate at the site, the thermodynamic instability of zeolites, the concentrated morphology of the observed patches, and their location in the soil column, we conclude that a hydrated perchlorate salt is the most likely candidate to explain the 0.967 µm absorption feature.

5.4.3 Perchlorate at the Phoenix Landing Site

The observation that concentrated perchlorate patches are limited to the subsurface is not inconsistent with previous findings from the Phoenix WCL, which reported perchlorate throughout the soil column, including a sample from near the surface (actually a scoop sample of the upper ~1 cm of soil) [*Hecht et al.,* 2009]. Taken together, the WCL and SSI observations indicate that the soil column contains low concentrations of evenly dispersed perchlorate, with occasional patches of the highly concentrated perchlorate reported here.

These observations have constrained the cation associated with the perchlorate: only Mg- and Ca-perchlorate produce a 0.967 µm feature, while K-, Na-, Fe^{3+}, and Fe^{2+}-perchlorates do not. Interestingly, Mg- and Ca-perchlorates have significantly lower eutectic temperatures, increasing the chances to brine formation [

Chevrier et al., 2009]. This work does not rule out the possibility of additional perchlorate phases at the Phoenix site.

Previous studies have proposed that perchlorate on Mars might form from atmospheric interactions between ozone and volatile chlorine compounds as aerosols or at the surface, as in the Atacama Desert of Chile [*Catling et al.,* 2010] and the Antarctic Dry Valleys [*Kounaves et al.,* 2010]. Dissolution and redistribution of perchlorate could occur when summer mid-day temperatures exceed the perchlorate eutectic point. *Chevrier et al.*, [2009] showed that Mg-perchlorate is metastable above 206K, while Phoenix surface temperatures rose up to 245K during the mission. However, the volume of water in the atmosphere during these times is small: the maximum observed water vapor in the atmospheric column was ~55 precipitable- μm [*Tamppari et al.,* 2009]. An alternative redistribution mechanism involves seasonal ices. The Phoenix site is covered in early fall by an ~90 micrometer layer of seasonal H_2O ice, which is then topped in winter by a translucent slab of CO_2 ice that reaches ~30 cm thick [*Cull et al.*, 2010]. At the base of the translucent CO_2 slab, a solid greenhouse effect can increase the temperature at the ice-surface interface, a process that *Kieffer et al.,* [2000] proposed could be responsible for southern hemisphere "spider" features. We propose that this solid greenhouse effect can raise temperatures at the ice-surface interface high enough for small amounts of meltwater or thin water films to form, dissolving surface perchlorate and transporting it downward through diffusive or gravity-driven fluid transport. Transport into the soil is limited by the rate of transport and the lower boundary of the subsurface ice table. This surface-to-subsurface redistribution process is common in the Antarctic Dry Valleys, where it concentrates soluble sulfates beneath soil clods and rocks. Perchlorate is thus removed from the surface and deposited as salt crusts in the shallow subsurface soil by thin films of water (greater volumes of liquid water are unlikely given the small amount of seasonal water ice involved and the low relative humidity/partial pressure of water in the atmosphere). This scenario implies a geologically recent occurrence of aqueous processes at the site.

Figures

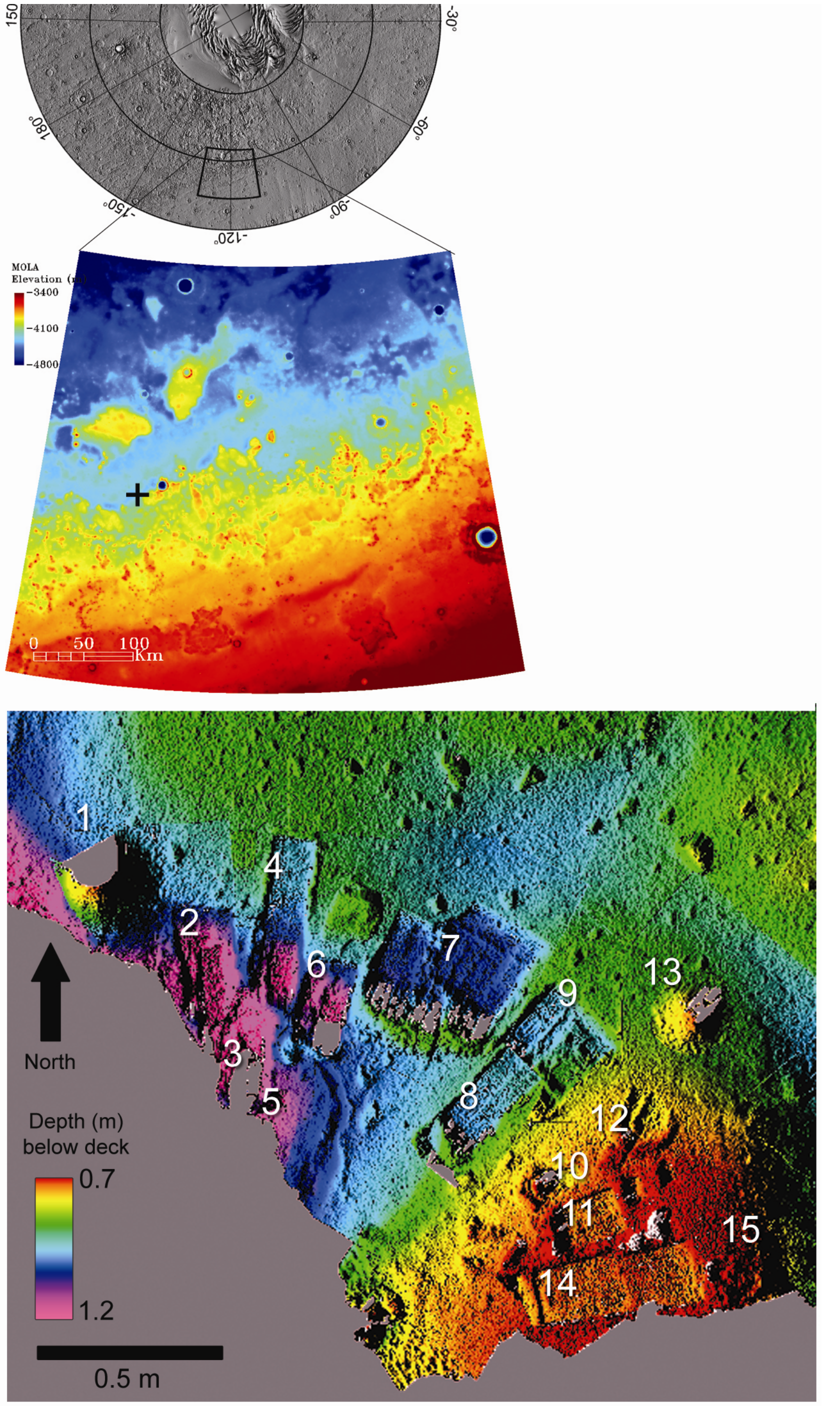
150
-30°
180°
-60°
-150°
-90°
-120°
MOLA
Elevation (m)
-3400
-4100
-4800
0
50
100
Km
1
2
3
4
5
6
7
8
9
10
11
12
13
14
15
North
Depth (m)
below deck
0.7
1.2
0.5 m

Figure 5.1 - Global, regional, and local context.

Phoenix landing site marked by + on lower left. The lander excavated 12 trenches and produced three dump piles along its northeast side (right): Caterpillar Dump (1), Dodo-Goldilocks (2), Stone Soup (3), Upper Cupboard (4), Lower Cupboard (5), Ice Man (6), La Mancha (7), Neverland (8), Pet Donkey (9), Bear’s Lodge (10), Burn Alive 3 (11), Runaway (12), Bee Tree Dump (13), Snow White (14), and Croquet Ground Dump (15).

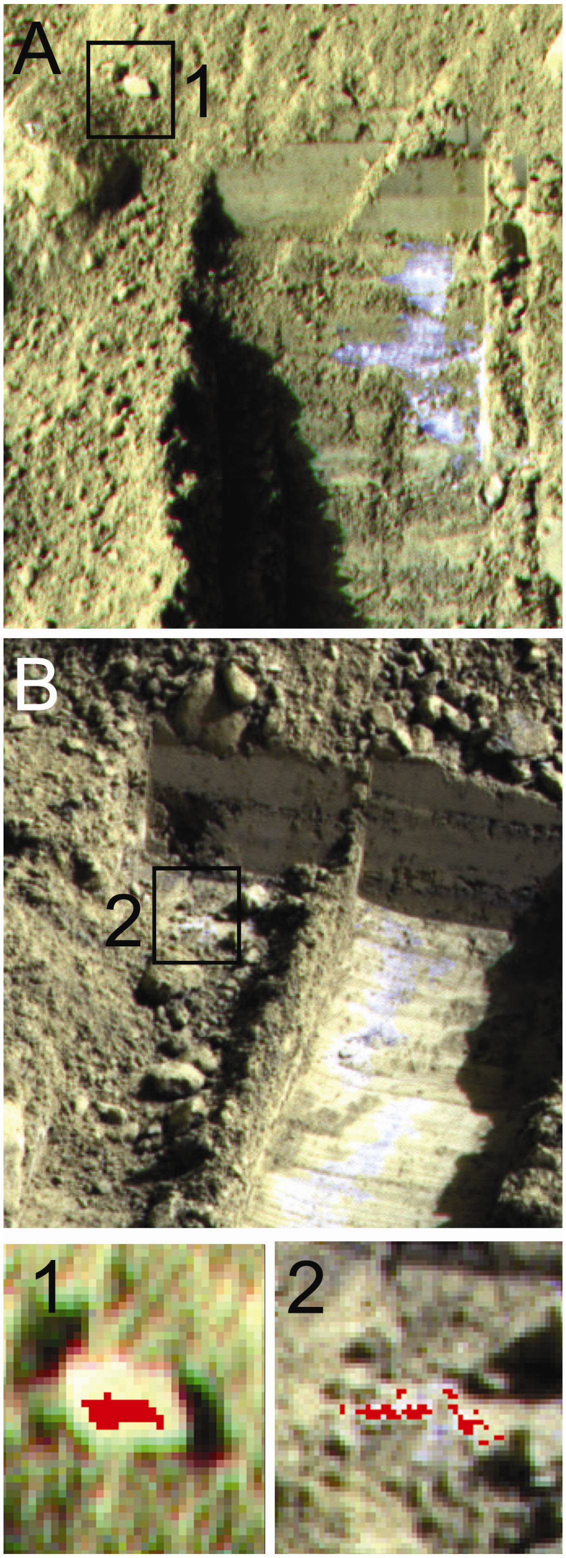
A
1
B
2
1
2

Figure 5.2 - Examples of patches that display the 0.967 µm absorption

Two examples of patches that display the 0.967 µm feature. A) A clod (inset 1, pixels with feature marked in red) at Dodo-Goldilocks (sol 18, image token 125C) does not appear in images taken on before the sol 18 excavation. We conclude that the clod was either dropped by the RA on its way to the Caterpillar Dump (left and below the image), or rolled off the dump pile after dumping. B) A patch at Snow White (sol 16, image token 1314) appeared after the sol 24 excavation (inset 2, pixels with features marked in red). This patch is close to, but does not appear to be in contact with, the Snow White ice.

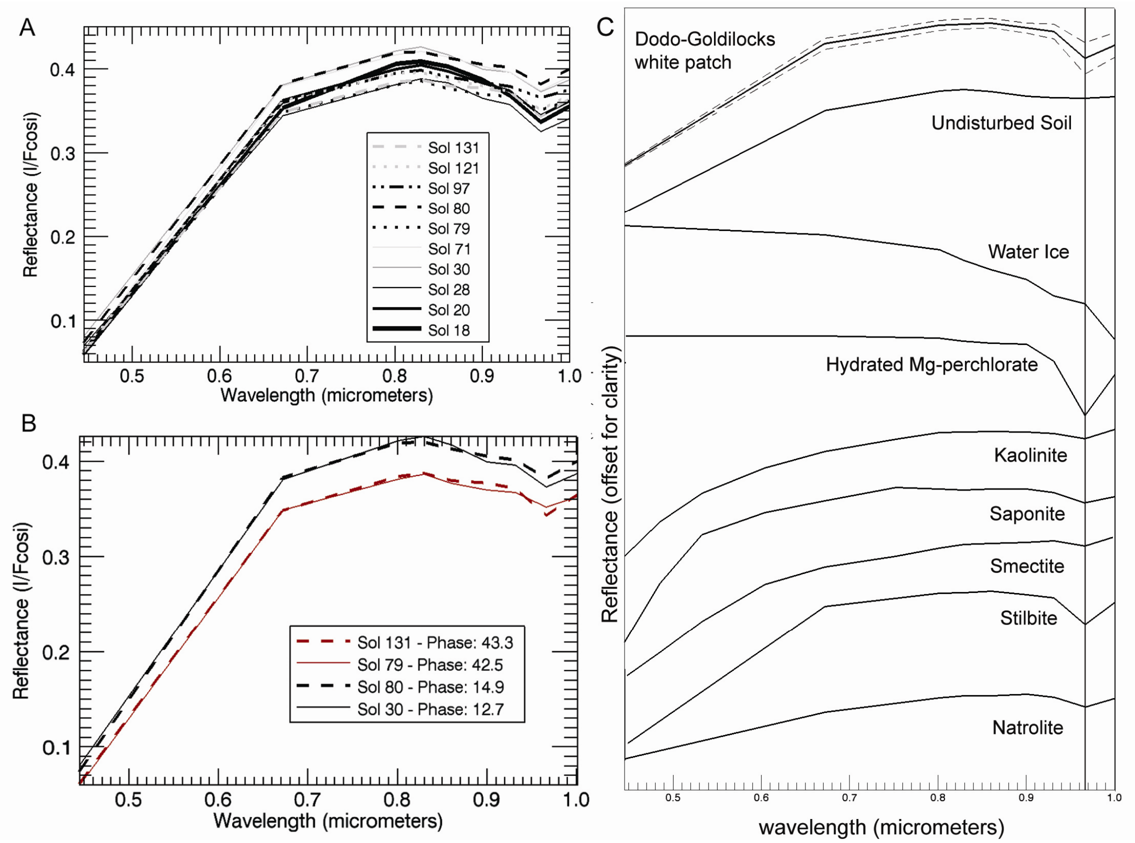

Figure 5.3 – Patch spectra.

A) Spectra of the clod pictured in Figure 2A, taken over 113 sols. The feature at 0.967 μm does not appear to change during that time. The brightness of the spectrum does vary through time; however, this is clearly due to differences in viewing geometry (B). Each of these spectra is generated from averaging together the same group of approximately 30 pixels. The standard deviation for this group of pixels is shown in Figure 3 and is approximately +/- 0.017. C. C) Spectra of candidate minerals for the 0.967 µm feature. A representative patch from Dodo-Goldilocks is shown on top, with the dotted lines illustrating the standard deviation of patch spectra.

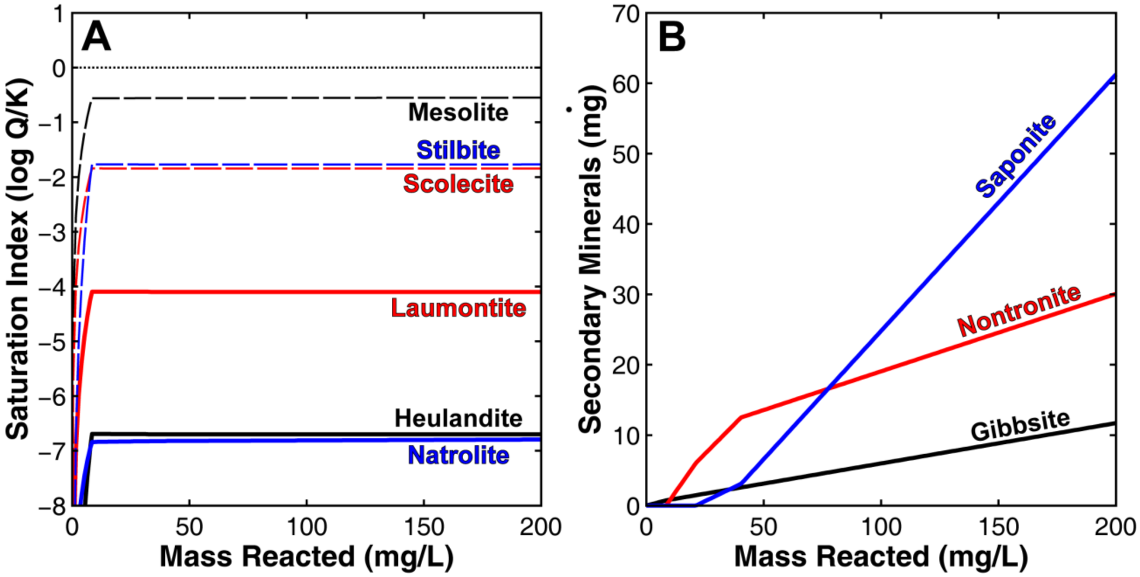

Figure 5.4 – Geochemical modeling results.

Zeolite mineral saturation indices (A) and mass of secondary minerals produced (B) as a function of the mass of a 1:1 mixture of hematite and basaltic sand reacted with a fluid phase representative of the site. K is the equilibrium constant for the reaction, Q is the reaction quotient, and the mineral saturated in the system when K=Q. None of the minerals shown here is saturated in the system.

References

Arvidson, R.E., R. Bonitz, M. Robinson, J. Carsten, R. Volpe, A. Trebi-Ollennu, M. Mellon, P. Chu, K. Davis, J. Wilson, A. Shaw, R. Greenberger, K. Siebach, T. Stein, S. Cull, W. Goetz, R. Morris, D. Ming, H. Keller, M. Lemmon, H. Sizemore, M. Mehta (2009), Results from the Mars Phoenix Lander Robotic Arm experiment, *Journal of Geophysical Research*, 114, E00E02, doi:10.1029/2009JE003408.

Bethke, C. M. (2009) The Geochemist's Workbench Release 8.0. Hydrogeology Program, University of Illinois, Urbana, IL.

Boynton, W. V., Ming, D. W.; Arvidson, R. E.; Blaney, D.; Kounaves, S.; Mellon, M.; Morris, R. V.; Pike, W. T.; Smith, P.; Team, P. S. (2008) Preliminary identification of minerals at the Mars Phoenix Landing Site. *American Geophysical Union Fall Meeting*, Abstract # U14A-03.

Boyton, W.V., Douglas W. Ming, Samuel P. Kounaves, S. M. M. Young, R. E. Arvidson, M. H. Hecht, J. Hoffman, P. B. Niles, D. K. Hamara, R. C. Quinn, P. H. Smith, B. Sutter, D. C. Catling, R. V. Morris (2009) Evidence for calcium carbonate at the Mars Phoenix landing site. *Science* 325**:** doi:10.1126/science.1172768.

Catling, David C., M. Claire, K. Zahnle, Richard Quinn, Benjamin Clark, Michael Hecht, S. Kounaves (2010) Atmospheric origin of perchlorate on Mars and in the Atacama. *Journal of Geophysical Research* 115: doi:10.1029/2009JE003425.

Chevrier, V.F., J. Hanley, T. Altheide (2010) Stability of perchlorate hydrates and their liquid solutions at the Phoenix landing site, Mars. *Geophysical Research Letters* 36: L10202, doi:10.1029/2009GL037497.

Crowley, J.K., (1991) Visible and near-infrared (0.4-2.5 µm) reflectance spectra of playa evaporite minerals. *Journal of Geophysical Research* 96: 16,231-16,240.

Cull, S.C., Raymond E. Arvidson, Michael T. Mellon, Sandra Wiseman, Roger Clark, T. Titus, R. Morris, P. McGuire (2010) Seasonal H_2O and CO_2 ice cycles at the Mars Phoenix landing site: 1. Prelanding CRISM and HiRISE observations. *Journal of Geophysical Research* 115: doi:10.1029/2009JE003340.

Delany J. M. and Lundeen S. R. (1990) The LLNL thermochemical database. Lawrence Livermore National Laboratory, Livermore, CA.

Eswaran, H. and C. Sys. (1979) Argillic horizon in LAC soils: Formation and significance to classification. *Pedologie* 29: 175-190.

Hay, R. L. and R. A. Sheppard (2001) Formation of Zeolites in Open Hydrologic Systems. *Reviews in Mineralogy and Geochemistry* 45.

Hecht, M.H., S. P. Kounaves, R. C. Quinn, S. J. West, S. M. M. Young, D. W. Ming, D. C. Catling, B. C. Clark, W. V. Boynton, J. Hoffman, L. P. DeFlores, K. Gospodinova, J. Kapit, and P. H. Smith (2009) Detection of perchlorate and the soluble chemistry of Martian soil at the Phoenix Lander Site. *Science* **325**: doi: 10.1126/science.1172466.

Helgeson, H.C. (1969) Thermodynamics of hydrothermal systems at elevated temperatures and pressures. *American Journal of Science* 267, 729–804.

Helgeson, H.C. and Kirkham, D.H. (1974a) Theoretical prediction of thermodynamic behavior of aqueous electrolytes at high pressures and temperatures. 1. Summary of thermodynamic-electrostatic properties of solvent. *American Journal of Science* 274, 1089–1198.

Helgeson, H.C. and Kirkham, D.H. (1974b) Theoretical prediction of thermodynamic behavior of aqueous electrolytes at high pressures and temperatures. 2. Debye-Huckel parameters for activity-coefficients and relative partial molal properties. *American Journal of Science* 274, 1199–1261.

Kounaves, S.P., Michael Hecht, S. West, John-Michael Morookian, S. Young, R. Quinn, P. Grunthaner, Z. Wen, M. Wielert, C. Cable,. A. Fisher, K. Gospodinova, J. Kapit, S. Stroble, P. Hsu, B. Clark, D. Ming, P. Smith

(2009) The MECA Wet Chemistry Laboratory on the 2007 Phoenix Mars Scout Lander. *Journal of Geophysical Research* **114**, doi:10.1029/2008JE003084 (2009).

Kounaves , S. P., M. Hecht, J. Kapit, K. Gospodinova, L. DeFlores, R. Quinn, W. Boynton, B. Clark, D. Catling, P. Hredzak, D. Ming, Q. Moore, J. Shusterman, S.Stroble, S. West, S. Young. (2010), Wet Chemistry experiments on the 2007 Phoenix Mars Scout Lander mission: Data analysis and results, *Journal of Geophysical Research*, 115, E00E10, doi:10.1029/2009JE003424.

Kounaves, Samuel P., S. Stroble, Ryan Anderson, Q. Moore, David Catling, Susan Douglas, Christopher McKay, Douglas Ming, Peter Smith, Leslie Tamppari, A. Zent (2010) Discovery of Natural Perchlorate in the Antarctic Dry Valleys and Its Global Implications. *Environmental Science and Technology* **44**(2360-2364).

McSween, H. Y., et al., (2006) Characterization and petrologic interpretation of olivine-rich basalts at Gusev Crater, Mars. *Journal of Geophysical Research* 111, E02S10.

Mellon, M. T., William V. Boynton, William Feldman, R. Arvidson, T. Titus, J. Bandfield, N. Putzig, H. Sizemore (2008) A prelanding assessment of the ice table depth and ground ice characteristics in Martian permafrost at the

Phoenix landing site. *Journal of Geophysical Research* **113**: doi:10.1029/2007JE003067.

Ming, D.W. and Boettinger, J.L. (2001) Zeolites in soil environments. *Reviews in Mineralogy and Geochemistry* 45, 323-345.

Morris, R.V. et al., (2006) Mossbauer mineralogy of rock, soil, and dust at Gusev crater, Mars: Spirit's journey through weakly altered olivine basalt on the plains and pervasively altered basalt in the Columbia Hills. *Journal of Geophysical Research* **111**: doi: 10.1029/2005JE002584.

Murchie, S. L., *et al.*, (2009) Compact Reconnaissance Imaging Spectrometer for Mars investigation and data set from the Mars Reconnaissance Orbiter's primary science phase, *Journal of Geophysical Research*, 114, E00D07, doi:10.1029/2009JE003344.

Passaglia, E. and Sheppard, R.A. (2001) The crystal chemistry of zeolites. *Reviews in Mineralogy and Geochemistry* **45**, 69-116

Roush, T.L., D.L. Blaney, R.B. Singer, (1997) The surface composition of Mars as inferred from spectroscopic observations, in Remote Geochemical Analysis: Elemental and Mineralogical Composition (Pieters and Englert, editors).

Smith, P.H., L. K. Tamppari, R. E. Arvidson, D. Bass, D. Blaney, W. V. Boynton, A. Carswell, D. C. Catling, B. C. Clark, T. Duck, E. DeJong, D. Fisher, W. Goetz, H. P. Gunnlaugsson, M. H. Hecht, V. Hipkin, J. Hoffman, S. F. Hviid, H. U. Keller, S. P. Kounaves, C. F. Lange, M. T.

Lemmon, M. B. Madsen, W. J. Markiewicz, J. Marshall, C. P. McKay, M. T. Mellon, D. W. Ming, R. V. Morris, W. T. Pike, N. Renno, U. Staufer, C. Stoker, P. Taylor, J. A. Whiteway, A. P. Zent (2009) Water at the Phoenix Landing Site. *Science* 325: doi:10.1126/science.1172339.

Tamppari, L.K. et al., (2008) Expected atmospheric environment for the Phoenix landing season and location. *Journal of Geophysical Research* 113, doi:10.1029/2007JE003034.

Chapter 6 - Synthesis: The water cycle at the Phoenix landing site

The water cycle at the Phoenix landing site is part of a complex system, involving interactions with the CO_2 and dust cycles, surface materials, and all three phases of water: solid, liquid, and gas.

This work has shown that most of the surface around the Phoenix landing site is ice-free during the northern early summer, though patches of perennial ice exist on north-facing slopes (Figure 3.9, Figure 3.10), and mobile patches follow crater wall shadows (Figure 3.11) throughout the summer.

During summer, H_2O activity at the Phoenix landing site involves vapor exchange between the atmosphere and subsurface pore ice (e.g., Snow White, Figure 4.2B). Modeling of Snow White-type ice reported in chapter 4 showed that this type of summer vapor-ice exchange is likely responsible for the initial deposition of Snow-White-like pore ice across the northern plains (as originally proposed by *Mellon et al.*, 2004). Modern water vapor is likely in equilibrium with this pore ice.

It is unclear to what extent water vapor is also interacting with the subsurface pure water ice reported in chapter 4, such as that uncovered at the Dodo-Goldilocks site (Figure 4.2A). Although modeling by *Mellon et al.*, [2004] suggests that this pure ice should be unstable at that depth and locale, similar deposits of water ice have been discovered across the northern plains, in recent crater ejecta [*Bryne et al.,* 2009].

Hapke modeling (as presented in chapters 2 and 3) indicates that the water ice reported by *Bryne et al*. [2009] is relatively pure (Figure 6.1). The stability of these pure ice deposits remains unexplained; however, *Mellon et al.* [2009] propose that this type of pure ice may form through thin film migration, and may represent only a thin layer overlying pore ice deposits. Future work is needed to understand the exchanges between the atmosphere and these pure ice deposits, both at the Phoenix landing site and across the northern plains.

In addition to water vapor exchange between the atmosphere and subsurface water ices, water may also adhere to soil grains in thin films, creating the broad 3 µm absorption seen at the Phoenix landing site (Figure 2.4) and across Mars [*Milliken et al.,* 2007]. This soil-atmosphere exchange may account for the exceptional clodiness of the soil observed at the Phoenix landing site (Figure 6.2, *Arvidson et al.* 2009).

Summertime water vapor is one possible mechanism to explain the concentrated perchlorate patches described in Chapter 5 (an alternative mechanism involves seasonal ices, discussed below). During the summer, atmospheric water vapor may be interacting with perchlorate salts that are deposited on the surface through atmospheric interactions between ozone and chlorine [*Catling et al.,* 2010; *Kounaves et al.*, 2010]. Chapter 5 showed that perchlorate salts are concentrated in subsurface patches, not homogeneously distributed across the site (Figure 5.2), as would be expected if they were atmospherically-deposited. The most probable mechanism for translocating perchlorate from the surface to subsurface and concentrating it in patches, is interaction with thin films of liquid water. *Chevier et al.* [2009] showed that Mg-perchlorate brines are stable above 206K, well below the 245K maximum temperature recorded by Phoenix. It is therefore possible that summertime water vapor interacts with perchlorate on the surface, forming thin film brines which then diffuse through the soil column.

This work has shown that seasonal water ice first begins to form on the surface at the Phoenix site between L_s~104° to 109°. Water ice continues to form on the surface during the night, lingers through the early morning, and sublimates during the late morning to afternoon, until L_s~154°, after which water ice is stable on sunlit surfaces throughout the day.

The timing of ice deposition at the Phoenix site varied significantly in the two years tracked here. CRISM observations first show afternoon water ice on the surface at L_s~167° during the 2006/2007 observing cycle and at L_s~154° during the 2008/2009 cycle: a difference of 36 sols. The differences may be due to the atmospheric dust cycle, which exerts a strong control on atmospheric temperature [*Kahn et al.*, 1992, *Smith et al.*, 2002]. Temperature in turn controls the amount of water the atmosphere can hold at a given time.

During fall, water ice continues to form on the surface, possibly due to precipitation from cloud layers, as observed by *Whiteway et al.* [2009], or due to radiative cooling, as predicted from modeling by *Forget et al.* [1998]. CO_2 ice begins to form on the surface sometime after L_2~181°.

By mid-winter (L_s~344˚), the landing site is covered by a layer of CO_2 ice ~30 cm thick, a thickness supported by CRISM modeling and HiRISE ice-depth measurements (Table 2.3) reported in chapter 2. The thickness of the mid-winter layer is further supported by recent observations of the Phoenix lander emerging from the spring defrosting period: the observations show the lander's wide solar panels have been broken off, as would be expected if a heavy layer of ice was deposited on top of it (Figure 6.3).

The winter CO_2 ice layer is most likely in the form of a semi-transparent slab, formed as individual CO_2 ice grains sinter together over the course of the fall and winter. This process has been reported elsewhere on Mars as well (*e.g., Titus et al.,* 2001). The CO_2 ice slab is covered by a thin layer of water ice, presumably cold-trapped onto the surface by the CO_2 ice. The water ice deposited in the late summer and fall is still trapped beneath the CO_2 ice slab; however, it is not visible to near-infrared CRISM observations.

Winter ice may also provide an alternative mechanism for perchlorate brine formation. During fall, winter, and early spring, the surface is covered by the thin layer of fall-deposited water ice, underlying a thick layer of CO_2 ice. During this time, it is possible that the fall-deposited water ice comes in contact surface perchlorate salts. The overlying CO_2 ice slab may act as a greenhouse cap [*Kieffer et al.,* 2000], inducing minor melting of seasonal water ice. This process could form the thin-films that are responsible for redistributing perchlorate reported in chapter 5.

These films would be easily transported from the surface to the subsurface by gravity-driven diffusion, where they would form concentrated patches of perchlorate salt, such as those observed at the Phoenix landing site (Figure 5.2).

Thin films of liquid water appear to be the only mechanism capable of concentrating perchlorate into the patches observed at the Phoenix landing site; seasonal melt water or summertime water vapor are the most likely sources for these films. Further work is needed to understand the conditions under which perchlorate salts interact with water ice and water vapor, and the geographic extent of these interactions.

As northern spring progresses, the CO_2 slab breaks up into smaller grains, presumably due to an increase in solar insulation, [*e.g.*, *Titus et al.*, 2001]. As the CO_2 sublimates away, water ice dominates the site's near-infrared spectra (Figure 2.7).

The spectral dominance of water ice during the spring defrosting period has been reported before [*e.g.*, *Bibring et al.*, 2005]. It has been proposed that the water ice annulus could be due to cold-trapped water on the surface of the retreating CO_2, or due to water ice deposited in fall and re-exposed in spring as the CO_2 cap retreats. Chapter 2 shows that the initial spectral dominance of water ice occurs before the CO_2 has fully retreated and that the water ice is most likely cold-trapped onto the CO_2. Later, as the final CO_2 ice sublimates (L_s~34˚), fall-deposited water ice dominates for approximately two months, until (L_s~59˚).

Spring ice sublimation is not uniform. Ice disappears first from polygon centers, later from polygon troughs (Figure 2.11). *Searls et al.* [2010] proposed that this may be due to differences in thermal conductivity, possibly related to airborne dust that is trapped in polygon troughs, thus lowering the thermal inertia of the surface over those areas. However, this is inconsistent with findings from *Heet et al.* [2009], which show that cryoturbation tends to concentrate rocks in polygon troughs (Figure 6.4). Alternatively, shadowing or differences in ice table depth may be responsible for the different rates of sublimation from troughs and centers.

Ice sublimation also varies with geomorphic unit (Figure 2.12). Ice disappear first from Lowland Dark and Knobby identified by *Seelos et al*. [2008], then from Block/Mesa terrain, then Highland Unit, then Lowland Bright Unit, and finally debris aprons surrounding plateaus. On a regional scale, it is possible that subsurface ice type, depth, and distribution might be influencing ice sublimation. These results call for a detailed analysis of the relationship between subsurface ice and seasonal ice deposition/sublimation patterns.

Overall, the modern water cycle at the Phoenix landing site involves water vapor, subsurface ice, seasonal ice, and thin films of liquid water. It is strongly influenced by the CO_2 and dust cycles, surface mineralogy (especially soluble salts), and surface physical properties (especially thermal inertia). And, it has a high degree of interannual variability.

Figures

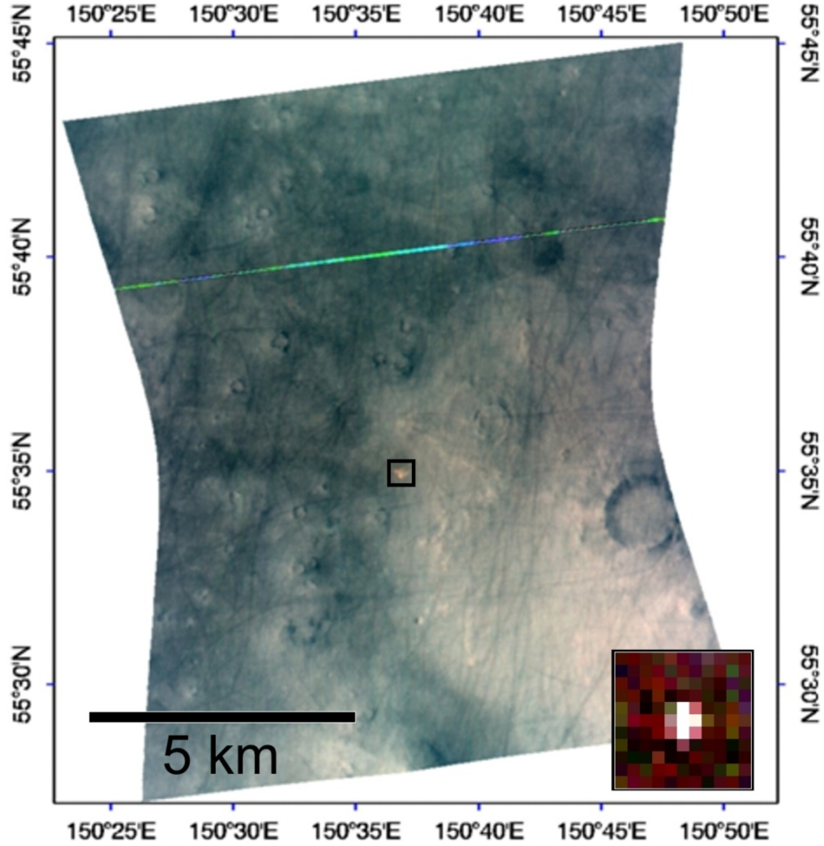
150°25'E
150°30'E
150°35'E
150°40'E
150°45'E
150°50'E
55°45'N
55°40'N
55°35'N
55°30'N
5 km

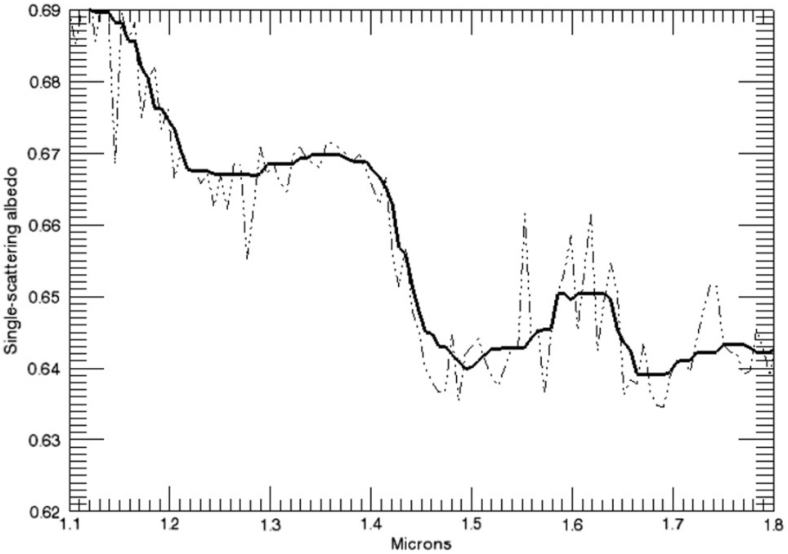
0.69
0.68
0.67
0.66
0.65
0.64
0.63
0.62
Single-scattering albedo
1.1
1.2
1.3
1.4
1.5
1.6
1.7
1.8
Microns

Figure 6.1 - Water ice in crater ejecta.

A CRISM observation (FRT0000D2F7) of a freshly-formed crater on the northern plains of Mars. The crater (boxed and enlarged in the corner) was observed in HiRISE images [*Byrne et al.,* 2009], then imaged with CRISM. The CRISM spectrum of the crater material (bottom) was processed according to the atmospheric-correction process laid out in chapter 2. The spectrum has broad water ice features at 1.5 an 2.0 μm, indicating that the bright white material is water ice. This – and craters like it, reported in *Bryne et al. [*2009] – is evidence of subsurface water ice at mid-latitudes, south of the Phoenix landing site. The strong water ice signature suggests pure water ice, as opposed to pore ice.

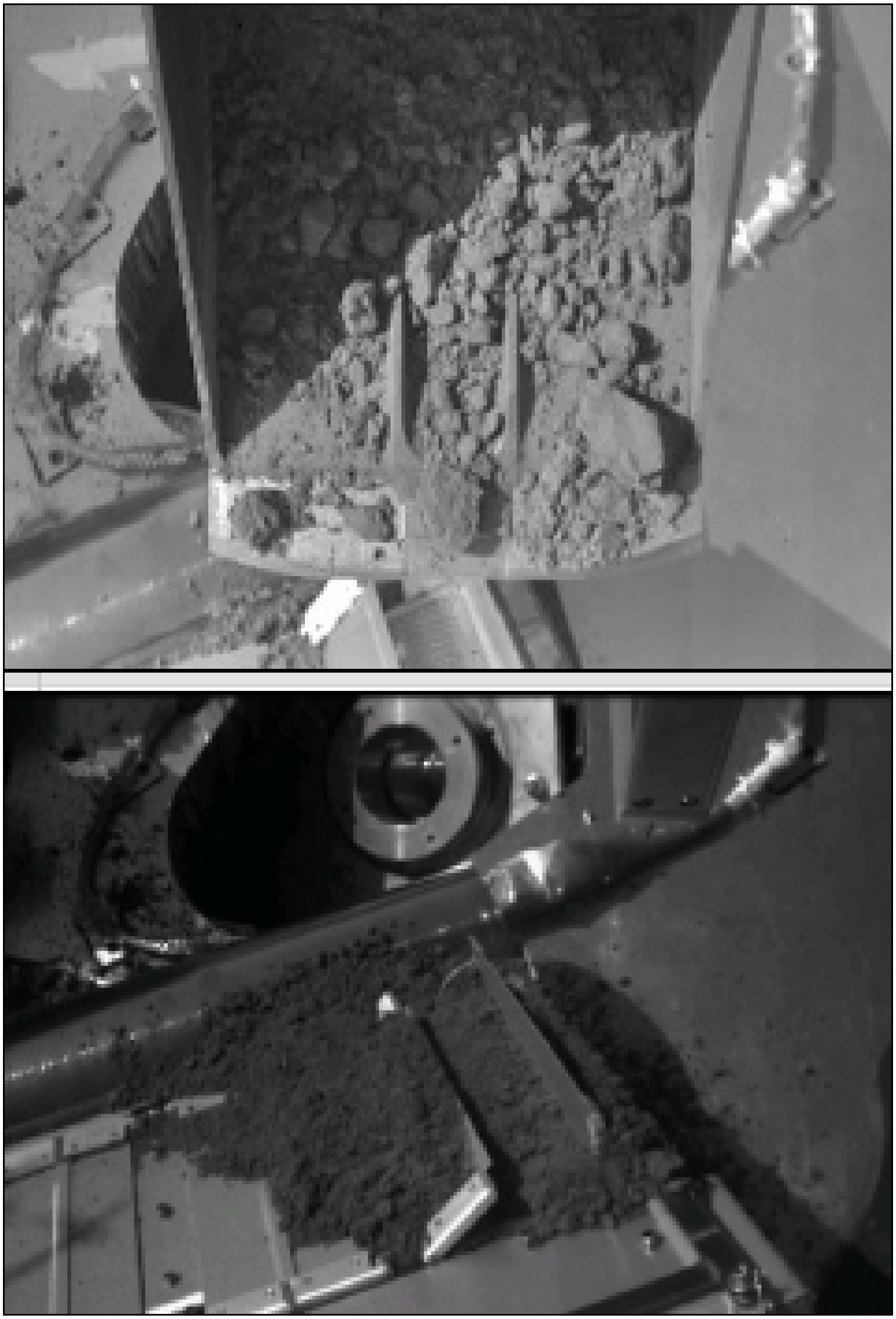

Figure 6.2- Cloddy soils at the Phoenix landing site.

Soil samples showed that Phoenix soils are highly clumpy. Top: An image from the Robotic Arm Camera (RAC, image token 11C3) showing dirt in the Robotic Arm's scoop. The material is newly-excavated soils and is highly cloddy. Bottom: RAC image (token 11C9). When delivered to Phoenix's TEGA instrument, the Phoenix soils were too cloddy to sift through the mesh screen. They clumped on top of the screen and required shaking to fall into the doors.

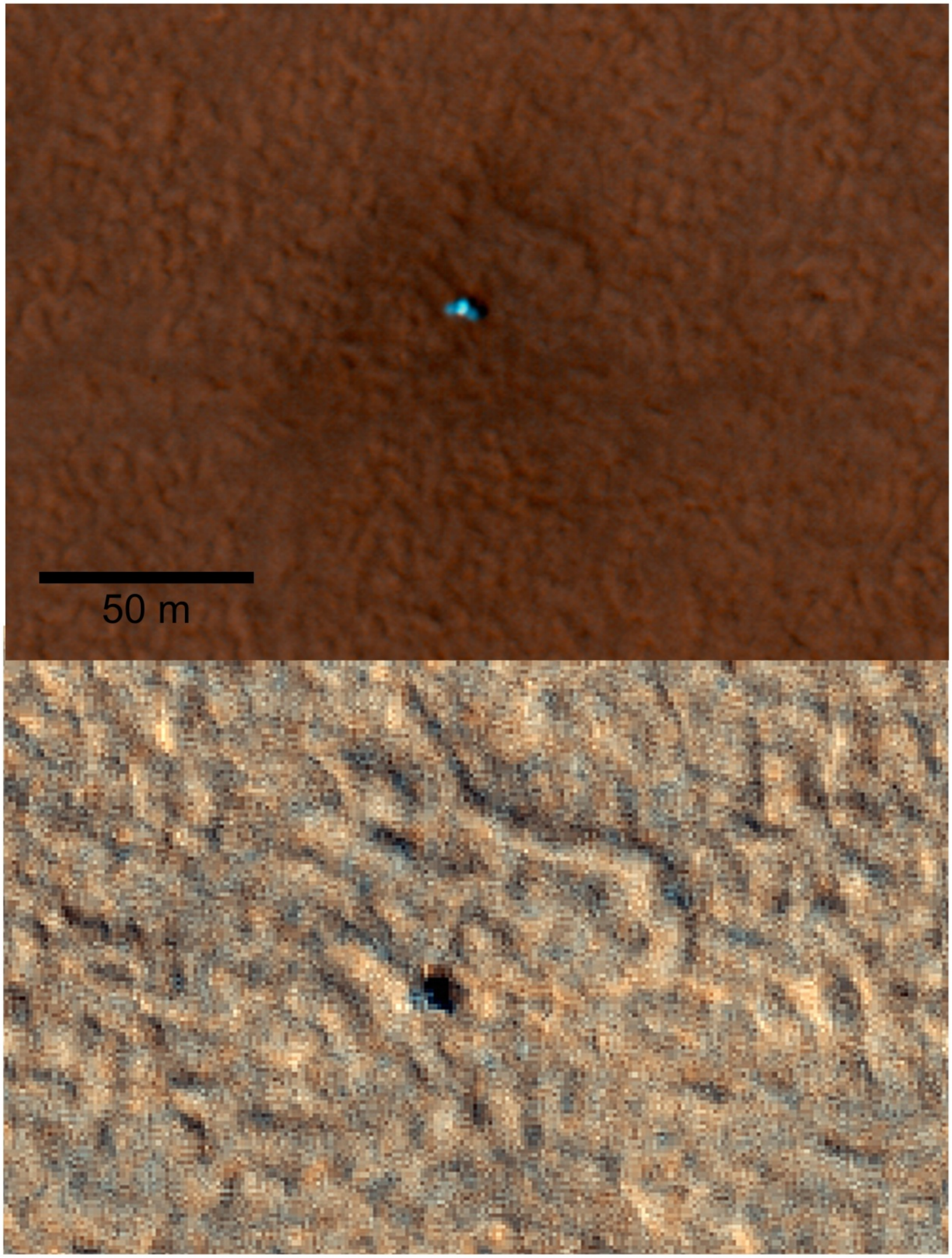

Figure 6.3 – HiRISE observations of the Phoenix lander in 2008 and 2010.

The 2008 observation (top, PSP_008591_2485) was taken during the northern summer, just after Phoenix landed on the surface. The central bright spot is the lander deck. The two bright circles on either side are the lander's two solar panels. The 2010 observation (bottom, ESP_017716_2485) was taken the following northern spring, just after the Phoenix lander's first winter on Mars. In the 2010 observation, the Phoenix's large solar panels appear to have broken off, as would be expected if the spacecraft was buried under a thick layer of ice all winter.

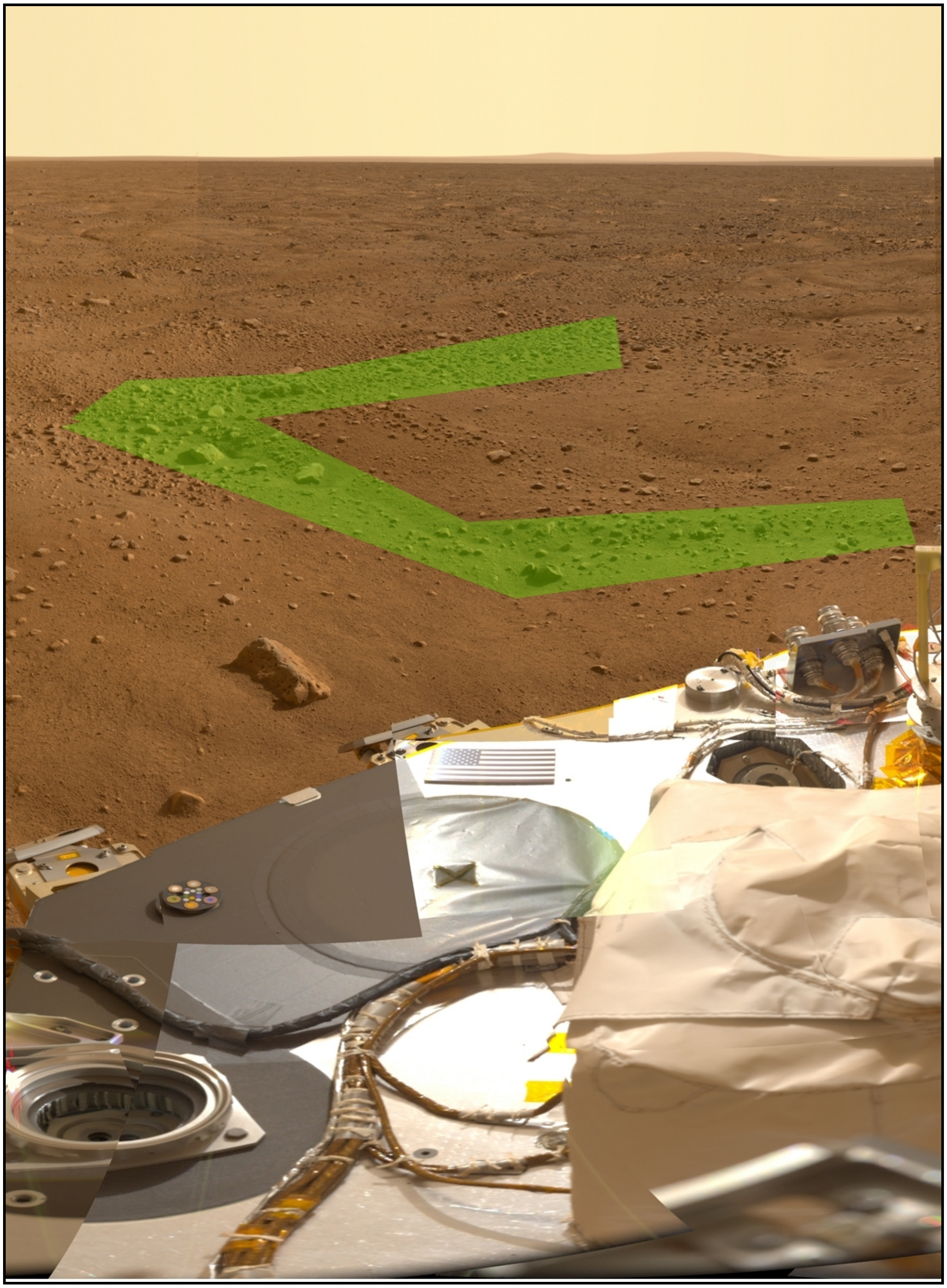

Figure 6.4 - Phoenix site polygons.

A portion of an SSI mosaic (Mission Success Pan, R=603.8 nm, G=532.0 nm, B=: 485.3 nm) from the Phoenix landing site, showing several polygons stretching out into the distance. A few polygon troughs have been marked in a green overlay. The troughs have higher densities of rocks than the polygon centers, presumably due to reworking from cryoturbation cycles.

References

Arvidson, R.E., R. Bonitz, M. Robinson, J. Carsten, R. Volpe, A. Trebi-Ollennu, M. Mellon, P. Chu, K. Davis, J. Wilson, A. Shaw, R. Greenberger, K. Siebach, T. Stein, S. Cull, W. Goetz, R. Morris, D. Ming, H. Keller, M. Lemmon, H. Sizemore, M. Mehta (2009), Results from the Mars Phoenix Lander Robotic Arm experiment, *Journal of Geophysical Research*, 114, E00E02, doi:10.1029/2009JE003408.

Bibring, Jean-Pierre, Yves Langevin, Aline Gendrin, Brigitte Gondet, François Poulet, Michel Berthé, Alain Soufflot, Ray Arvidson, Nicolas Mangold, John F. Mustard, Pierre Drossart, the OMEGA team (2005) Mars surface diversity as revealed by OMEGA/Mars Express observations. *Science* 307: 1576. DOI: 10.1126/science.1108806

Byrne, S., Colin M. Dundas, Megan R. Kennedy, Michael T. Mellon, Alfred S. McEwen, Selby C. Cull, Ingrid J. Daubar, David E. Shean, Kimberly D. Seelos, Scott L. Murchie, Bruce A. Cantor, Raymond E. Arvidson, Kenneth S. Edgett, Andreas Reufer, Nicolas Thomas, Tanya N. Harrison, Liliya V. Posiolova, Frank P. Seelos (2009) Distribution of mid-latitude ground-ice on Mars from new impact craters. *Science*, 325(5948): 1674-1676. doi: 10.1126/science.1175307

Catling, D.C. M. Claire, K. Zahnle, R. Quinn, B. Clark, M. Hecht, S. Kounaves (2010) Atmospheric origin of perchlorate on Mars and in the Atacama. *Journal of Geophysical Research* **115**: doi:10.1029/2009JE003425.

Chevrier, V.F., J. Hanley, T. Altheide (2010) Stability of perchlorate hydrates and their liquid solutions at the Phoenix landing site, Mars. *Geophysical Research Letters* 36: L10202, doi:10.1029/2009GL037497.

Forget, F., F. Hourdin, O. Talagrand (1998) CO_2 snowfall on Mars: Simulation with a general circulation model. *Icarus* 131(2), 302-316, doi:10.1006/icar.1997.5874.

Gilfichinsky, D.A. et al., (2007) Microbial populations in Antarctic permafrost: Biodiversity, state, age, and implications for astrobiology. Astrobiology 7: 275-311.

Heet, T,. R. E. Arvidson, S. C. Cull, M. T. Mellon, and K. D. Seelos (2009) Geomorphic and geologic settings of the Phoenix lander mission landing site. *Journal of Geophysical Research*, 114, E00E04, doi:10.1029/2009JE003416, 2009.

Kahn, R.A., Martin, T.Z., Zurek, R.W., Lee, S.W., (1992) The martian dust cycle. In: Kieffer, H.H., Jakosky, B.M., Snyder, C.W., Matthews, M. (Eds.), Mars. University of Arizona Press, Tucson, pp. 1017–1053

Kereszturi, A., D. Mohlmann, Sz. Berczi, T. Ganti., A. Kuti, A. Sik, A. Horvath (2009) Recent rheologic processes on dark polar dunes of Mars: Driven by interfacial water? *Icarus* 201: 492-503. doi:10.1016/j.icarus.2009.01.014

Kieffer, H. H., T. N. Titus, K. F. Mullins, and P. R. Christensen (2000), Mars south polar spring and summer behavior observed by TES: Seasonal cap evolution controlled by frost grain size, *Journal of Geophysical Research*, 105(E4), 9653–9699. doi:10.1029/1999JE001136

Kossacki, K.J. and Markiewicz, W.J. (2010) Interfacial liquid water on Mars and its potential role in formation of hill and dune gullies. *Icarus*, 210: . doi:10.1016/j.icarus.2010.06.029

Kounaves, S. P., S. Stroble, R. Anderson, Q. Moore, D. Catling, S. Douglas, C. McKay, D. Ming, P. Smith, L. Tamppari, A. Zent (2010) Discovery of Natural Perchlorate in the Antarctic Dry Valleys and Its Global Implications. *Environmental Science and Technology* 44 (2360-2364). DOI: 10.1021/es9033606.

Mellon, M., W. Feldman, T. Prettyman (2004) The presence and stability of ground ice in the southern hemisphere of Mars. *Icarus* 169: 324-340. doi:10.1016/j.icarus.2003.10.022

Mellon, M.T., R. Arvidson, H. Sizemore, M. Searls, D. Blaney, S. Cull, M. Hecht, T. Heet, H.U. Keller, M. Lemmon, W. Markiewicz, D. Ming, R. Morris, W. Pike, A. Zent (2009) Ground ice at the Phoenix landing site: Stability, state, and origin. *Journal of Geophysical Research* 114: E00E08, doi:10.1029/2009JE003417.

Milliken, R. E., J. F. Mustard, F. Poulet, D. Jouglet, J.-P. Bibring, B. Gondet, and Y. Langevin (2007), Hydration state of the Martian surface as seen by Mars Express OMEGA: 2. H_2O content of the surface, *Journal of Geophysical Research*, 112, E08S07, doi:10.1029/2006JE002853.

Moehlmann, D.T.F. (2008) The influence of van der Waals forces on the state of water in the shallow subsurface of Mars. *Icarus* 195: doi:10.1016/j.icarus.2007.11.026

Searls, M.L., M. Mellon, S. Cull, C.J. Hansen, H. Sizemore (2010) Seasonal defrosting of the Phoenix landing site. *Journal of Geophysical Research* 115: E00E24, doi:10.1029/2009JE003438.

Seelos, K. D., R. Arvidson, S. Cull, C. Hash, T. Heet, E. Guinness, P. McGuire, R. Morris, S. Murchie, T. Parker, T. Roush, F. Seelos, M. Wolff (2008), Geomorphologic and mineralogic characterization of the northern plains of Mars at the Phoenix Mission candidate landing sites, *Journal of Geophysical Research*, 113, E00A13, doi:10.1029/2008JE003088.

Smith, M.D., Conrath, B.J., Pearl, J.C., Christensen, P.R., (2002) Thermal Emission Spectrometer Observations of martian planet-encircling dust storm 2001A. *Icarus* 157, 259–263. doi:10.1006/icar.2001.6797

Smith, P.H., L. K. Tamppari, R. E. Arvidson, D. Bass, D. Blaney, W. V. Boynton, A. Carswell, D. C. Catling, B. C. Clark, T. Duck, E. DeJong, D. Fisher, W. Goetz, H. P. Gunnlaugsson, M. H. Hecht, V. Hipkin, J. Hoffman, S. F. Hviid, H. U. Keller, S. P. Kounaves, C. F. Lange, M. T. Lemmon, M. B. Madsen, W. J. Markiewicz, J. Marshall, C. P. McKay, M. T. Mellon, D. W. Ming, R. V. Morris, W. T. Pike, N. Renno, U. Staufer, C. Stoker, P. Taylor, J. A. Whiteway, A. P. Zent (2009) Water at the Phoenix Landing Site. *Science* 325: doi:10.1126/science.1172339.

Titus, T. N., H. H. Kieffer, K. F. Mullins, and P. R. Christensen (2001), TES premapping data: Slab ice and snow flurries in the Martian north polar night, *Journal of Geophysical Research*, 106(E10), 23,181–23,196. doi:10.1029/2000JE001284

Whiteway, J. M., L. Komguem, Cameron Dickinson, C. Cook, M. Illnicki, J. Seabrook, V. Popovici, T. Duck, R. Davy, P. Taylor, J. Pathak, David Fisher, A. Carswell, M. Daly, V. Hipkin, A.Zen, M. Hecht, S. Wood, L. Tamparri, N. Renno, J. Moores, M. Lemmon, F. Daerden, P. Smith (2009) Mars Water Ice Clouds and Precipitation, *Science*, 325(68). DOI:10.1126/science.1172344.